Influence of indentations on rolling bearing life

Nans Biboulet

To cite this version:

Nans Biboulet. Influence of indentations on rolling bearing life. Mechanics [physics.med-ph]. INSA de Lyon, 2008. English. NNT : 2008ISAL0054 . tel-00663264

HAL Id: tel-00663264
https://theses.hal.science/tel-00663264v1

Submitted on 26 Jan 2012

n° d'ordre : 2008-ISAL-0054 Année 2008

THESE

présentée

DEVANT L'INSTITUT NATIONAL DES SCIENCES APPLIQUEES DE LYON

pour obtenir

LE GRADE DE DOCTEUR

ECOLE DOCTORALE DES SCIENCES POUR L'INGENIEUR DE LYON :
MECANIQUE, ENERGETIQUE, GENIE CIVIL, ACOUSTIQUE (M.E.G.A.)
SPECIALITE : MECANIQUE

par

Nans BIBOULET
Ingénieur I.N.S.A. de Lyon

INFLUENCE OF INDENTATIONS ON ROLLING BEARING LIFE

Soutenue le 16 septembre 2008 devant la commission d'examen :

Jury :	**M.**	**K.**	**Dang Van**	
	M.	**J.**	**Frêne**	**Rapporteur**
	M.	**C.J.**	**Hooke**	**Rapporteur**
	M.	**L.**	**Houpert**	
	M.	**A.A.**	**Lubrecht**	
	M.	**J.**	**Seabra**	
	M.	**F.**	**Ville**	

Cette thèse a été préparée au Laboratoire de Mécanique des Contacts et des Structures de l'I.N.S.A. de Lyon

INSA Direction de la Recherche - Ecoles Doctorales – Quadriennal 2007-2010

SIGLE	ECOLE DOCTORALE	NOM ET COORDONNEES DU RESPONSABLE
CHIMIE	**CHIMIE DE LYON** **http://sakura.cpe.fr/ED206** M. Jean Marc LANCELIN Insa : R. GOURDON	M. Jean Marc LANCELIN Université Claude Bernard Lyon 1 Bât CPE 43 bd du 11 novembre 1918 69622 VILLEURBANNE Cedex Tél : 04.72.43 13 95 Fax : lancelin@hikari.cpe.fr
E.E.A.	**ELECTRONIQUE, ELECTROTECHNIQUE, AUTOMATIQUE** **http://www.insa-lyon.fr/eea** M. Alain NICOLAS Insa : D. BARBIER ede2a@insa-lyon.fr Secrétariat : M. LABOUNE AM. 64.43 – Fax : 64.54	M. Alain NICOLAS Ecole Centrale de Lyon Bâtiment H9 36 avenue Guy de Collongue 69134 ECULLY Tél : 04.72.18 60 97 Fax : 04 78 43 37 17 eea@ec-lyon.fr Secrétariat : M.C. HAVGOUDOUKIAN
E2M2	**EVOLUTION, ECOSYSTEME, MICROBIOLOGIE, MODELISATION** **http://biomserv.univ-lyon1.fr/E2M2** M. Jean-Pierre FLANDROIS Insa : H. CHARLES	M. Jean-Pierre FLANDROIS CNRS UMR 5558 Université Claude Bernard Lyon 1 Bât G. Mendel 43 bd du 11 novembre 1918 69622 VILLEURBANNE Cédex Tél : 04.26 23 59 50 Fax 04 26 23 59 49 06 07 53 89 13 e2m2@biomserv.univ-lyon1.fr
EDIIS	**INFORMATIQUE ET INFORMATION POUR LA SOCIETE** http://ediis.univ-lyon1.fr M. Alain MILLE Secrétariat : I. BUISSON	M. Alain MILLE Université Claude Bernard Lyon 1 LIRIS - EDIIS Bâtiment Nautibus 43 bd du 11 novembre 1918 69622 VILLEURBANNE Cedex Tél : 04.72. 44 82 94 Fax 04 72 44 80 53 ediis@liris.cnrs.fr - alain.mille@liris.cnrs.fr
EDISS	**INTERDISCIPLINAIRE SCIENCES-SANTE** Sec : Safia Boudjema M. Didier REVEL Insa : M. LAGARDE	M. Didier REVEL Hôpital Cardiologique de Lyon Bâtiment Central 28 Avenue Doyen Lépine 69500 BRON Tél : 04.72.68 49 09 Fax :04 72 35 49 16 Didier.revel@creatis.uni-lyon1.fr
Matériaux	**MATERIAUX DE LYON** M. Jean Marc PELLETIER Secrétariat : C. BERNAVON 83.85	M. Jean Marc PELLETIER INSA de Lyon MATEIS Bâtiment Blaise Pascal 7 avenue Jean Capelle 69621 VILLEURBANNE Cédex Tél : 04.72.43 83 18 Fax 04 72 43 85 28 Jean-marc.Pelletier@insa-lyon.fr
Math IF	**MATHEMATIQUES ET INFORMATIQUE FONDAMENTALE** M. Pascal KOIRAN Insa : G. BAYADA	M.Pascal KOIRAN Ecole Normale Supérieure de Lyon 46 allée d'Italie 69364 LYON Cédex 07 Tél : 04.72.72 84 81 Fax : 04 72 72 89 69 Pascal.koiran@ens-lyon.fr Secrétariat : Fatine Latif - latif@math.univ-lyon1.fr
MEGA	**MECANIQUE, ENERGETIQUE, GENIE CIVIL, ACOUSTIQUE** M. Jean Louis GUYADER Secrétariat : M. LABOUNE PM : 71.70 –Fax : 87.12	M. Jean Louis GUYADER INSA de Lyon Laboratoire de Vibrations et Acoustique Bâtiment Antoine de Saint Exupéry 25 bis avenue Jean Capelle 69621 VILLEURBANNE Cedex Tél :04.72.18.71.70 Fax : 04 72 18 87 12 mega@lva.insa-lyon.fr
ScSo	**ScSo*** M. BRAVARD Jean Paul Insa : J.Y. TOUSSAINT	M. BRAVARD Jean Paul Université Lyon 2 86 rue Pasteur 69365 LYON Cedex 07 Tél : 04.78.69.72.76 Fax : 04.37.28.04.48 Jean-paul.bravard@univ-lyon2.fr

*ScSo : Histoire, Geographie, Aménagement, Urbanisme, Archéologie, Science politique, Sociologie, Anthropologie

Résumé

Les lubrifiants contiennent des particules qui sont à la fois initialement présentes dans le lubrifiant et dans le mécanisme (fabrication, stockage...); générées durant le rodage, par usure ou corrosion; ou bien issues de sources externes.

Les particules détériorent les surfaces en créant des indents lorsqu'elles sont piégées dans les contacts. Ces indents augmentent le risque de rupture par fatigue en induisant des perturbations de pression et de contraintes.

Ce travail est basé sur une étude des contacts indentés secs et lubrifiés (EHD). L'équation de Reynolds en fluide Newtonien est utilisée. Les techniques mutigrilles et multi-intégration sont employées.

L'objectif de ce travail est de proposer un modèle de prédiction des perturbations des champs de pression et de contraintes, et finalement un modèle de réduction de durée de vie des contacts indentés en fonction de la géométrie des indents et des conditions de contact.

Mot-clés : contact ponctuel, contact elliptique, contact sec, lubrification, EHD, élastohydrodynamique, Reynolds, multigrilles, multi-intégration, réduction d'amplitude, pollution, contamination, débris, particule, indent, indentation, prédiction de durée de vie, roulement, fatigue

Abstract

All lubricants contain particles. These particles are both initially present in the lubricant and mechanisms (manufacturing process, storage...); generated during running-in, through wear and corrosion; or come from external sources.

These particles damage the surfaces, creating indents when they are squashed in the contact. These indents increase the fatigue failure risk inducing pressure and stress perturbations.

This work is based on a dry and lubricated (EHL) contact study. The Reynolds equation for Newtonian fluids is used. Multigrid and multi-integration techniques are used to limit computing time.

The aim is to predict pressure and stress distribution perturbations, and finally to predict the life reduction of indented contacts as a function of the indent geometry and the operating conditions.

Keywords: point contact, elliptical contact, dry contact, lubrication, EHL, elastohydrodynamic, Reynolds, multigrid, multi-integration, amplitude reduction theory, pollution, contamination, debris, particle, indent, indentation, life prediction, rolling element bearing, fatigue

Foreword

Contents

Notation

α	pressure viscosity index [Pa^{-1}]
$\bar{\alpha}$	dimensionless viscosity index [.] $= \alpha p_H$
δ	correction [.]
ΔP	dimensionless additional pressure amplitude [.]
$\mathcal{S}\Delta P$	initial slope of the dimensionless additional pressure [.] $= \left. \dfrac{\mathrm{d}\Delta P(D/\Phi)}{\mathrm{d}(D/\Phi)} \right\rvert_{D/\Phi \to 0}$
η	viscosity [Pa.s]
$\overline{\eta}$	dimensionless viscosity [.] $= \eta/\eta_0$
η_0	viscosity at ambient pressure [Pa.s]
κ	ellipticity [.] $= b/a$
λ	roughness wavelength [m]
$\overline{\lambda}$	parameter of Reynolds equation [.] $= 12 u_m \eta_0 R_x^2/(b^3 p_H)$
∇	dimensionless wavelength parameter [.] $= \lambda/b \cdot \sqrt{M/L}$
∇_Φ	dimensionless indent parameter [.] $\propto \Phi \cdot \sqrt{M/L}$
ν	function of the decay coefficient K [.]
ν_1, ν_2	Poisson coefficient for body 1 and 2 [.]
ω	adjustment coefficient [.]
ω	under relaxation coefficient [.]
Ω	integration domain [.]
ϕ	indent diameter [m]
Φ	dimensionless indent diameter [.] $= \phi/b$
ρ	radius of curvature [m]
ρ	density [kg/m^3]
ρ_0	density at ambient pressure [kg/m^3]
$\overline{\rho}$	dimensionless density [.] $= \rho/\rho_0$
σ'	stress [Pa]
σ	dimensionless stress [.] $= \sigma'/p_H$
τ	stress criterion for the stress risk integral [Pa]
ϑ	failure probability [.]
ξ	dimensionless coefficient in Reynolds equation [.]
ζ	function of the decay coefficient K [.]

a	Hertzian contact half width along y (major axis ellipse) [m]
A	line relaxation matrix
b	Hertzian contact half width along x (minor axis ellipse) [m]
c	stress exponent [.]
d	indent depth [m]
D	dimensionless indent depth [.] $= dR_x/b^2$
e	Weibull slope [.]
E_1, E_2	Young modulus for body 1 and 2 [Pa]
E'	equivalent Young modulus [Pa]
$\mathcal{E}$	elliptical integral of the second kind [.]
f	right member [.]
F	ratio between initial and deformed indent depth [.] $= D_d/D_i$
$\mathcal{F}$	failure probability [.]
h	depth exponent [.]
h	gap height [m]
h_X, h_Y	dimensionless mesh size [.]
h_T	dimensionless time step [.]
H	dimensionless gap height [.] $= hR_x/b^2$
H_0	dimensionless mutual approach [.]
i, j	index in space [.]
I	risk integral
$\bar{I}$	dimensionless risk integral [.] $= (I/(b^3\, p_H^c))^{1/c}$
I_h^H, I_H^h	restriction and interpolation operators
$\mathbb{I}_H^h, \mathbb{I}_h^H$	restriction and interpolation operators (MLMI)
k	index in time [.]
K	decay coefficient [.]
K	elastic kernel [.]
$\mathcal{L}$	differential operator
L	Moes parameter [.] $= \alpha\, E' \cdot ((2\,\eta_0\, u_m)/(E'\, R_x))^{1/4}$
m	adjustment coefficient [.]
M	Moes parameter [.] $= w/(E'\, R_x^2) \cdot ((2\,\eta_0\, u_m)/(E'\, R_x))^{-3/4}$
n	adjustment coefficient [.]
n_X, n_Y	number of points along X and Y [.]
p	pressure [Pa]
P	dimensionless pressure [.] $= p/p_H$
p_H	maximum Hertzian pressure [Pa]
P_{REF}	dimensionless reference pressure [.]
q_K	function of the decay coefficient K [.]
q_{T_∞}	function of the dimensionless infinite life [.]
r	residual term [.]
r	radius [m] $= \sqrt{x^2 + y^2}$
r_h	shoulder top radius [m]
rh_X, rh_Y	dimensionless inverse mesh size [.] $= 1/h_X, = 1/h_Y$
rh_T	dimensionless inverse time step [.] $= 1/h_T$
R	dimensionless radius [.]
R_{x1}, R_{x2}	radii of curvature along X for body 1 and 2 [m]
R_{y1}, R_{y2}	radii of curvature along Y for body 1 and 2 [m]

R_x, R_y	reduced radii of curvature [m]
$\mathcal{R}$	roughness or indent [m]
$\bar{\mathcal{R}}$	dimensionless roughness or indent [.]
s	adjustment coefficient [.]
s_h	shoulder height [m]
t	time [s]
T	dimensionless time $[.] = tu_m/b$
T	dimensionless stress criterion for the stress risk integral $[.] = \tau/p_H$
u	speed [m/s]
u	unknown
v	numerical error [.]
w	load [N]
x, y, z	coordinates [m]
X, Y, Z	dimensionless coordinates $[.] = x/b, = y/b, = z/b$
X_a, X_b	dimensionless domain boundaries along X [.]
Y_a, Y_b	dimensionless domain boundaries along Y [.]

$\bigcirc^{DRY}$	dry contact
$\bigcirc^{EHL}$	EHL contact
$\bigcirc^{VM}$	Von Mises
$\bigcirc^{PA}$	Papadopoulos
$\tilde{\bigcirc}$	not converged
$\bar{\bigcirc}$	corrected
$\hat{\bigcirc}$	coarse grid variable
$\underline{\bigcirc}$	discrete
$\overline{\bigcirc}^h$	fine grid
$\bigcirc^H$	coarse grid
$\bigcirc_b$	hole
$\bigcirc_d$	deformed
$\bigcirc_h$	hydrostatic
$\bigcirc_h$	shoulder
$\bigcirc_H$	Hertzian
$\bigcirc_i$	initial
$\bigcirc_{GS}$	Gauss-Seidel
$\bigcirc_{JA}$	Jacobi
$\bigcirc_{PT}$	pseudo-transient
$\bigcirc_\infty$	infinite life limit
$\bigcirc_m$	mean
$\bigcirc_{FRONT}$	front indent shoulder (first in the contact)
$\bigcirc_{LAT}$	lateral indent shoulder
$\bigcirc_{REAR}$	rear indent shoulder
$\bigcirc_{CENT}$	indent center
$\bigcirc_D$	dented
$\bigcirc_S$	smooth

Chapter 1

General introduction

Tribology is literally the study of friction between two contacting surfaces. By extension, tribology treats the associated problems of lubrication and surface deterioration (wear, fatigue...). It includes phenomena that occur in everyday life and is implicated in a wide range of mechanisms. Actually, every contact is subjected to friction (desirable or not) and surface deterioration. The understanding of the underlying mechanisms requires a combination of knowledge from various fields (physics, chemistry, material science, mechanical engineering, mathematics...). This work is restricted to the domain of elastohydrodynamic lubrication (EHL).

EHL contacts are encountered when a lubricant (frequently oil or grease) separates the two contacting bodies and the contact pressure is so high that both surfaces are elastically deformed. The lubricant limits friction and wear. The lubricant film formed between the two surfaces is very thin, typically thinner than 1 μm. The high contact pressure leads to a radical change in the lubricant behavior which becomes almost solid (piezoviscous effect). These two aspects characterize EHL contacts: important surface deformation and important piezoviscous effects.

This kind of contact is found in various applications: cam tappet, gears, rolling element bearings...This work is mainly dedicated to the study of contacts in rolling element bearings.

The function of a rolling element bearing is to enable a relative rotation between two elements with precision and minimum frictional power losses. Rolling element bearings are constituted by two concentric rings, a set of rollers and a cage, see figure 1.1. The two rings rotate at different speeds. The rollers adapt this velocity difference and transmit the load minimizing the friction. Decreasing friction has been a crucial aspect[1]. The load is transmitted between the rings and the rollers by pressures created on the contact areas. The cage separates the rollers.

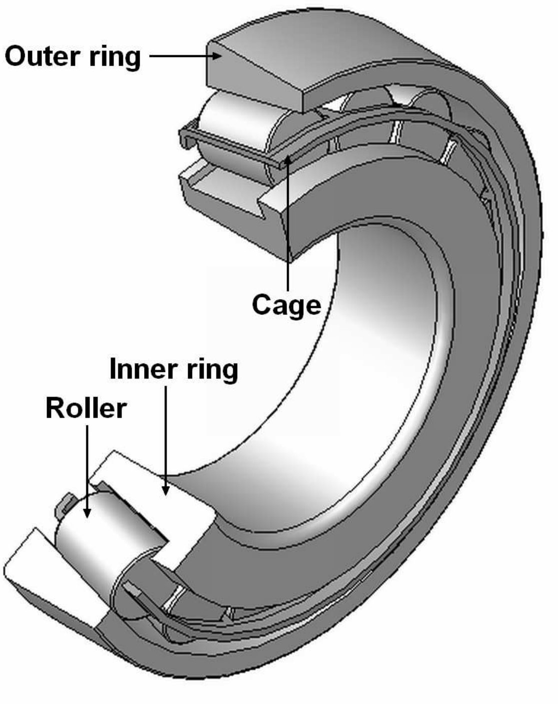

Figure 1.1: Tapered roller bearing

The system of equations describing the EHL problem is complicated. Some advanced numerical techniques have to be used. The chapter 2 gives an overview of the equations and of the numerical techniques used. Figure 1.3 represents a typical EHL pressure and film thickness distribution along the rolling direction. The lubricant is dragged into the contact sticking to the surfaces. The contact can be divided in three zones: the inlet, where the pressure builds up but the viscosity remains sufficiently small to enable viscous flow; the high pressure region, where the viscosity is so high that the lubricant is almost rigid; and the outlet, with the characteristic constriction.

---

[1] Looking at figure 1.2, the reader probably wonders what the link is between rolling element bearings and ten guys pulling a big stone lain on tree trunks. Well, it emerges from a literature survey starting 15 years ago with comics, that the figure 1.2 represents one of the oldest rolling-element-bearing-like documented applications (Iron Age).

Figure 1.2: Struggle against friction

1.1 Pollution

The contact life prediction is a major industrial issue. A large proportion of real mechanisms are subjected to contact deteriorations which affect their overall performance. Contact lives are important regarding economical aspects; the user safety is also sometimes involved. Increased understanding of the contact behavior has enabled improvement of the reliability and the efficiency of industrial or individual mechanisms. In most engineering applications, contact conditions become increasingly severe (higher loads, lower viscosities...). Some contradictory interests are involved: on one hand increasingly severe operating conditions and power loss diminution, and on the other, reliability and security improvements. To achieve the best compromise in design, the theoretical models have to be continuously improved.

Manufacturing processes have evolved during the last decades. A bearing which would have failed forty years ago because of very dangerous inclusions in the material, has more chance nowadays to fail because of surface defects (roughness...). Progress in material manufacturing has resulted in an in-

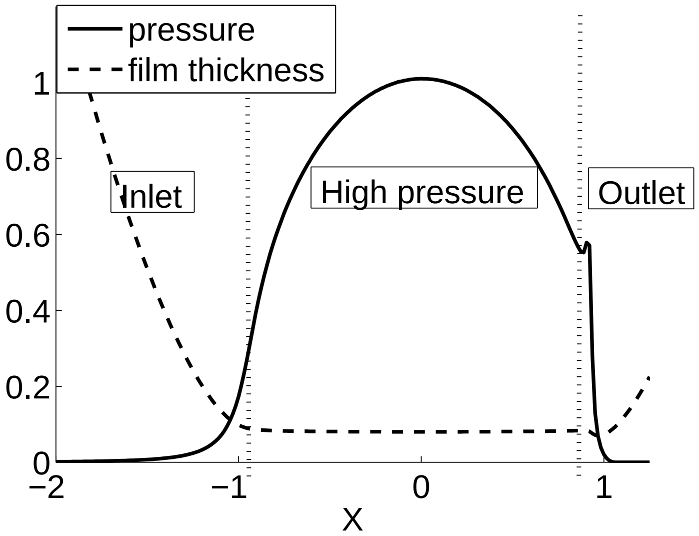

Figure 1.3: Typical EHL pressure distribution and film thickness along the rolling direction

crease in the relative importance of other failure sources, and especially the lubricant pollution problems. Ai [5] reports that almost 75% of premature bearing failures are related to pollution problems.

Lubricants contain particles. These particles are both initially present in the lubricant (due to manufacturing process, storage. . .); initially present in mechanisms (manufacturing residual particles. . .); generated during running in, wear and corrosion; or come from external sources (incomplete sealing and environment pollution, pollution during maintenance). The concentration, size and material properties of these particles can vary substantially, see Ai [5]. Ville [119] gives a simple example of the initial pollution of the same fresh oil which has been bought in a one liter packaging or two hundred liter packaging. The number of particles is multiplied by more than a factor four. Moreover, manufacturing residual particle specifications become more and more important. A strict process cleanliness is required to avoid particles exceeding 400 μm for series production bearings.

Very different particles can be encountered in real lubricants. Both the particle shape and properties can vary substantially. Table 1.1 briefly presents different particles encountered in real devices and their usual consequences. Figures 1.4 and 1.5 show a picture of ductile metallic spheres and fragile sand particles from Ville [119]. The bearing surface indentation caused by ductile metallic particles is the main object of this work.

Nature	**Origins**	**Frequency**	**Indentation**
metallic–ductile	machining, assembling, wear, damaging	very important for new parts, important during running-in	large and shallow indents (laminated particles)
carbides–tough	machining	moderate and limited to new parts	sharp and small indents (difficult to predict)
mineral–fragile	foundry sand, environment	limited to very important depending on the environment	very small indents (particle fracture)

Table 1.1: Particle origins and consequences on indentation [119]

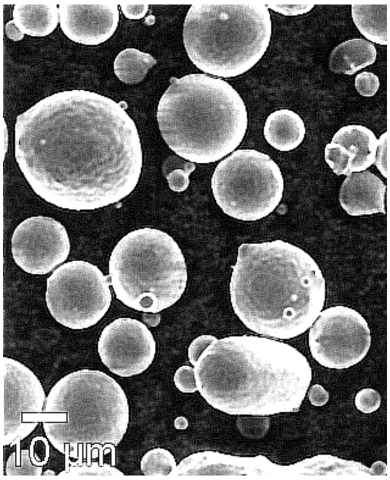

Figure 1.4: M50 particles [119] (distribution $0 - 100\ \mu m$)

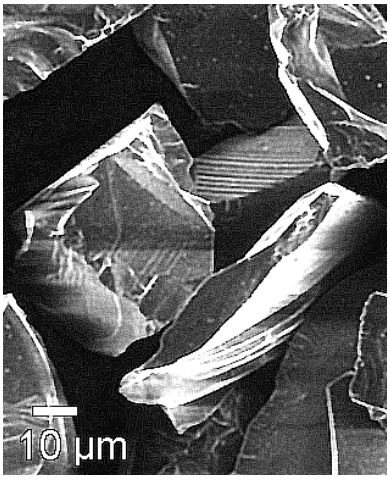

Figure 1.5: SiC particles [119] (mean size $45\ \mu m$)

These particles can be much larger than the film thickness. Typically, the particles can reach a few hundred micrometers, whereas the usual film thickness is less than one micrometer. When a particle enters the contact, it is squashed between the surfaces and plastically deforms them. The remaining deformed surface geometry (a hole surrounded by shoulders) is called an indent. The indents perturb the contact pressure distribution. These pressure perturbations cause additional stresses in the material; these additional stresses increase the fatigue failure risk (crack and spalling). Figure 1.6 represents a fatigue failure initiated in the vicinity of an artificial indent.

The magic solution to the pollution problem does not exist. Several possibilities are available: material development / thermochemical treatments, filters... However, even if all these approaches can bring great improvements in mechanism life, the failure prediction remains a question of great inter-

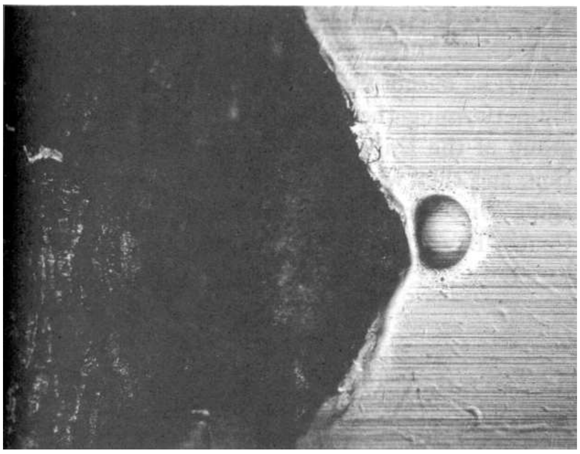

Figure 1.6: Spalling due to an artificial indent [82]

est. For example, a classical filtering size in the automobile industry is 40 m. Webster et al. [124] still report a ratio of 7 between the characteristic $L10$ life with a 40 μm filter and a 3 μm filter on a ball bearing life test bench. The use of very small filtering size is questionable because of the choking risk and the pressure drop. In this study, the aim is to predict indented contact life assuming: that the surface indentation is known, and that the material behavior is accounted for by an adjustment to experimental tests.

1.2 Modeling the pollution impact

1.2.1 Lubricant pollution and surface indentation

An important aspect is the link between a specific lubricant pollution and the indentation which will be observed on the surfaces. Several studies have been conducted concerning the link between the lubricant pollution and the surface indentation. On carefully designed experimental devices, under strictly controlled conditions, some clear conclusions have been obtained. A direct link between the particle concentration and the indent surface density has been established by Ville and Nelias [122].

However the next step, which consists in applying these results to real cases, is not trivial at all. For example, the study mentioned above contradicted results obtained by Dwyer-Joyce [37] who related a ratio between particle concentration and surface indentation density until 10 000 times higher.

Moreover, the relation between the indent geometry and the particle shape, the particle nature, the material behavior and the operating conditions is not clearly known. For example, the elastoplastic model which is used, strongly influences the calculated residual stresses. The prediction of the surface indentation from oil contamination in a real device is difficult. To be reliable, such a prediction in real cases would imply to know the concentration and the nature of particles which will enter the contact. It is not only strongly dependent of the particular bearing technology, but also from the polluted lubricant supply. Indeed, studies mentioned above, on the link between particle concentration and indentation density, have been obtained taking many precautions concerning the lubricant supply and the mixing of particles in the lubricant. Let us imagine the complexity of an automobile gear box lubricant repartition which is often ensured by oil projection and carter grooves...

Moreover, the way the particles will indent the surfaces depends on many parameters such as the material properties or the contact conditions. For example, Ville [119] shows the major impact of particle material (shallow and wide indent for ductile particle versus sharper and smaller indent for tough carbide particle). In this work, the surface indentation is supposed to be known. For example, from a real mechanism or from predenting process as presented by Nixon and Zantopoulos [93] or Girodin et al. [41], the surfaces can be analyzed using topography measures to quantify the indentation geometry and density. With such data, the contact lives can be estimated using the model developed in this work.

Figure 1.7 gives a glimpse of where this work is situated in the entire contact pollution problem. The example of an automobile gear box is taken. The surface indentation is assumed to be known. The contact condition and the indent geometry are numerically modeled to obtain the pressure and stress distribution. A life model is then used to predict the life from the stress distribution.

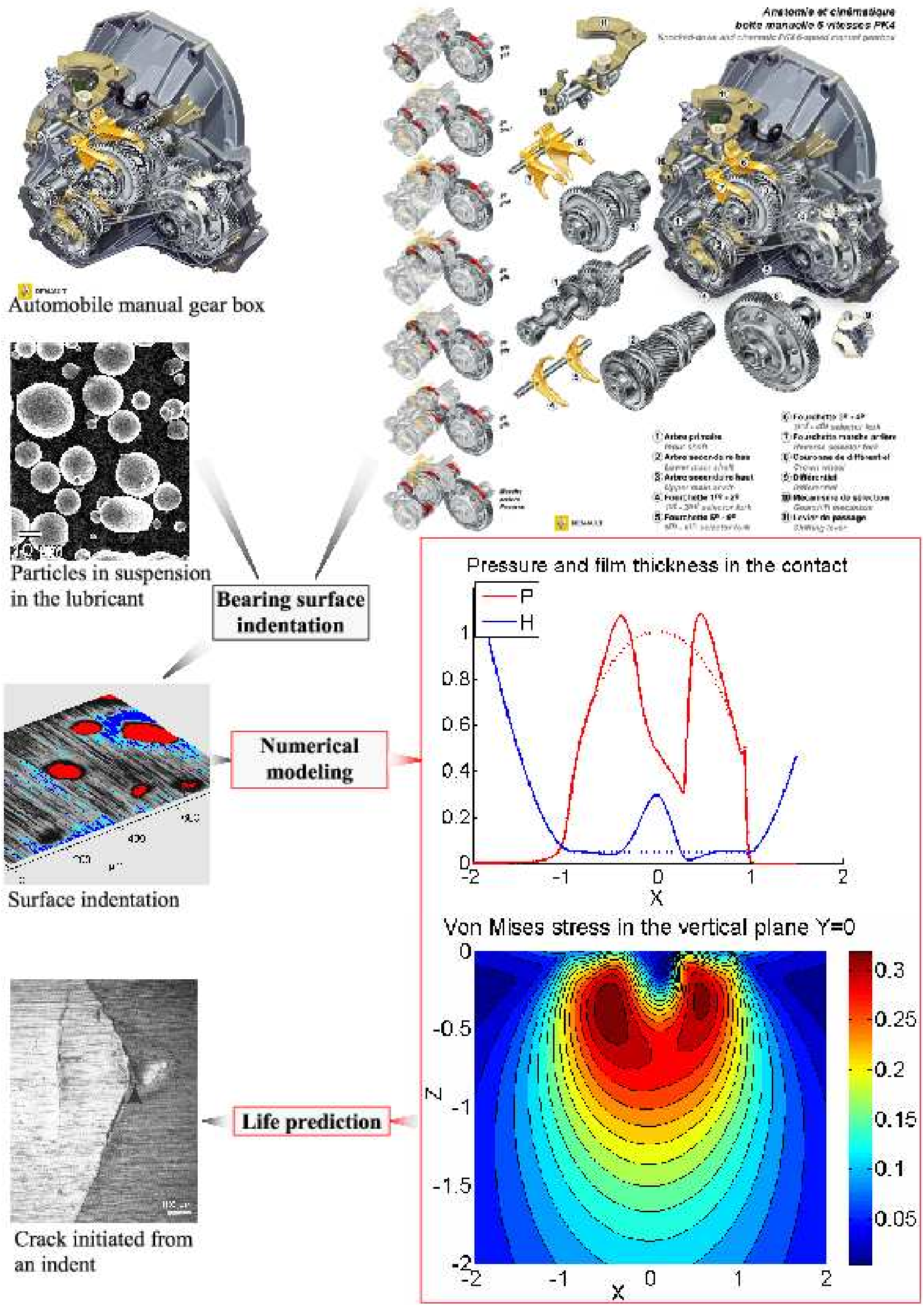

Figure 1.7: Pollution modeling in a real device

1.2.2 Life prediction

Prediction of rolling contact fatigue is complex. Many physical phenomena are coupled at different scales. This work is focused on the macroscopic pressure and the stress distribution in indented contacts.

One of the major problems is to account for the cumulative damage. At each loading cycle, the material is submitted to stress variations. A part of the energy provided to the material is converted in microstructural changes (dislocation movements, grain interactions, microstructural phase changes. . .) and other dissipative phenomena (heat generation, oil degradation. . .). This microscopic view has a physical basis. However, even with very simple loading cycles, the microscopic material behavior prediction is extremely difficult. Steel is an extremely complex material because of its heterogeneity, several phases coexists, various defects are randomly distributed, and the microstructure is not continuous at all at the grain scale and evolves with time and load cycles. Figure 1.8 represents the microstructure of a case carburized quenched $16NiCrMo13$ steel (residual austenite and martensite lath). However, a homogeneous and isotropic material will be considered in this work, the phenomena mentioned above are more or less averaged and, the variability will be accounted for by a statistical model see chapter 4.

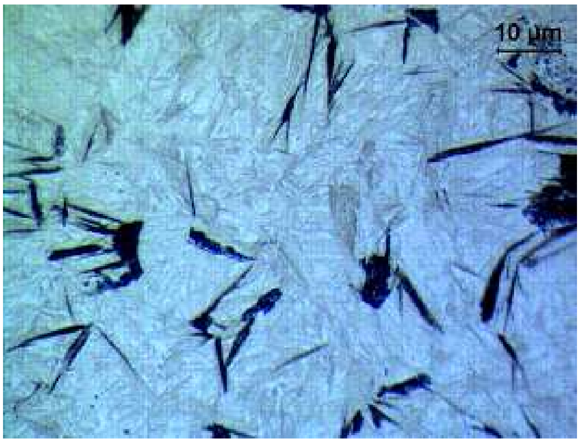

Figure 1.8: Microstructure of a case carburized quenched $16NiCrMo13$ steel [108]

Important variations are observed in contact life. Some variations can be attributed to complicated loading cycles and stress distributions, material properties, manufacturing process influence. . . With so many variables and coupled effects some restrictive assumptions have to be made. Neglecting some variation causes and considering intrinsically random material properties, implies to accept a large statistical dispersion in experimental results. The models used are idealized problems, and only attempt to highlight some of the principal physical trends and several order of magnitude variations.

Actually, the kind of theoretical models developed in this work have to be correlated with experimental validations.

The statistical dispersion is unavoidable for many reasons: the principal one is that the material defects such as inclusions are intrinsically randomly distributed and influenced by many parameters; the bearing geometry varies also; the operating conditions are not completely controlled; the defect shapes (such as indentations) are submitted to random distributions... All these aspects have to be kept in mind when looking at all the future considerations. Conclusions derived from models presented in this work have to be sufficiently significant to be experimentally correlated. It is irrelevant to highlight a 5% difference in the calculated life. Indeed, the 90% confidence band of a standard life test campaigns[2] is wide. If one repeats the standard life test, one will obtain several characteristic lives. The life interval which regroups 90% of the characteristic lives is spread roughly from half to twice the median value.

Finally, the intermediate step of the pressure analysis will be studied here for two main reasons: first, understanding the role of different parameters is easier when proceeding step-by-step (pressure distribution, subsurface stress, life reduction). Moreover, the pressure results do not depend on the fatigue life model. The calculated pressure distributions, which are already obtained using several assumptions, are certainly less questionable than fatigue lives and can be more easily experimentally validated.

1.3 Objectives

Different bearing technologies exist. The contact conditions can change enormously. So, a life prediction tool as accurate as possible is of great interest to avoid time consuming and expensive test campaigns. Moreover, for practical (and cost) reasons, the products are tested on a certain range of life and operating conditions. The extrapolation from these experimental data to a larger range of operating conditions is done using a theoretical model. The theoretical models developed here use three major steps: the development or the extension of numerical tools (elliptical dry contact pressure, transient elliptical EHL contact pressure, contact stress...), the analysis of the calculated results and the development of models.

This work focuses on three points considering the pressure and stress distribution: the ellipticity influence, the indent geometry including the shoulder role and the operating conditions. As explained previously, the final step of the life prediction is strongly dependent on material properties. So, only general trends will be presented.

- Chapter 1 gives the context and some limitations of this study. It

---

[2] six failures, in first in four tests

restricts the question of the life prediction of a bearing in a real device under polluted environment, to the simpler[3] question: knowing the indentation distribution (density and geometry), what will be the pressure and the subsurface stress distributions as a function of the operating conditions?

- Chapter 2 presents the dry contact and EHL contact models. It presents the main equations and a brief overview of the numerical techniques.
- Chapter 3 studies the contact ellipticity influence. It presents some conclusions about the contact ellipticity influence on the pressure distribution. The dry and EHL indented contact pressure distribution are compared. A dry contact pressure distribution model is presented. The lubrication condition influence is also detailed.
- Chapter 4 presents the stress distribution and life prediction results. The life model is presented.
- Chapter 5 summarizes this study and presents the future work.

---

[3] nevertheless sufficiently complex

Chapter 2

Modeling and numerical methods

2.1 Introduction

This work is a numerical study of indented contacts. The main equations are presented below. An effort will be made to point out the advantages and the limits of the models. The goal of this study is to predict indented contact behavior for a wide range of geometries and operating conditions. It means that hundreds of calculations are required. The other side of the coin is that some restrictive choices have to be made to be able to obtain these results in a reasonable time.

The EHL problem is governed by a complex set of equations. It requires a very detailed solution. A fine mesh implies a large number of unknowns and the solution time can become unacceptable unless advanced numerical techniques are used. The numerical techniques should enable to deal with the numerical difficulties of the set of equations. Moreover, obtaining a solution is not sufficient, an idea of the numerical error should be known as well. Below, an overview of the following aspects will be given: dry contact pressure, EHL contact pressure and subsurface stress distribution calculation.

2.2 Dry contact

The contact pressure distribution under dry contact conditions has been studied by Hertz [53]. The dry contact solution referred as Hertzian contact solution is considered as a limit case of lubricated contacts. Actually, when films become very thin and hydrodynamic effects decrease (high loads, low speeds, and low viscosities), the Hertzian pressure distribution is the asymptotic solution.

The Hertzian solution is the extension of the work of Boussinesq [13] who has formulated several assumptions: the bodies are semi-infinite half space (the contact zone is small compared with the body sizes); the bodies are elastic, homogeneous and isotropic; the stresses are normal to the surface.

The equations below will be presented twice: initial equations and dimensionless equations. The equations are solved using dimensionless variables for two main reasons: first, the dimensionless parameters enable to obtain variables of the order of magnitude of 1 which is crucial for numerical precision; second, they enable to use the opportunity of similarity groups.

2.2.1 Gap height equation

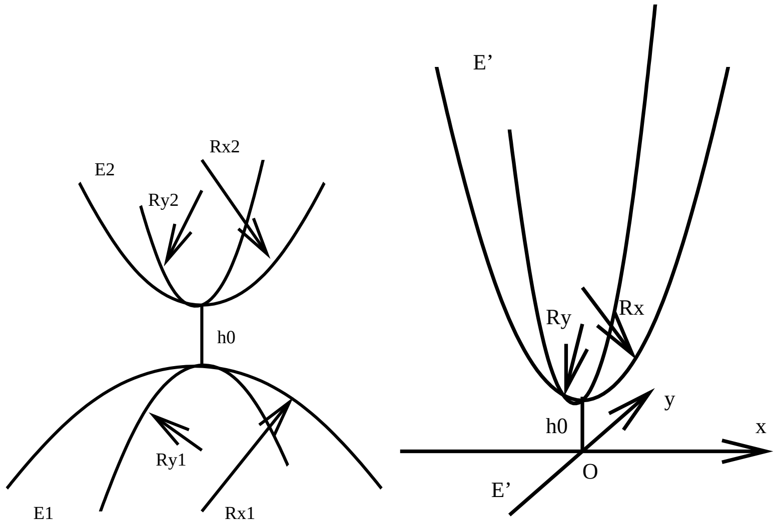

Figure 2.1: Contacting body geometries – real geometry (left) and equivalent geometry (right) [28]

The contacting body geometries can be well approximated by paraboloids because the contacting body radii of curvature are large in comparison with the contact dimensions. Since the surfaces are approximated by paraboloids, the equivalent radii of curvature R_x and R_y can be defined for a non-conforming contact by equation 2.1. Figure 2.1 represents, on the left the "real" geometry, and on the right the equivalent geometry.

$$\begin{aligned}\frac{1}{R_x} &= \frac{1}{R_{x1}} + \frac{1}{R_{x2}}\\ \frac{1}{R_y} &= \frac{1}{R_{y1}} + \frac{1}{R_{y2}}\end{aligned} \tag{2.1}$$

The gap height equation represents the separation between the two bodies. When the two bodies come into contact, a pressure is generated. The pressure deforms the initial undeformed surfaces. This deformation is calculated using the deformation integral which is function of the contact pressure over the domain Ω.

$$h\left(x,y,t\right) = h_0 + \frac{x^2}{2R_x} + \frac{y^2}{2R_y} + \mathcal{R}\left(x,y,t\right) + \frac{2}{\pi E'} \iint_\Omega \frac{p\left(x',y',t\right)\, \mathrm{d}x'\, \mathrm{d}y'}{\sqrt{\left(x-x'\right)^2 + \left(y-y'\right)^2}} \tag{2.2}$$

The term h_0 is the mutual approach of two remote points in the solids. The indent geometry will be introduced through $\mathcal{R}$. The equivalent Young modulus corresponds to:

$$\frac{2}{E'} = \frac{1-\nu_1^2}{E_1} + \frac{1-\nu_2^2}{E_2} \tag{2.3}$$

The dimensionless gap height equation reads:

$$H\left(X,Y,T\right) = H_0 + \frac{X^2}{2} + \frac{R_x}{R_y}\frac{Y^2}{2} + \bar{\mathcal{R}}\left(X,Y,T\right) + \frac{1+R_x/R_y}{2\pi\mathcal{E}} \iint_\Omega \frac{P\left(X',Y',T\right)\, \mathrm{d}X'\, \mathrm{d}Y'}{\sqrt{\left(X-X'\right)^2 + \left(Y-Y'\right)^2}} \tag{2.4}$$

$$\kappa\left(\frac{R_x}{R_y}\right) \approx \frac{1}{1 + \sqrt{\dfrac{\ln\left(16/\dfrac{R_x}{R_y}\right)}{2\dfrac{R_x}{R_y}} - \sqrt{\ln 4} + 0.16\ln\dfrac{R_x}{R_y}}} \tag{2.5}$$

$$\mathcal{E}\left(1-\kappa^2\right) = \int_0^{\frac{\pi}{2}} \sqrt{1 - \left(1-\kappa\right)^2 \sin^2\psi}\ \mathrm{d}\psi \tag{2.6}$$

$$\mathcal{E}\left(1-\kappa^2\right) \approx \frac{\pi}{2}\,\kappa^2\left(1 + \frac{2\left(1-\kappa^2\right)}{\pi\kappa^2} - 0.125\ln\kappa^2\right) \tag{2.7}$$

The elliptical integral approximation $\mathcal{E}$ in equation 2.7 is from Hamrock and Brewe [52] and Moes [88]. For circular contacts, $R_x/R_y = 1$, the elliptical integral $\mathcal{E}$ tends asymptotically to $\pi/2$ while the ellipticity κ becomes 1.

$$\mathcal{E}\,(0) = \frac{\pi}{2} \tag{2.8}$$

2.2.2 Force balance equation

The force balance equation represents the load equilibrium. The applied load is compensated by the pressure which is generated on the surfaces. The force balance is considered in a quasi-static approximation. It means that no inertia is considered, and the load balance is exactly and immediately verified.

$$\iint_{\Omega} p\,(x, y, t)\ \mathrm{d}x\ \mathrm{d}y = w \cdot f(t) \tag{2.9}$$

The dimensionless force balance equation reads:

$$\iint_{\Omega} P\,(X, Y, T)\ \mathrm{d}X\ \mathrm{d}Y = \frac{2\pi}{3\kappa} \cdot f(t) \tag{2.10}$$

2.3 EHL contact

The fundamental equation of thin film lubrication has been established by Reynolds [98]. This equation is derived from the Navier-Stokes fluid dynamics equations using some simplifications and assumptions. The major shortcuts are: a very thin lubricant film thickness in comparison with the contact dimensions, a continuous fluid which sticks to the surfaces, a laminar flow, a constant pressure through the film thickness, volume and surface forces are neglected in comparison with viscous forces. The Reynolds equation describes the mass flow conservation of a viscous fluid flow between two parallel surfaces. It links the pressure to the contact geometry and the lubricant properties.

A major step forward in EHL understanding was in the work of Ertel [38] the combination of Hertzian solution and a piezoviscous lubricant behavior from the work of Barus [8]. The first numerical solution of an EHL contact is proposed by Petrusevich [96] who solved simultaneously the elastic deformation and the Reynolds equation. The smooth contact film thickness study was published by Dowson and Higginson [32] for line contacts; and later by Hamrock and Dowson for elliptical contacts [49, 50, 51].

The experimental measurement were improved with the interferometric techniques. The gap height between the two surfaces is reconstituted from the interference pattern of light rays see Gohar and Cameron [43] and Foord et al. [40]. Thin film measurements (5 nm) were made possible by Johnston et al. [68].

The EHL contact equations are complex. Three equations are simultaneously solved: the two previous dry contact equations (gap height equation 2.4 and force balance equation 2.10) and the Reynolds equation. This set of equations presents some pathological behaviors:

- A strong coupling between these three equations: for example, a modification of the mutual approach from the force balance equation induces a global variation of the film thickness and so, of the pressure distribution.
- Very non-linear behavior of the viscosity with pressure.
- Nature change of the Reynolds equation between low and high pressure regions (from elliptical to hyperbolic).
- The integral part of the elastic deformation equation: a pressure variation in a single point affects the entire deformed geometry.

A major step forward in the solution of these equations is due to the development of multigrid techniques by Brandt [14, 15]. These techniques were applied to the EHL problem by Lubrecht [79, 80, 81]. To speed up the elastic deformation calculation, Brandt and Lubrecht [16] developed the multigrid multi-integration scheme (MLMI). Venner [109] optimized the relaxation process of the multigrid solver. The improvement concerning the stability and the convergence speed enabled to solve transient problems.

The transient problem has been studied for various geometrical patterns and especially harmonic roughness, see Lubrecht [86], Venner [110, 112, 111, 113, 114]. A different approach is developed by Greenwood [44, 45] and Morales-Espejel [89]. Hooke [54, 55, 56] proposed several studies where the importance of the ratio between the geometry wavelength and the inlet length is highlighted. Ai [1] calculates the effect of a moving indent traversing an EHL contact.

The experimental validation was done in parallel of the development of high speed camera and interferometric measurement Kaneta et al [71, 72], Wedeven and Cusano [126]. The lubricant behavior is at center of attention of latest developments, see Chapkov [18, 19] and Hooke [61, 62]. An important number of publications are also related to the microgeometry optimization as a function of the operating conditions by surface texturing (especially on coatings), both on numerical and experimental aspects [123], [90]. The lack of lubricant referred as starved contacts is also numerically studied for example by Chevalier [22] and Damiens [28].

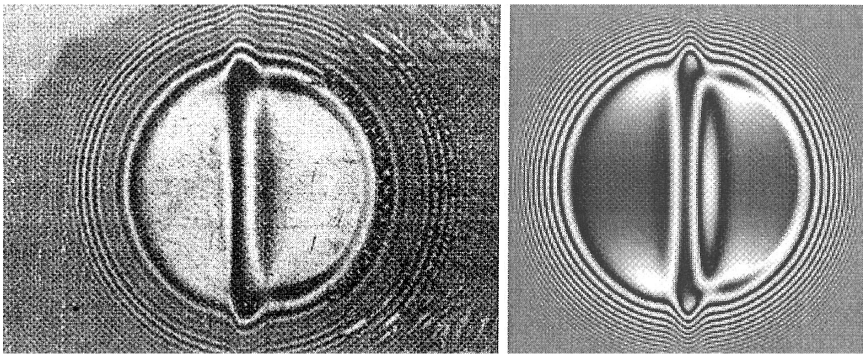

Figure 2.2: Comparison of experimental (left) and numerical (right) results of a transverse ridge under pure-rolling, experimental result by Kaneta [71] and numerical result by Lubrecht [110]

2.3.1 Lubricant

An important aspect of the EHL lubrication is the lubricant behavior. The operating conditions are extreme in terms of pressure (several GPa) and sometimes shear rate. Some very sophisticated lubricant behavior model exist. For example, the lubricant viscosity-pressure relationship η is often very dependent on the shear rate. However, for the range of small slide to roll ratio (encountered in rolling element bearings $< 5\%$), a simple model of Newtonian behavior is a reasonable simplification. Moreover, with a zero or small sliding speed, the thermal effects are expected to be small and will be negliged.

The Roelands viscosity [99] is used:

$$\begin{aligned} \overline{\eta}\left(P\right) = \frac{\eta}{\eta_0} &= e^{\frac{\alpha p_r}{\mathbf{z}}\left(-1+\left(1+\frac{Pp_h}{p_r}\right)^{\mathbf{z}}\right)} \\ \frac{\alpha p_r}{\mathbf{z}} &= \ln \eta_0 + 9.67 \\ p_r &= 1.96\ 10^8 \end{aligned} \tag{2.11}$$

The fluid compressibility appears to have a small effect on the indented contact behavior. The simplest and most common density relation, which was proposed by Dowson and Higginson [33], is used:

$$\overline{\rho} = \frac{\rho}{\rho_0} = \frac{0.59 \cdot 10^9 + 1.34 \cdot Pp_h}{0.59 \cdot 10^9 + Pp_h} \tag{2.12}$$

2.3.2 Reynolds equation

The Reynolds equation is written for a constant speed, the transient term comes from non smooth patterns traversing the contact:

$$\frac{\partial}{\partial x}\left(\frac{\rho h^3}{\eta}\frac{\partial p}{\partial x}\right)+\frac{\partial}{\partial y}\left(\frac{\rho h^3}{\eta}\frac{\partial p}{\partial y}\right)=12\,u_m\frac{\partial \rho h}{\partial x}+12\,\frac{\partial \rho h}{\partial t} \tag{2.13}$$

To make the Reynolds equation dimensionless, the parameter $\bar{\lambda}$ is defined in equation 2.15. The transient dimensionless Reynolds equation with a Newtonian fluid reads:

$$\frac{\partial}{\partial X}\left(\frac{\overline{\rho}H^3}{\overline{\eta}\overline{\lambda}}\frac{\partial P}{\partial X}\right)+\frac{\partial}{\partial Y}\left(\frac{\overline{\rho}H^3}{\overline{\eta}\overline{\lambda}}\frac{\partial P}{\partial Y}\right)=\frac{\partial \overline{\rho}H}{\partial X}+\frac{\partial \overline{\rho}H}{\partial T} \tag{2.14}$$

$$\overline{\lambda}=\frac{12\,u_m\eta_0R_x^2}{b^3p_h} \tag{2.15}$$

2.4 Subsurface stress distribution

The contact elastic tensor (CET) is defined as the elastic stress distribution associated with the deformation in the contact. One can approximate the CET in each point of the semi-infinite half space which is submitted to a given pressure field on the top surface. The influence coefficient method is used to compute the stress integrals. The problem is solved by meshing the loaded region on the top surface as a finite union of squares. The kernels used in those integrations are deduced from Boussinesq and Cerruti equations [13]. The CET is calculated assuming homogeneous and isotropic bodies, small deformations and linearity between deformations and stresses.

MLMI techniques are used to calculate the integrals of the elastic stress field to ensure a reasonable calculation time. The scheme used is from Lubrecht [84] with appropriate kernels, see Kalker [69]. The domain has been meshed as shown in the figure 2.3 to ensure both a sufficient discretisation of the high gradient region (close to the surface) and a coarser meshing deeper (to maintain reasonable calculation times). The contact pressures and subsurface stresses are calculated assuming no friction at the surface. The principal stresses are calculated according to Fenner [39].

The residual stress distribution and the contact elastic stress distribution due to indent pressure perturbations are considered separately. The residual stress is the stress distribution in the material without any loading obtained after running-in. The real stress state in the material during loading is the sum of the residual stress distribution and the CET.

To predict the residual stress field one needs several steps: initial residual stress of the bodies (manufacturing residual stress, thermochemical treatment residual stress, hoop stress), the elastoplastic behavior of the two

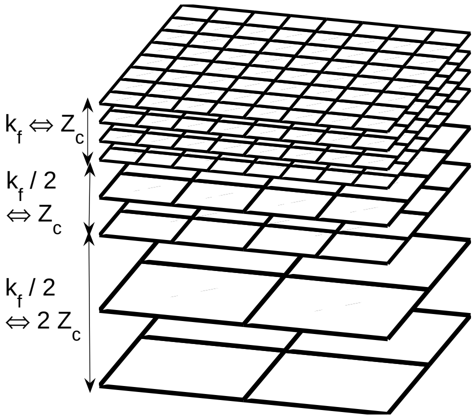

Figure 2.3: Stress meshing

bodies and the particles, the particle geometry and nature, the indentation residual stress, the running-in residual stress (geometry stabilization). Moreover, as said in section 2.5, the particle indentation modeling is still a challenging problem. The indentation conditions are generally not known.

Finally, the residual stress distribution will be omitted. Two main justifications can be given. Firstly, it would be very costly considering the number of parameters (and so, very time-consuming). For example, elasto-plastic calculations would no longer remain dimensionless… Secondly, most of the fatigue criteria are based on the stress amplitude seen by the material. The residual stress is expected to be stabilized very quickly in comparison of the contact life. With a fatigue criterion like the Dang Van criterion [29], the residual stresses do not act on this stress amplitude because it is a constant stress tensor shift. The impact is only on the residual hydrostatic stress. The validity of this particular point for high compressive hydrostatic stress is contested see Desimone et al. [30].

2.5 Indent geometry

EHL film thickness is classically thinner than one micrometer. Pollution particles can reach few hundreds of micrometers. When these particles enter the contact, they are squashed between the two surfaces. The particles plastically deform the two surfaces and the remaining geometry is called an indent. The indent geometry is difficult to predict. Several numerical and experimental studies treat the indent geometry aspect. These studies use both artificial indents (Rockwell indenter) or natural indents (polluted contact).

The understanding of the indent creation is interesting for two reasons: first, the pressure and stress perturbations induced by an indent traversing a contact depend obviously on its geometry; second, the indentation residual stress can be correctly evaluated.

2.5.1 Natural indentation observations

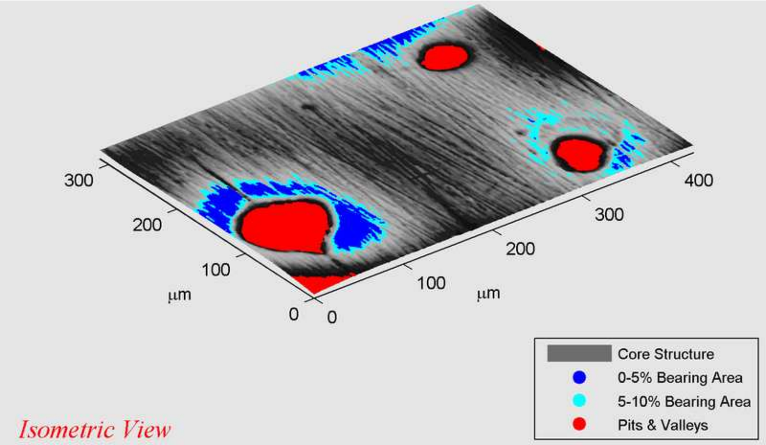

Figure 2.4: Ductile particle indent 3D mapping by Cogdell [23]

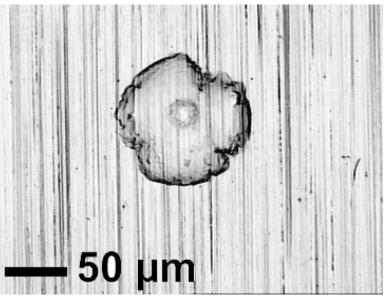

Figure 2.5: Ductile particle indent [119]

A comprehensive study of the indentation especially with ductile particles was made by Ville [119]. Some of the results are reported and are linked to some experimental observations in tapered roller bearings performed by Cogdell at the Timken company metrology laboratory.

Ville [119] describes the major impact of the particle nature (ductile, fragile, tough) and the operating conditions (especially sliding) on the indentation. For example, brittle particles (sand) explode in the contact inlet and produce numerous small indents; tough ceramic (carbide) particles produce sharp indents and seem to be a harmful type of contaminant; the metallic – ductile spheres produce large shallow indents, see figure 2.4, 2.5. For pure-rolling conditions and ductile particles, these indents are roughly axysymmetrical. The shoulder height seems to be a little higher on the rear shoulder.

- The Hertzian pressure seems to have a small influence on the indent geometry.
- The particle diameter has an important influence on the indent diameter, however a more moderate influence on the indent depth.
- The mean velocity has a moderate impact on the indent depth and diameter. The difference concerning the indent depth seems to be linked with the central film thickness variation. Moreover, the indent shoulders are much higher with decreasing speed.
- The slide to roll ratio has a very important impact on the indent geometry. The indent shape becomes very irregular and stretched along the sliding direction even for small slide to roll ration (6%).

Particle diameter (μm)	**10-20**	**20-32**	**32-40**	**40-50**
Indent diameter (μm)	20-30	30-40	40-80	60-100
Indent depth (μm)	1.5-1.7	1.7-1.8	1.8-3.0	2.0-3.0
Indent slope (°)	8.7-6.7	6.7-5.2	5.2-3.8	3.8-3.0

Table 2.1: Experimental observation of the indent diameter, depth and slope as function of the particle diameter [119]

Table 2.1 represents the indent slope and diameter distribution as a function of the particle size. These measures have been obtained by Ville [119] on a twin disc pollution bench. The particles are $M50$ spheres, they cross once the contact creating a unique indent. Pure-rolling conditions have been used. The discs are made of 52100 steel with a similar hardness as the particles. When the particle size increases, the indent diameters are larger and the indent slopes are shallower. Observations of bearings which have run under controlled polluted environment show also that the sharpest indents are systematically the smallest.

For a given class of particle diameters, the variation of the indent geometry is relatively limited. Moreover, the results presented above have been obtained ensuring that the particles traverse only once the contact. However, when a particle traverses several times the contact, it creates each time a shallower indent. In a rolling element bearing, particles can be trapped in the bearing and traverse many contacts. It can be an explanation why numerous very shallow indents are measured on the surfaces of a bearing which runs under controlled polluted environment.

2.5.2 Indent creation modeling

Artificial indentations (Rockwell indenter) have been modeled in several studies. The indentation residual stress influence on contact life which is studied by Ko and Ioannides [74], Lubrecht et al. [85], Xu et al. [129]. The authors observe a moderate impact of the indentation residual stress distribution, only Hamer et al. [48] predicts an important impact. For dry contacts or pure-rolling EHL contacts, the residual stresses have a beneficial effect on calculated life. The predicted life can roughly be multiplied at the most by a factor four (for low loads, and almost constant for high loads and/or very severe indents). At first sight, it could seem important but the reduction in life presented in these studies between smooth and indented contacts is about 10^3. The calculated indentation is strongly dependent on the material properties (elastoplastic behavior). The friction coefficient seems to have no influence on the indent hole, and a moderate influence on the shoulder geometry, see Nelias et al. [92].

However, concerning natural indentation, the study conducted by Kang et al. [73] shows that the friction coefficient between the particle and the bodies seems to have an important effect on the dent geometry. Particle indentation is also studied by Sayles and Ioannides [103], and Xu et al. [129] who confirm the moderate impact on indented contact life of the indentation residual stress.

2.5.3 Analytical description

Indents present a hole surrounded by shoulders. The indent geometry has to be modeled as precisely as possible, but keeping a reasonable number of parameters. Two problems are encountered: First, the indent geometry depends on the operating conditions (nature of particles, sliding, . . .); second, the indent geometry evolves during the bearing life. When an indent is created, the initial indent geometry evolves during a few thousand overrolling cycles until the pressure perturbations around the indent induce only elastic deformations. It leads to the stabilized geometry. It is assumed that only very few cycles compared to the total life are sufficient to obtain the stabilized geometry, which will be subjected to high cycle fatigue, see Bhargava et al. [9, 10], Hahn et al. [47], Coulon [24].

Two major approaches exist, on one hand, the use of the measured indent geometry and on the other, the use of simplified geometries such as analytical indent geometry. The use of measured geometries has two disadvantages. First, the quality of the solution is not easy to evaluate and second, general trends are difficult to extract. The analytical indent description used in this work is obviously an important simplification, see figure 2.6. However, it enables a parametric study (reduced number of parameters). The continuous geometry facilitates the numerical accuracy. Finally, the analysis uses the indent geometry used by Coulon [24] which uses three parameters, see equation 2.16.

$$\bar{\mathcal{R}} = -De^{-K\frac{R^2}{\Phi^2}} \cos\left(\frac{\pi R}{\Phi}\right) \tag{2.16}$$

These three parameters control the indent shape: the diameter Φ, the depth D and the attenuation factor K for the shoulder shape. The analytical function 2.16 is a good compromise between the number of parameters, the correct emulation of the indent geometry and good numerical properties. Real surface indents under polluted environment present so many different geometries (variability in particle nature, size, operating conditions, ...) that for the moment, no clear observation justifies a more sophisticated analytical description.

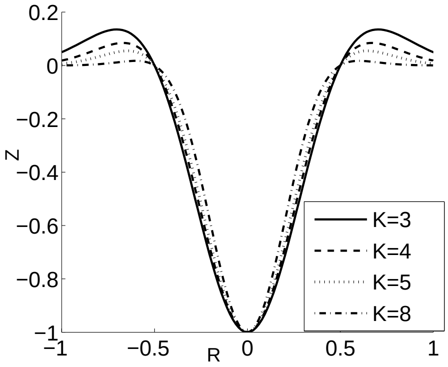

Figure 2.6: Indent profiles for different decay coefficients K from 3 to 8, $D = 1, \Phi = 1$

2.6 Numerical techniques

Following the modeling, the continuous equations have to be solved. These continuous equations are too complex to find an analytical solution, so the equations are discretised and the discrete solution computed in nodes of a mesh grid. The accuracy of this step is determined by the discretisation error. The equations are solved using an iterative process. At each iteration, the variables converge to the solution. The difference between the last iteration and the discrete solution is the numerical error.

The first crucial point in a numerical study is to ensure that the solution represents accurately the continuous equations. In other words, the error which comes from the numerical techniques used to solve the continuous problem, should be controlled. The solution trends should be caused by the physical parameter variations, not by numerical artifacts. An example of a numerical artifact is clearly demonstrated by Venner [116] where artificial trends for low speeds in EHL contacts appear as a result of poor accuracy.

The end of this chapter is a very quick overview of the basics of the numerical techniques used in this work. A complete description and analysis can be found in the literature especially Venner and Lubrecht [115]. This work started with the implementation of the transient terms in the EHL multigrid solver: the Gauss-Seidel line relaxation and the distributive Jacobi line relaxation. Validation of the numerical accuracy is also presented.

The solution of the EHL equations requires: first, a fine meshing which implies a large number of unknowns N; second, numerical techniques which can overcome pathological behavior of these equations (especially in terms of stability); finally, efficiency in terms of computation time. The notion of algorithm complexity is at the heart of the problem[1].

2.6.1 MLMI principles

The calculation of the deformation integral and of the stress integrals are made using the technique of influence coefficients. The calculation of the deformation integral and of the stress integrals corresponds to a convolution between an integration kernel K (influence coefficients) and the pressures $P_{i,j}$. The kernel gives the influence of a ponctual pressure in every point of the half-space domain. A naive implementation of these integrals gives a complexity of N^2 for the deformation integral. MLMI[2] enables a complexity of $N \cdot ln(N)$ for the deformation integral.

The main idea consists in taking advantage of the kernel smoothness. The kernel involved here are asymptotically smooth kernels. It means that the kernel gradient can become very small far from the singularity. In this conditions, the kernel can be interpolated with a negligible accuracy lost. The crucial point is to note that the smoothness assumption is only made on the kernel, and not on the pressures. This subtlety is referred as anterpolation [115]. In the zones where the kernel is not smooth enough, a correction

---

[1] The answer of the increasing computer speed is deceptive. For example, a fine 2D discretisation of 1024×1024 points corresponds to 2^{20} unknowns. A classic algorithm with a complexity of N^2 requires 2^{40} operations. An "efficient" algorithm with a complexity of $N \cdot ln(N)$ requires roughly 2^{24} operations. If the efficient method solves the problem in one minute, it means that the classic algorithm will require about one month and half. The CPU speed increase is expected to reach its limit in 10 to 15 years. Anyway, in 15 years, CPU should be roughly 2^{10} faster. So don't hold your breath, it means that you still will have to wait more than one hour to obtain your result.

[2] MultiLevel-Multi-Integration

is used. The correction has a complexity cost, so the correction has to be made only when a gain is obtained on the discretisation error.

The continuous integral is:

$$w(x) = \int_\Omega K(x,y)u(y)\,dy \tag{2.17}$$

A piecewise integration is used:

$$w_{i,j}^h = h^d \sum_j K_{i,j}^{hh} u_j^h \tag{2.18}$$

$$w_{i,J}^H = H^d \sum_j K_{i,J}^{hH} u_J^H \tag{2.19}$$

$$u_J^H = 2^{-d}[(I\!I_H^h)^T u_\cdot^h]_J \tag{2.20}$$

Then, the fine grid integral $w_{i,j}^h$ is approximated by the coarse grid integral $w_{i,J}^H$ and a correction is applied around the singularity:

$$w_i^h \simeq w_I^H + h^d \sum_{|j-i|\leqslant m} (K_{i,j}^{hh} - \tilde{K}_{i,j}^{hh}) u_j^h \tag{2.21}$$

$$\tilde{K}_{i,j}^{hh} = [(I\!I_H^h) K_{i,\cdot}^{hH}]_j \tag{2.22}$$

The deformation kernel is calculated using the equations 2.23 and 2.24. The stress kernels can be found in [69].

$$\begin{aligned} K_{i,j,k,l} = \frac{2}{\pi^2}\Big(& |X_p|\,\mathrm{asinh}\frac{Y_p}{X_p} + |Y_p|\,\mathrm{asinh}\frac{X_p}{Y_p} + |X_m|\,\mathrm{asinh}\frac{Y_m}{X_m} + |Y_m|\,\mathrm{asinh}\frac{X_m}{Y_m} \\ & - |X_m|\,\mathrm{asinh}\frac{Y_p}{X_m} - |Y_p|\,\mathrm{asinh}\frac{X_m}{Y_p} - |X_p|\,\mathrm{asinh}\frac{Y_m}{X_p} - |Y_m|\,\mathrm{asinh}\frac{X_p}{Y_m}\Big) \end{aligned} \tag{2.23}$$

$$\begin{aligned} X_p &= X_i - X_k + \frac{h_X}{2} & Y_p &= X_j - X_l + \frac{h_Y}{2} \\ X_m &= X_i - X_k - \frac{h_X}{2} & Y_m &= X_j - X_l - \frac{h_Y}{2} \end{aligned} \tag{2.24}$$

2.6.2 Multigrid principles

The discrete problem is solved iteratively. Each iteration is called a relaxation. A crucial aspect of the relaxation process used is that the high frequencies of the error converge much faster than the low frequencies. It means that after few relaxations the high frequencies of the error have vanished whereas the lower frequencies remain unchanged. The multigrid algorithm uses this characteristic. The algorithm works on several levels which corresponds to different mesh sizes. It is much more efficient for two reasons: first, obviously a coarser grid is synonym of less unknowns and a smaller amount of work per relaxation; second, the ratio between the error wavelength and the mesh size decreases and a low frequency on the fine grid corresponds to a less smooth error on a coarse grid. It means that the coarser levels will speed up the convergence of the low frequencies of the error.

The EHL problem is non linear so the Full Approximation Scheme (FAS) has to be used.

FAS scheme

A general way of writing a differential equation is:

$$\mathcal{L}\left\langle u\right\rangle = f \tag{2.25}$$

with:

- $\mathcal{L}$ – continuous differential operator
- u – continuous unknown
- f – continuous right hand side function (known)

After discretisation on a grid with mesh size h, the discrete equation reads:

$$\mathcal{L}^h\left\langle \underline{u}^h\right\rangle = \underline{f}^h \tag{2.26}$$

with:

- $\mathcal{L}^h$ – discrete differential operator
- $\underline{u}^h$ – discrete unknown
- $\underline{f}^h$ – discrete right hand side function (known)

The resolution starts, the initial unknown $\hat{\underline{u}}^h$ is transformed after each relaxation in the incompletely converged unknown $\tilde{\underline{u}}^h$. The exact solution of the discrete problem is $\underline{u}^h$. It enables to define the residual $\underline{r}^h$ and the numerical error $\underline{v}^h$.

$$\underline{r}^h = \underline{f}^h - \mathcal{L}^h\left\langle \tilde{\underline{u}}^h\right\rangle \tag{2.27}$$

$$\underline{v}^h = \underline{u}^h - \tilde{\underline{u}}^h \tag{2.28}$$

Substituting equations 2.27 and 2.28 in 2.26 gives:

$$\mathcal{L}^h\left\langle \underline{\tilde{u}}^h + \underline{v}^h \right\rangle = \mathcal{L}^h\left\langle \underline{\tilde{u}}^h \right\rangle + \underline{r}^h \tag{2.29}$$

The coarse grid H is now used to calculate a correction to apply to the fine level h. The restriction and interpolation operators are respectively I_h^H and I_H^h.

$$\begin{aligned} \mathcal{L}^H\left\langle \underline{\hat{u}}^H \right\rangle &= \underline{\hat{f}}^H && (2.30)\\ \underline{\hat{u}}^H &= I_h^H \underline{\tilde{u}}^h + \underline{v}^H && (2.31)\\ \underline{\hat{f}}^H &= \mathcal{L}^H\left\langle I_h^H \underline{\tilde{u}}^h \right\rangle + I_h^H \underline{r}^h && (2.32) \end{aligned}$$

After a number of relaxations on the coarse grid, a good approximation $\underline{\tilde{u}}^H$ to the coarse grid variable $\underline{\hat{u}}^H$ is found. The fine grid old approximation $\underline{\tilde{u}}^h$ is then corrected according to:

$$\underline{\bar{u}}^h = \underline{\tilde{u}}^h + I_H^h(\underline{\tilde{u}}^H - I_h^H \underline{\tilde{u}}^h) \tag{2.33}$$

This scheme is applied recursively on several grid levels see figure 2.7, typically on five levels from 256 grid points for the finest grid to 16 points for the coarsest grid. The choice of intergrid transfer operators is not without consequences, see [115]. An efficient way to obtain a first guess of the unknown on the finest grid is to solve at lower cost the problem on coarser grids and interpolate it recursively on finer grids. This scheme is referred as Full Multigrid Cycle (FMG), see figure 2.8.

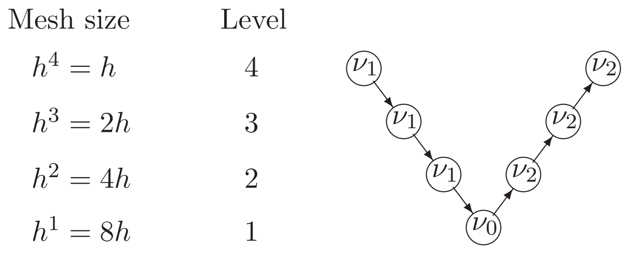

Figure 2.7: Example of a $V(\nu_1, \nu_2)$-cycle with 4 levels [115]

Line relaxation

As said previously, the efficiency of the relaxation process is strongly dependent on the error wavelength. It is detailed in the local mode analysis in [115]. A local relaxation scheme is used. The equation will be discretised

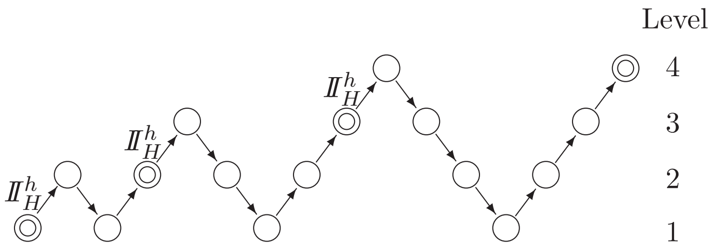

Figure 2.8: FMG with one V-cycle [115]

using finite differences. It means that the discrete equations in the grid point i, j will only make appear few neighboring unknowns. As the equations are non linear, a local linearisation is used. The current approximation $\tilde{u}^h_{i,j}$ in the grid point i, j will be corrected in $\overline{u}^h_{i,j}$ by the correction $\delta^h_{i,j}$:

$$\overline{u}^h_{i,j} = \tilde{u}^h_{i,j} + \omega \delta^h_{i,j} \tag{2.34}$$

$$\delta^h_{i,j} = \left(\frac{\partial \mathcal{L}^h \left\langle \underline{u}^h \right\rangle_{i,j}}{\partial\, u^h_{i,j}} \right)^{-1}_{\underline{u}^h = \underline{\tilde{u}}^h} r^h_{i,j} \tag{2.35}$$

Relaxing every points of the grid, if the very last corrected values are used, a Gauss-Seidel relaxation is performed; if the corrected values are updated only at the end of each grid relaxation, a Jacobi relaxation is performed.

The EHL equations present a strong coupling in the direction X. Instead of solving the equations changing one unknown at the time, a line relaxation can be performed. It means that the corrections of the locally linearised problems will be calculated on an entire line. An important gain in the relaxation efficiency is obtained. A smart choice of the important coupling terms enable to obtain an hexadiagonal linear problem with n_X unknowns which can be solved without impairing the overall complexity:

$$A^j \underline{\delta}^h_j = \underline{r}^h_j \tag{2.36}$$

with:

- A^j – hexadiagonal linear system matrix
- $\underline{\delta}^h_j$ – correction in all points i of the line j
- $\underline{r}^h_j$ – residual in all points i of the line j

It has been shown in section 2.6.1 that the deformation in one point is a function of the pressures in all grid points through the influence coefficient matrix. It means that a change in pressure in one grid point will affect all the other grid points through the deformation integral. It leads to important numerical difficulties (convergence and stability). To overcome this, the distributive relaxation is used in the high pressure zone. The distributive relaxation is based on the deformation kernel properties. The influence of a local change in pressure on the deformation in the other grid points is limited by the distributive relaxation. When a correction is applied in one grid point, an opposite smaller correction in the other direction is applied to the neighboring points. Two schemes are employed, the Gauss-Seidel line relaxation for the low pressure zones and the distributive Jacobi line relaxation for the high pressure zones.

$$\underline{\overline{r}}_j^h = \underline{f}_j^h - \mathcal{L}^h \left\langle \ldots; \underline{\overline{u}}_{j-1}^h; \left\langle \ldots; \overline{u}_{i-1,j}^h; \tilde{u}_{i,j}^h; \tilde{u}_{i+1,j}^h; \ldots \right\rangle; \underline{\tilde{u}}_{j+1}^h; \ldots \right\rangle \tag{2.37}$$

$$\underline{\tilde{r}}_j^h = \underline{f}_j^h - \mathcal{L}^h \left\langle \ldots; \underline{\tilde{u}}_{j-1}^h; \left\langle \ldots; \tilde{u}_{i-1,j}^h; \tilde{u}_{i,j}^h; \tilde{u}_{i+1,j}^h; \ldots \right\rangle; \underline{\tilde{u}}_{j+1}^h; \ldots \right\rangle \tag{2.38}$$

Depending on which relaxation scheme is used, the correction matrix system is constructed:

- Gauss-Seidel line relaxation:

$$A^j \underline{\delta}_j^h = \underline{\overline{r}}_j^h \tag{2.39}$$

$$A_{i,k}^j = \frac{\partial \mathcal{L}^h \left\langle \underline{u}^h \right\rangle_{i,j}}{\partial u_{k,j}^h} \tag{2.40}$$

$$\underline{\overline{u}}_j^h = \underline{\tilde{u}}_j^h + \omega_{GS}\, \underline{\delta}_j^h \tag{2.41}$$

- Jacobi distributive line relaxation:

$$A^j \underline{\delta}_j^h = \underline{\tilde{r}}_j^h \tag{2.42}$$

$$\begin{aligned} A_{i,k}^j = {} & \frac{\partial \mathcal{L}^h \left\langle \underline{u}^h \right\rangle_{i,j}}{\partial u_{k,j}^h} - \frac{1}{4} \left(\frac{\partial \mathcal{L}^h \left\langle \underline{u}^h \right\rangle_{i,j}}{\partial u_{k+1,j}^h} + \right. \\ & \left. \frac{\partial \mathcal{L}^h \left\langle \underline{u}^h \right\rangle_{i,j}}{\partial u_{k-1,j}^h} + \frac{\partial \mathcal{L}^h \left\langle \underline{u}^h \right\rangle_{i,j}}{\partial u_{k,j+1}^h} + \frac{\partial \mathcal{L}^h \left\langle \underline{u}^h \right\rangle_{i,j}}{\partial u_{k,j-1}^h} \right) \end{aligned} \tag{2.43}$$

$$\begin{aligned} \overline{u}_{i,j}^h = {} & \tilde{u}_{i,j}^h + \omega_{JA} \left(\delta_{i,j}^h - \frac{1}{4} \left(\delta_{i+1,j}^h + \right.\right. \\ & \left.\left. \delta_{i-1,j}^h + \delta_{i,j+1}^h + \delta_{i,j-1}^h \right) \right) \end{aligned} \tag{2.44}$$

2.6.3 Transient calculation implementation

Transient calculations face some specific numerical difficulties. The direct $SU2$ discretising of the transient term in finite differences leads to numerical damping, see Wijnant [127], Venner and Lubrecht [110], Venner and Morales-Espejel [114] and Venner et al. [114]. A more sophisticated $NU2$ scheme is used. A detailed implementation of the Gauss-Seidel and the Jacobi line relaxation is given using the $NU2$ scheme in appendix A.

2.6.4 Numerical accuracy

Some results about the numerical accuracy are presented below. The evolution of numerical errors as a function of the number of points is studied. Several curves represent the error in the pressure calculation, the stress calculation and the stress risk integral calculation.

When an indent crosses a contact, it creates a pressure perturbation (positive over the shoulders and negative in the hole). The additional pressure amplitudes are defined in figure 2.9 for a centered indent. For dry contacts, this pressure distribution is axysymmetric, this is no longer true for EHL contacts.

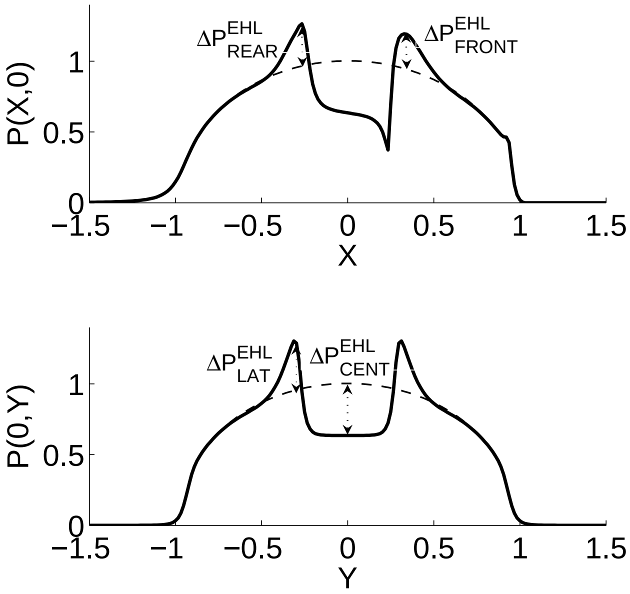

Figure 2.9: Additional pressure amplitude definition

Dry contact

The domain is $[-2\ 2] \times [-2\ 2]$. Figure 2.10 shows that the error in the additional pressure amplitude for $\Phi = 0.25$ is roughly twice the error for $\Phi = 0.5$. A minimum of 16 points per diameter is required to ensure an accuracy of 1% on the additional pressure amplitude. A similar conclusion was obtained by Coulon [24].

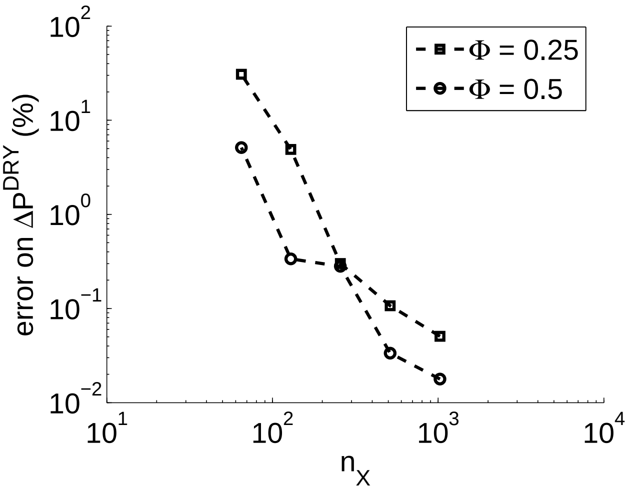

Figure 2.10: Error in ΔP^{DRY} for a dry contact as a function of n_X. Indent geometry $\Phi = 0.25\ 0.5$, $D/\Phi = 2$, $K = 4$

EHL contact

EHL indented contact calculations are transient. A steady-state problem with a longitudinal groove is first used, see equation 2.45 and figures 2.11, 2.12. Then, the error in the full transient problem is presented in figures 2.13, 2.14. The domain is $[-2.5\ 1.5] \times [-2\ 2]$.

These plots show that a finer discretisation for the EHL problem is needed. The error in the solution depends also on the operating conditions. The transient problem requires a minimum of 256 points to ensure an accuracy better than 10% on the additional pressure amplitude and often enables an accuracy close to 2% for $\Phi = 0.5$ and $4 - 5\%$ for $\Phi = 0.25$. A similar conclusion for harmonic wavelength was published by Lubrecht and Venner [86]. During the convergence process, an additional convergence condition has been used. Usually, a condition on the mean residual is used. However, some locally large errors appeared close to the indent. A specific condition on this maximum residual was added.

$$\bar{\mathcal{R}} = -De^{-K\dfrac{Y^2}{\Phi^2}} \cos\left(\frac{\pi Y}{\Phi}\right) \tag{2.45}$$

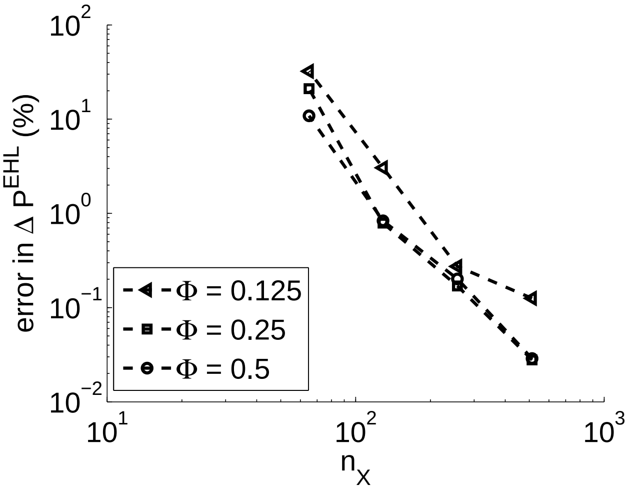

Figure 2.11: Error in ΔP_{LAT}^{EHL} for a stationary EHL contact $M = 200$, $L = 19$ as a function of n_X. Groove geometry $\Phi =$ 0.125 0.25 0.5, $D/\Phi = 1/4$, $K = 4$

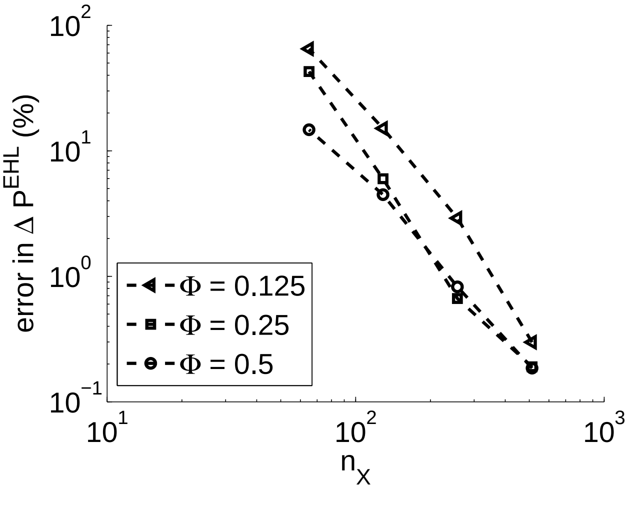

Figure 2.12: Error in ΔP_{LAT}^{EHL} for a stationary EHL contact $M = 800$, $L = 8$ as a function of n_X. Groove geometry $\Phi = 0.125$ 0.25 0.5, $D/\Phi = 1/4$, $K = 4$

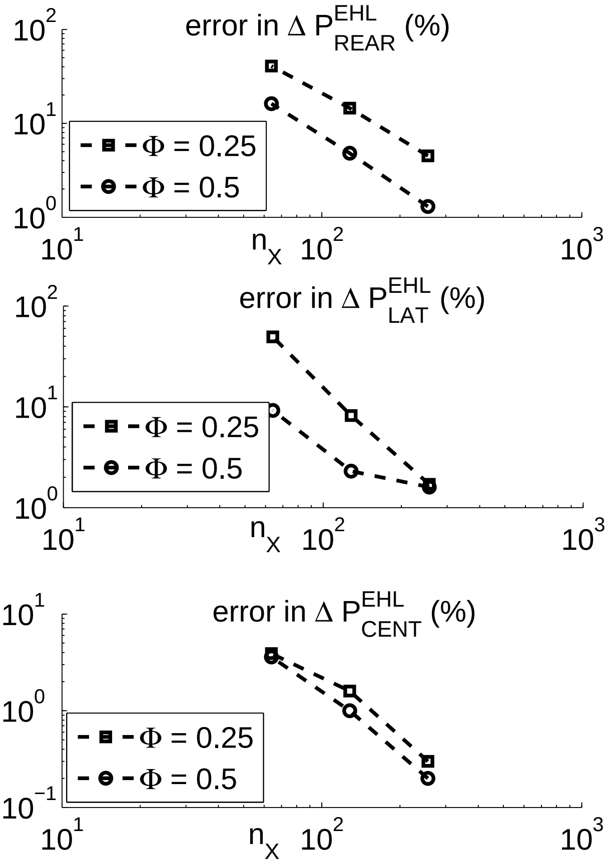

Figure 2.13: Error in ΔP^{EHL}_{REAR} ΔP^{EHL}_{LAT} ΔP^{EHL}_{CENT} for a transient EHL contact $M = 200$, $L = 19$ as a function of n_X. Indent geometry $\Phi = 0.25$ 0.5, $D/\Phi = 1$, $K = 4$

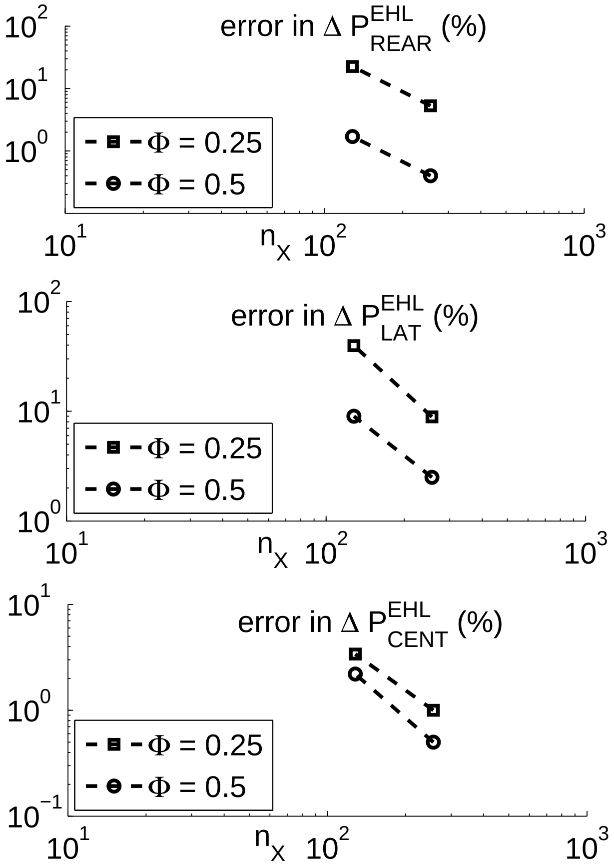

Figure 2.14: Error in ΔP^{EHL}_{REAR} ΔP^{EHL}_{LAT} ΔP^{EHL}_{CENT} for a transient EHL contact $M = 800$, $L = 8$ as a function of n_X. Indent geometry $\Phi = 0.25$ 0.5, $D/\Phi = 1$, $K = 4$

Subsurface stress calculation

Pressure perturbations induce stress perturbations. High stress zones appear close to the surface as shown in figure 2.15. The error in the maximum stress is presented in figure 2.16. Figure 2.17 represents the evolution of the error in the stress risk integral[3] I_D with a constant mesh size in the subsurface. A 256×256 top grid is required to ensure a sufficient accuracy of 1% on the maximum stress and the stress risk integral.

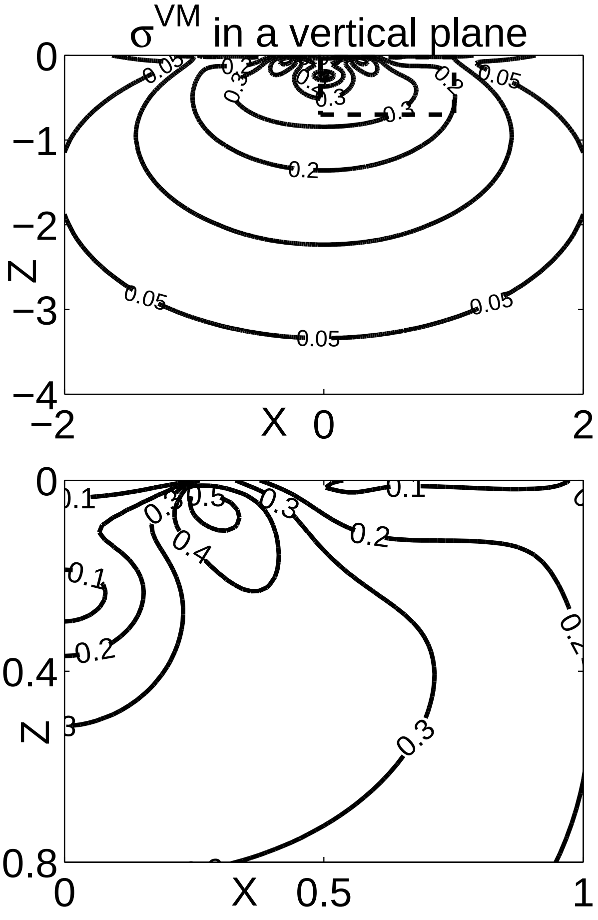

Figure 2.15: Example of a stress distribution in a vertical plane for a dry contact with a centered indent

---

[3] The stress risk integral definition will be detailed in chapter 4.

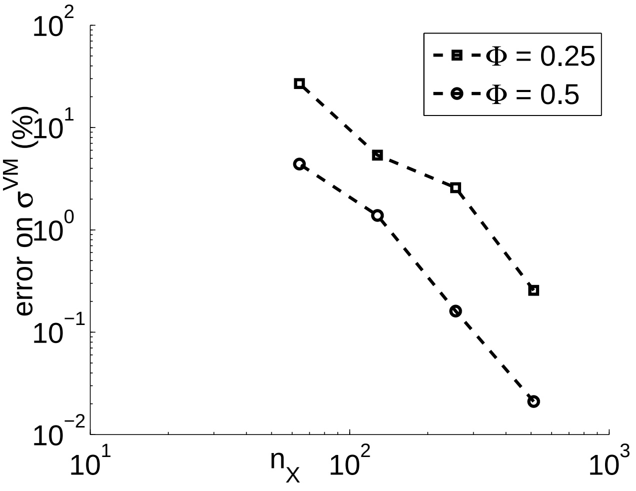

Figure 2.16: Error in σ_{max}^{VM} for a dry contact as a function of n_X. Indent geometry $\Phi = 0.25$ 0.5, $D/\Phi = 2$, $K = 4$

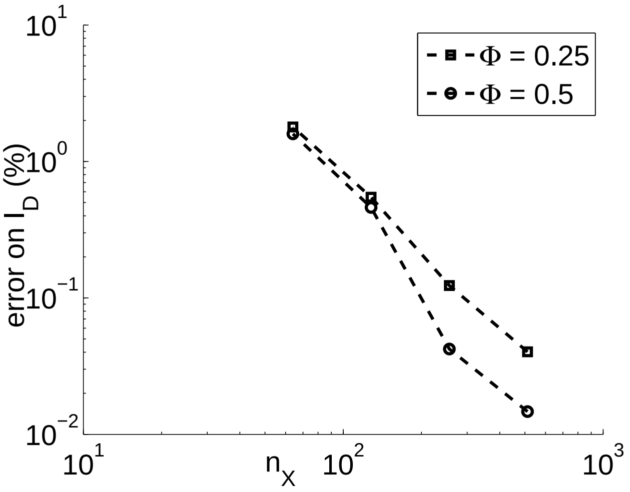

Figure 2.17: Error in I_D for a dry contact as a function of n_X. Indent geometry $\Phi = 0.25$ 0.5, $D/\Phi = 2$, $K = 4$

2.7 Conclusion

This chapter has presented the models and the main assumptions for the contact pressure and stress distribution calculation. Both the dry and the EHL models have been exposed. These two approaches will be used in this work. The simplifications have been emphasized. These simplifications are often due to calculation time constraints and are the result of a compromise in the model. Classical transient Newtonian Reynolds assumptions are used. Pure-rolling conditions are assumed. Only pure elastic deformations are considered. The indent geometry is approximated by an analytical function.

A brief overview of the numerical solution techniques is given. Multigrid techniques are used for the deformation/stress integral calculations and for pressure calculation. The implementation details for the transient EHL solver has been given. Finally, a rapid overview of the numerical accuracy is presented.

Chapter 3

Dry and EHL pressure in indented contacts

3.1 Introduction

The prediction of the indented contact pressure is an intermediate step in the life prediction. The pressure distribution in dry and lubricated contacts is interesting for several reasons. First, it is intuitively directly linked with the contact severity. Second, the theoretical model is well established and film thickness predictions are correlated by experimental observations. Finally, the understanding of the lubrication influence is more direct concerning pressure than stress or even risk integrals.

In this section, the indent geometry and the operating condition influence are studied. The aim is to analyze the influence of different parameters (indent diameter, indent depth, shoulder geometry, contact ellipticity, speed, viscosity, load...) over a certain range of operating conditions. It represents hundreds of calculations which means hundreds of computing days. It also tries to give a physical interpretation of the influence of these parameters.

Some results are presented using a reference pressure P_{REF}. This reference is used for reasons of confidentiality and has no physical meaning. It has a constant value and does not affect the different conclusions. The main interest of these results is in the relative influence of the different parameters and in the physical interpretations rather than the numerical values of pressure.

This chapter is divided in two main sections. First, dry contact assumptions are used. Then, lubricated contacts are studied. Each of these two sections addresses three points: How does pressure evolve when an indent traverses the contact? What is the influence of the contact ellipticity? And finally, what are the important parameters concerning indented contact pressure and how can one predict the pressure perturbations induced by an indent?

3.2 Dry contact pressure

The dry contact is used as a first approximation of the lubricated case. It is seen as an asymptotic case of an EHL contact for low speed and viscosity and high load. There are also some practical advantages: the calculation is rapid, stable and quasi static (the pressure distribution for an indent position does not depend on previous solutions). The interpretation is easier and it provides a reference for the future study of the lubrication influence.

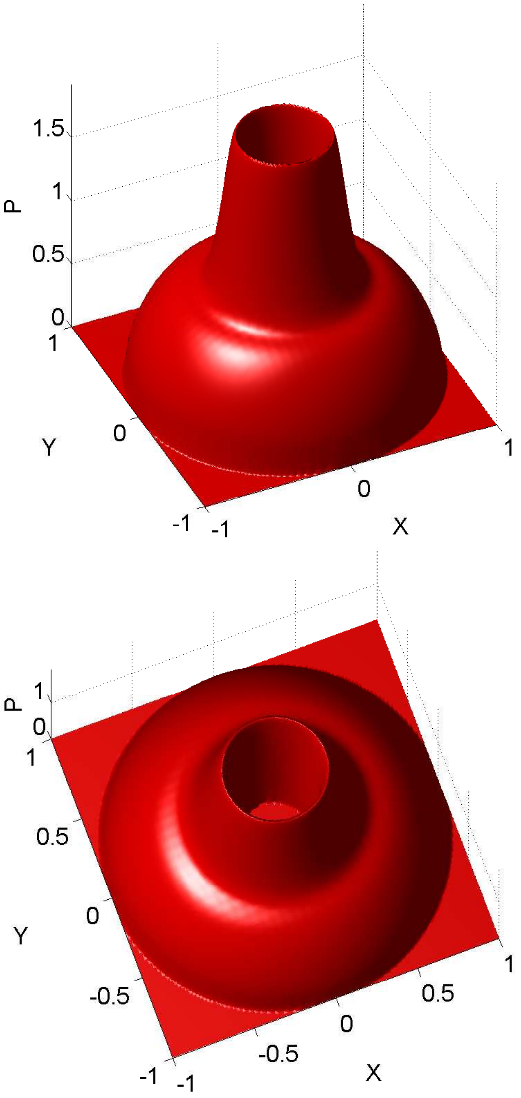

Figure 3.1: 2D pressure distribution in an indented dry contact $\Phi = 0.5$, $K = 4$

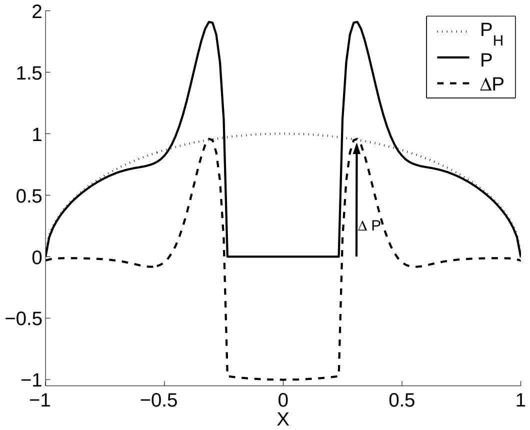

Figure 3.2: Additional pressure amplitude definition for dry contacts $\Phi = 0.5$, $K = 4$

3.2.1 Indent crossing

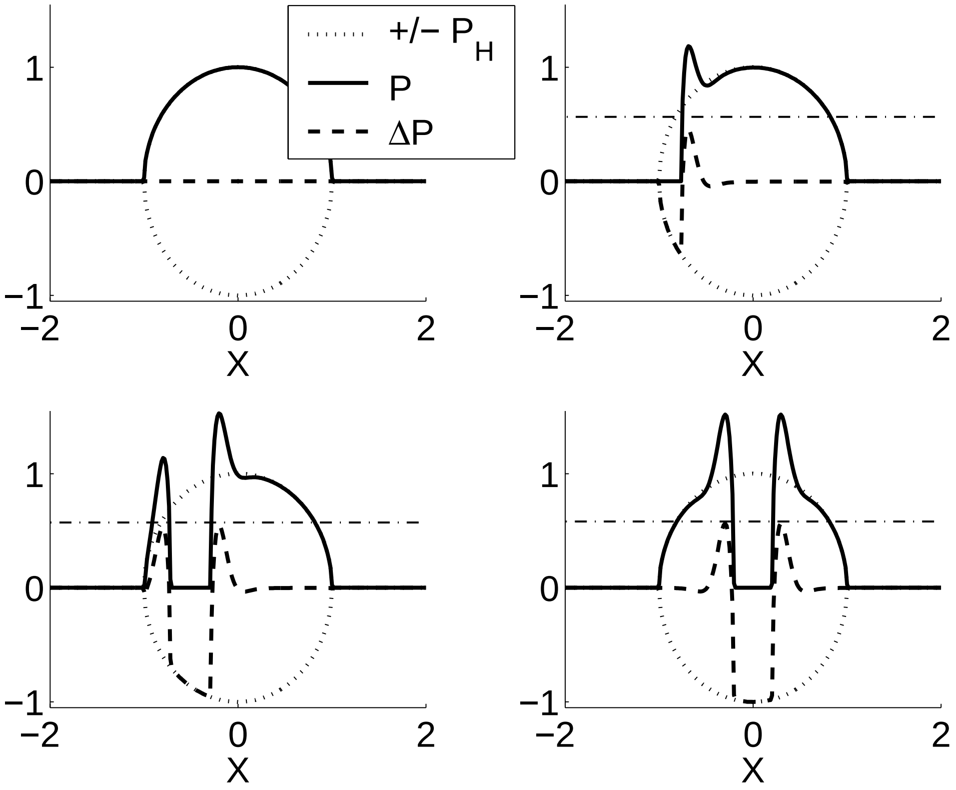

Figure 3.3: Indent traversing a dry contact $\Phi = 0.5$

	$\frac{D}{\Phi} = 1$	$\frac{D}{\Phi} = 2$
$\Phi = 0.5$	$< \mathbf{1\%}$	$< \mathbf{1\%}$
$\Phi = 1$	$< \mathbf{1\%}$	**2%**

Table 3.1: Difference in the additional pressure amplitude during indent crossing for dry contacts $= \left| \Delta P^{DRY}_{X_D=0} - \Delta P^{DRY}_{max(T)} \right| / \Delta P^{DRY}_{max(T)}$ as a function of the indent diameter Φ and the indent slope D/Φ for $K = 4$

When an indent traverses a contact, it is deformed. A pressure distribution is associated with this deformation. Figure 3.1 represents a 2D pressure distribution in an indented contact. Figure 3.2 represents the pressure distribution and the additional pressure distribution along the rolling direction X of an indented dry contact. Figure 3.3 represents the pressure distribution along the rolling direction at different indent locations: from a smooth contact to a centered indent. If the pressure is divided into the smooth pressure and the additional pressure distribution, one can observe that the additional pressure is almost constant for an indent traversing the contact. The additional pressure is only shifted in the contact along the rolling direction. One could have foreseen this result. It is convenient for several reasons. All the information about the additional pressure distribution during the entire crossing is obtained from a single centered indent calculation, and the additional pressure amplitude for a centered indent is representative of the entire crossing. It saves calculation time and memory because only one position is required.

This is true only for sufficiently small indents. It is quite obvious that if the indent is larger than the contact itself, it would be difficult to measure pressure over the shoulders outside the contact. More reasonably, the indent should be sufficiently small to not perturb the force balance too much. Table 3.1 presents the error in the maximum additional pressure amplitude during the indent crossing. For example, one can read that for a diameter $\Phi = 1$ and an indent slope $D/\Phi = 2$, the approximation error between the additional pressure amplitude for a centered position and the maximum value during the indent crossing is 2%.

3.2.2 Ellipticity

The equations presented in chapter 2 are solved using dimensionless parameters. These dimensionless parameters are especially useful because they allow the complexity of the problem to be reduced. For example for a smooth circular dry contact, the dimensionless equations enable one to obtain a unique solution which is applicable to every smooth circular dry contact regardless[1] of the radius of curvature, load, Hertzian pressure, contact half width… The smooth circular dry contact pressure distribution is calculated once for all. Moreover, it demonstrates the level of understanding of the problem which is reduced to its minimum expression.

The classical Hertzian dimensionless parameters are used. It means that parameters describing indents depend on the contact conditions. For example a given “physical” indent will not have the same dimensionless depth and diameter if the contact half width changes.

$$
\begin{aligned}
P &= \frac{p}{p_H} \\
H &= \frac{h\,R_x}{b^2} \\
X &= \frac{x}{b} \\
Y &= \frac{y}{b}
\end{aligned}
$$

Elliptical contacts are commonly encountered in rolling element bearings. The ellipticity can vary substantially. A simple question[2] appears: when varying the ellipticity, how do the pressure perturbations induced by a given indent evolve? Actually, it depends on how one varies the ellipticity κ. There are three free parameters in the dry elliptical smooth contact. Several arbitrary choices can be made; only one is presented here. The ellipticity variation will be obtained with the contact half width b along the minor axis (rolling direction X) and the Hertzian pressure p_H remaining unchanged.

Several reasons justify this choice: First, the ratio between the harmonic roughness wavelength and the contact half width b was identified by several authors as a key parameter for the deformation in lubricated contacts, see section 2.3. As the dry contact study is the basis of the lubrication study, the choice which was expected to simplify the lubrication study was made. Moreover, it maintains the dimensionless indent diameter constant when varying the ellipticity κ. Finally, the Hertzian pressure p_H appeared intuitively to be an important parameter. A constant Hertzian pressure when varying the ellipticity simplifies the comparison of the dimensionless pressures[3].

The consequence is that the radius of curvature along the rolling direction R_x is imposed and varies with the ellipticity κ. Equation 3.1 is obtained from Hertzian equations; the left handside is constant when varying the ellipticity.

---

[1] Actually, there are only two independent variables.

[2] Because a simple question does not systematically give rise to a *simple* answer.

[3] Certainly, they are made dimensionless with the *same* Hertzian pressure

$$\frac{bE'}{\pi p_H} = \frac{4}{\pi} \frac{\mathcal{E}}{1 + \dfrac{R_x}{R_y}} R_x \tag{3.1}$$

The above equation is used in equation 2.4. For the two asymptotic cases of a circular and an infinitely long contact, one obtains:

$$\begin{aligned} \text{circular contact:} \quad & \frac{bE'}{\pi p_H} = R_x \\ \text{line contact:} \quad & \frac{bE'}{\pi p_H} = \frac{4}{\pi} R_x \end{aligned}$$

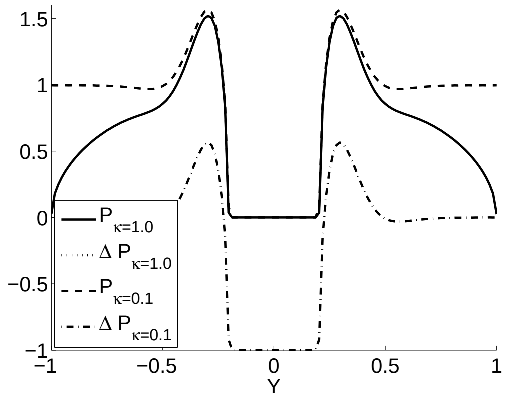

Figure 3.4: Dry contact pressure distribution around an indent as a function of the ellipticity $\Phi = 0.5$

The result is that the additional pressure distribution remains almost constant when varying the ellipticity. An example of the pressure distribution around an indent when varying the ellipticity is given in figure 3.4, the additional pressure distribution are perfectly superimposed. This is true up to a certain indent size. The force balance should not be perturbed significantly. Table 3.2 gives an idea of the validity of this observation. For example, one can see that the difference between the additional pressure amplitude for $\kappa = 1$ and $\kappa = 0.1$ for an indent with diameter $\Phi = 1$ and indent slope $D/\Phi = 1$ is 3%.

For sufficiently small indents, the ellipticity does not change the additional pressure amplitude. This is interesting for two reasons: First, it eliminates on one parameter of the parametric study. There is no need to calculate all the different indent geometry pressures for several ellipticities. Second, wide elliptical calculations are time and memory consuming because the number of unknowns is proportional to $1/\kappa$.

	$\frac{D}{\Phi} = 1$	$\frac{D}{\Phi} = 2$
$\Phi = 0.5$	$< \mathbf{1\%}$	$< \mathbf{1\%}$
$\Phi = 1.0$	**3%**	**7%**

Table 3.2: Difference in the additional pressure amplitude for two ellipticities $\kappa = 1.0$ and $\kappa = 0.1$ for dry contacts $= \left|\Delta P^{DRY}_{\kappa=1.0} - \Delta P^{DRY}_{\kappa=0.1}\right| / \Delta P^{DRY}_{\kappa=1.00}$ as a function of the indent diameter Φ and the indent slope D/Φ for $K = 4$

3.2.3 Analytical model for dry contacts

The previous section shows that the indent location question and the ellipticity variation question can be sidestepped. The next point is to highlight the important parameters: the indent slope D/Φ and the shoulder geometry K, and to propose a predictive model for the pressure perturbations.

The analytical model developed below is based on the model developed by Coulon [24], Coulon et al. [25, 26] and Gupta et al. [46]. This model is based on the elastic deformation of harmonic waviness studied by Johnson [67]. Coulon classified the indent in three categories: Zone A, indents are completely flattened in the contact; Zone B, the pressure becomes zero in the indent hole and indents are no longer entirely flattened; Zone C, the load is entirely carried by the shoulders. Coulon proposed an analytical model for the additional pressure amplitude in zone A and C. This model is extended to account for the shoulder influence in zone A and for the zero pressure in zone B, see figure 3.5.

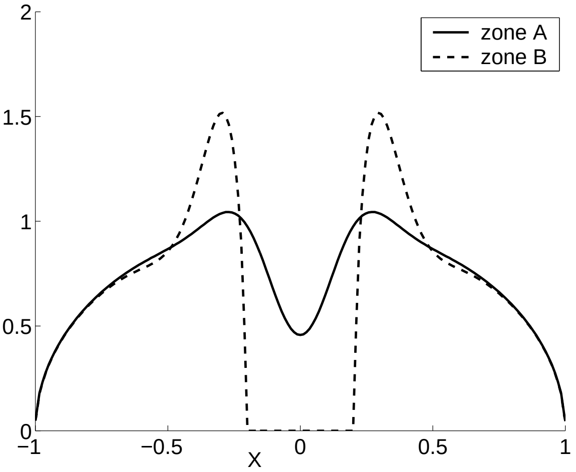

Figure 3.5: Zone A - B typical pressure distribution

Johnson shows that the additional pressure amplitude associated with the complete deformation of a harmonic waviness is proportional to the slope. The same observation was made by Coulon, concerning indents in zone A. The additional pressure amplitude in zone A is linear in the indent slope D/Φ. The main assumption for the zone A model was that the load not carried by the hole because of the lack of material is totally compensated by an annular additional pressure distribution referred to as the "not carried load", see figure 3.6.

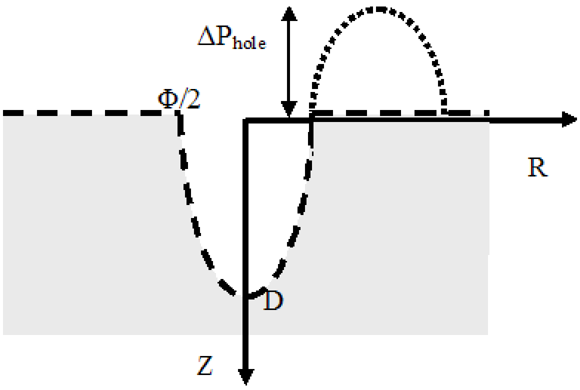

Figure 3.6: Analytical model pressure distribution

However, analysis of the additional pressure shows that the additional pressure amplitude ΔP depends on the shoulder geometry (controlled by K). Moreover, the "not carried load" is only partially compensated by the annular additional pressure. The load carried by the annular additional pressure around the hole represents roughly 60% of the "not carried load". The remaining load is spread over the entire contact area. Finally, the model can be extended to account for the partially flattened indents of zone B.

Table 3.3 presents the additional pressure amplitude evolution as a function of the indent slope D/Φ, the shoulder geometry K and the indent diameter Φ. For example, an indent slope of 0.5, a shoulder parameter $K = 3$ and an indent diameter $\Phi = 0.25$ lead to an additional pressure amplitude $\Delta P/P_{REF}$ of 1.82. For this case, when varying the indent diameter Φ from 0.25 up to 1.0, the additional pressure amplitude varies between 1.82 and 1.72. Two conclusions can be drawn: first, the indent slope D/Φ and the shoulder geometry K have an important influence on the additional pressure amplitude ; second, the indent diameter Φ has a limited impact.

Extension of the zone A model

The aim is to include the shoulder influence in the analytical zone A model. Several simplifications are made, the geometry of the hole and the shoulders is approximated. The contribution of the pressure needed to flatten the shoulders is modeled separately of the pressure needed to flatten the

		$\frac{D}{\Phi} = 0.5$	$\frac{D}{\Phi} = 1$	$\frac{D}{\Phi} = 2$
$K = 3$	$\Phi = 0.25$	**1.82**	**3.27**	**5.83**
	$\Phi = 0.50$	**1.82**	**3.25**	**5.78**
	$\Phi = 1.00$	**1.72**	**2.96**	**4.83**
$K = 4$	$\Phi = 0.25$	**1.59**	**2.83**	**4.82**
	$\Phi = 0.50$	**1.59**	**2.82**	**4.80**
	$\Phi = 1.00$	**1.58**	**2.72**	**4.41**
$K = 8$	$\Phi = 0.25$	**1.26**	**2.05**	**3.10**
	$\Phi = 0.50$	**1.26**	**2.05**	**3.10**
	$\Phi = 1.00$	**1.30**	**2.09**	**3.16**

Table 3.3: Evolution of the dry contact additional pressure amplitude $\Delta P^{DRY}/P_{REF}$ as a function of the indent slope D/Φ, the shoulder geometry K and the indent diameter Φ

hole. The global additional pressure over the dent shoulder is divided in two contributions:

$$\Delta P_{tot} = \Delta P_{hole} + \Delta P_{shoulder} \tag{3.2}$$

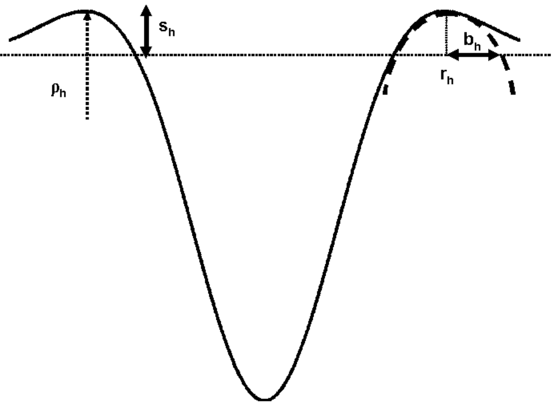

Figure 3.7: Shoulder approximation

The analytical approach of the shoulder influence uses a parabolic approximation of the shoulder geometry, see figure 3.7. The shoulder radius of curvature and the shoulder height are used for the parabolic approximation. These two parameters are functions of D, Φ and K. The analytical additional pressure amplitude is proportional to the indent slope with respect to a coefficient ν which is a function of the attenuation factor K, see equation 3.3. A "circular" line contact of length $2\pi r_h$ is assumed. Concerning the hole, the factor ζ in equation 3.4 is a function of K only, it depends also on the simplified geometry used.

$$\Delta P'_{shoulder} \propto \frac{D}{\Phi}\nu(K) \tag{3.3}$$

$$\Delta P'_{hole} \propto \frac{D}{\Phi}\zeta(K) \tag{3.4}$$

Details about the calculation of ν and ζ are given in appendix B. Several possibilities have been tried to approximate the shoulder and hole geometry. However, they only lead to modify the proportionality coefficient in equations 3.3 and 3.4. Two coefficients n and m are used to adjust the analytical model to numerical results of zone A in equation 3.5.

Figure 3.8 represents the ratio between the additional pressure amplitude and the indent slope as a function of the indent slope in zone A. Different shoulder geometries are presented from $K = 3$ corresponding to high shoulders to $K = 8$ corresponding to flat shoulders. The model in dashed lines correctly matches the full numerical results.

$$\Delta P_{tot} = n\Delta P'_{hole} + \ m\Delta P'_{shoulder} \tag{3.5}$$

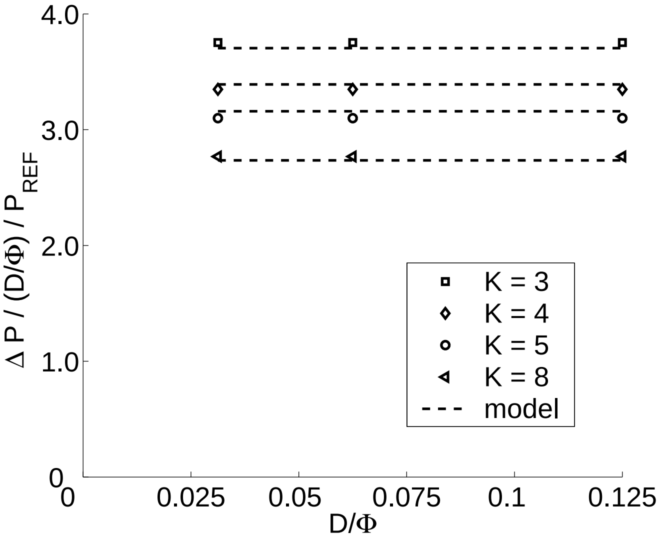

Figure 3.8: Ratio between the additional pressure amplitude and the indent slope $\frac{\Delta P}{D/\Phi}$ in zone A (completely flattened indents) as a function of the indent slope D/Φ and the decay coefficient K

Zone B model

Zone B corresponds to partially flattened indents. When the indent is sufficiently deep, it is not entirely flattened and a non contact zone remains in the indent center where the pressure is zero. Figure 3.9 represents a typical initial and deformed indent geometry in zone B. The direct extension of the zone A model to zone B decreases progressively the hole contribution when the hole geometry is less and less flattened. The main idea of the zone A model is to compensate the "not carried load". If the hole is no longer completely flattened, the "not carried load" decreases. Keeping a sufficient hole deformation, it is expected that the shoulder influence remains constant. So, the transition from zone A to zone B is seen as a modulation of the hole additional pressure contribution.

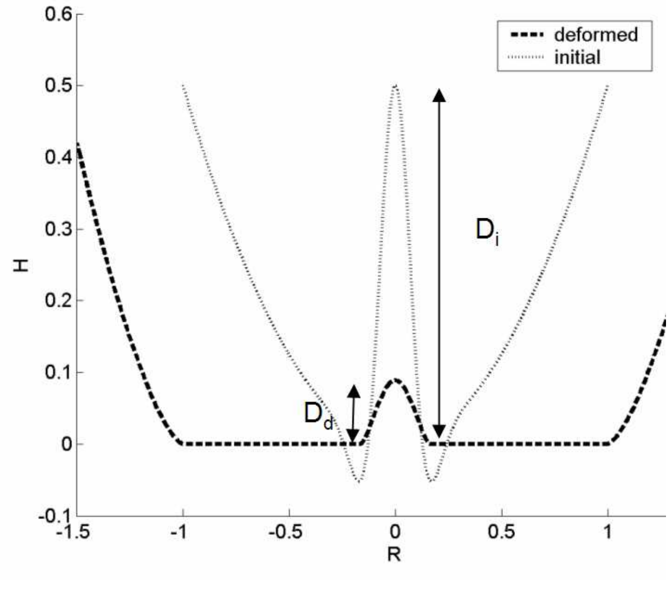

Figure 3.9: Example of deformed indent geometry in zone B (partially flattened indent)

A study of the ratio between deformed and initial indent depth D_d/D_i shows that it depends only on the indent slope, see figure 3.10. Two steps are needed: first, linking the remaining hole depth with the indent slope; second adjusting the modulation of the hole additional pressure (coefficient s and σ in equation 3.6). More details can be found in appendix B. The additional pressure reads:

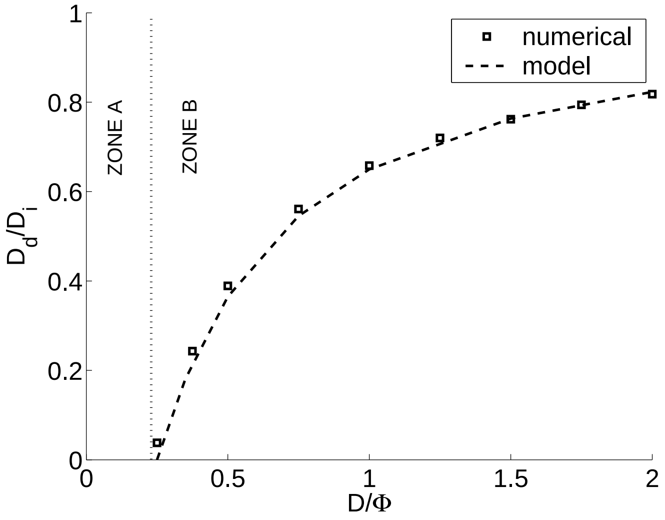

Figure 3.10: Ratio between deformed and initial indent depth D_d/D_i as a function of the indent slope D/Φ

$$
\begin{aligned}
F &= D_d/D_i \\
\Delta P_{tot} &= n\frac{D}{\Phi}\zeta(K)\left(1 - s\,F^{\omega}\right) + m\frac{D}{\Phi}\,\nu(K)
\end{aligned}
\tag{3.6}
$$

Figure 3.11 represents the ratio between the additional pressure amplitude and the indent slope as a function of the indent slope in zone B. A good correlation is obtained between the numerical results and the analytical predictions (dashed lines). The difference increases with increasing slope. Indeed, with a remaining hole depth exceeding 80% of the indent depth, the model is less accurate. Figure 3.12 recaps the good correlation obtained between the full numerical calculations and the analytical model.

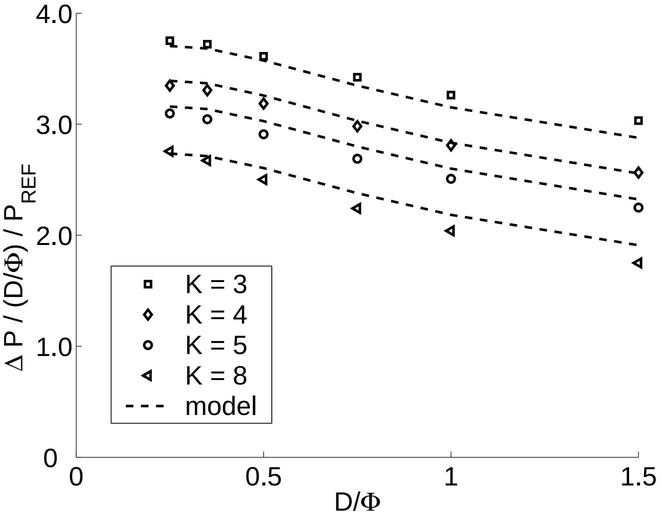

Figure 3.11: Ratio between the additional pressure amplitude and the indent slope $\frac{\Delta P}{D/\Phi}$ in zone B (partially flattened indent) as a function of the indent slope D/Φ and the decay coefficient K

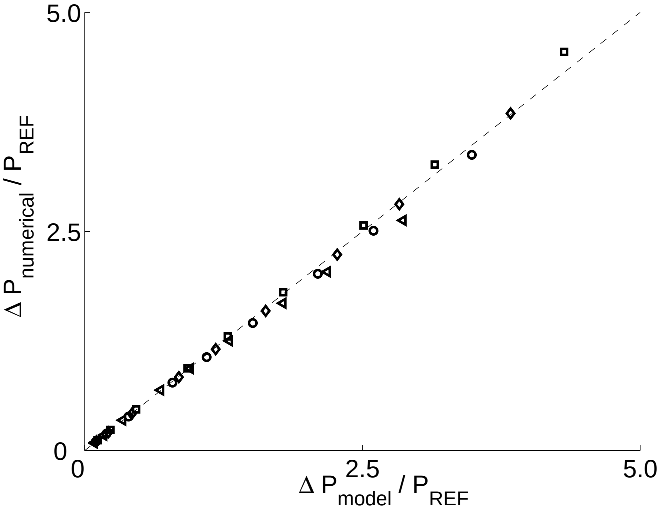

Figure 3.12: Full numerical additional pressure versus analytical prediction for $\Phi = 0.25 - 0.5$, $D/\Phi = 0 - 2$ and $K = 3 - 8$

3.3 EHL contact pressure

The previous section studied the dry indented contact pressure. Below, the lubricated study is proposed.

Lubrecht et al. [83] presented a numerical work on the indented rolling bearing life. The contact was modeled by an EHL 1D line contact and the indent by a transverse groove. The groove was chosen without any sharp corners and with significant shoulders emulating real indents. The parametric study of the life prediction focused on the Hertzian pressure, the relative size of the indent related to the contact size, and the indent slope. The dry contact assumption was said to approximate closely the pure-rolling lubricated contacts. 2D point contacts were studied by Lubrecht et al. [85] and the authors concluded that previous studies using 1D geometries were not able to reproduce accurately 2D results. Ai and Cheng [1] studied rolling sliding indented point contacts and highlighted the induced dent phenomenon described in section 3.3.4.

Figure 3.13 represents the pressure distribution in a pure-rolling EHL indented contact. The indent is centered. The additional pressure amplitudes are defined. The pressure distribution is more complex than in dry contacts. It is no longer symmetric and a plateau appears in the indent hole whereas a dry contact calculation would have given a zero pressure in the indent hole.

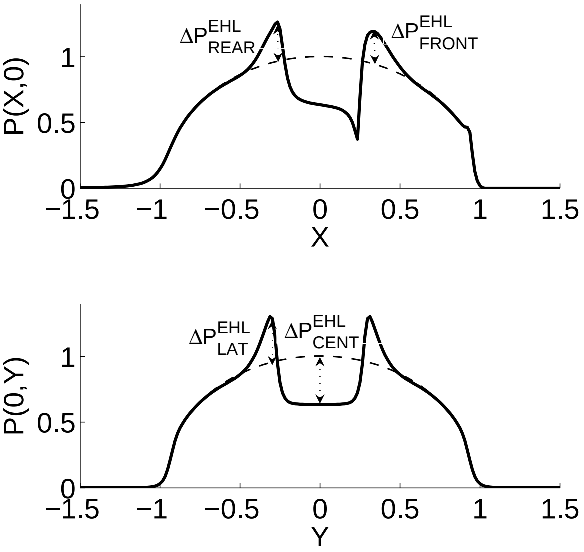

Figure 3.13: Additional pressure amplitude definition for EHL contacts $\Phi = 0.5$, $M = 400$, $L = 5$

3.3.1 Indent crossing

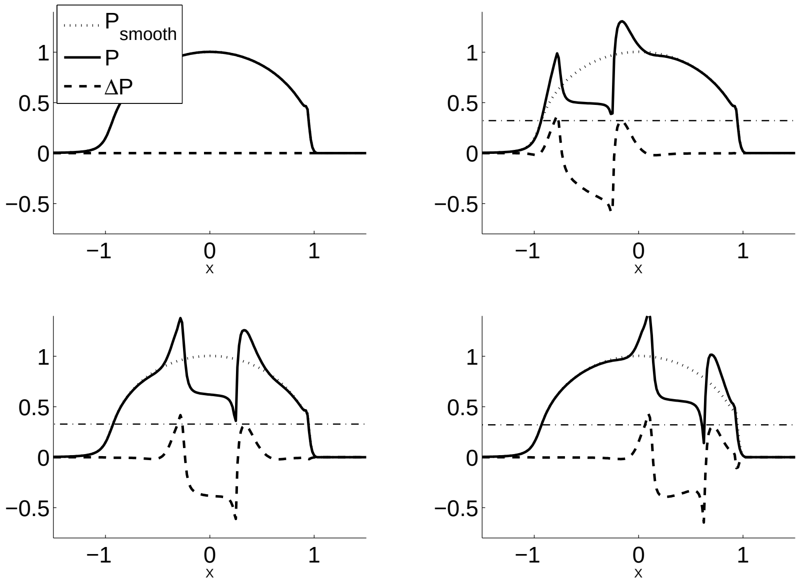

Figure 3.14: Indent traversing an EHL contact $M = 400$, $L = 5$

Similar results as for dry contacts in section 3.2.1 have been obtained for EHL pure-rolling contacts. Figure 3.14 shows that the additional pressure distribution remains almost constant when an indent traverses the contact. For pure-rolling conditions, the geometrical deformation in EHL contacts has been studied by several authors especially for harmonic waviness. The transition between the low and high pressure region is associated with an important increase in the lubricant viscosity. The fluid becomes so viscous that its geometry is "frozen". The lubricant separating the two surfaces (indent, roughness…) can no longer be deformed, it traverses the contact without any change in shape. For pure-rolling conditions, the lubricant traverses the contact at the same velocity as the surfaces. That explains why the additional pressure is almost constant.

Table 3.4 gives the error of the additional pressure amplitude over the rear shoulder when approximating the maximum additional pressure amplitude during indent crossing by the centered position value. For example, one can see in table 3.4 that the error in the additional pressure amplitude over the rear shoulder between a centered indent position and the real maximum for an indent diameter $\Phi = 0.5$ and an indent slope $D/\Phi = 0.5$ is equal to 2%.

Similar conclusions as in the dry contact study are obtained. However,

	$\frac{D}{\Phi} = 0.5$	$\frac{D}{\Phi} = 1$
$\Phi = 0.5$	**2%**	**4%**
$\Phi = 1$	**3%**	**6%**

Table 3.4: Difference in the additional pressure amplitude over the rear shoulder during indent crossing for EHL contacts = $\left|\Delta P^{EHL}_{X_D=0} - \Delta P^{EHL}_{max(T)}\right| / \Delta P^{EHL}_{max(T)}$ as a function of the indent diameter Φ and the indent slope D/Φ for $K = 4$, $M = 400$, $L = 5$

two differences exist: calculations are still transient even if one considers only the centered indent position and it is correct only for Newtonian pure-rolling conditions neglecting the outlet pressure spike.

3.3.2 Ellipticity

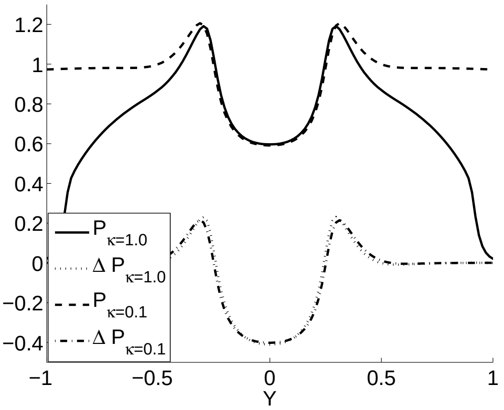

Figure 3.15: Pressure distribution around an indent when varying the ellipticity in an EHL contact, $\Phi = 0.5$, $M = 400$, $L = 10$

For EHL contacts, the ellipticity variation is made in accordance with the dry contact study. The radius of curvature is changed according to the ellipticity. As for dry contacts, this change appears in the equation 2.4, but also in the equation 2.15.

		$\frac{D}{\Phi} = 0.5$	$\frac{D}{\Phi} = 1$
$M = 200$ $L = 6.3$	$\Phi = 0.50$	$<$ **1%**	**2%**
	$\Phi = 1.00$	$<$ **1%**	**4%**
$M = 400$ $L = 10$	$\Phi = 0.50$	**1%**	**3%**
	$\Phi = 1.00$	$<$ **1%**	**2%**

Table 3.5: Difference in the additional pressure amplitude over the rear shoulder for two ellipticities $\kappa = 1.0$ and $\kappa = 0.2$ for EHL contacts $= \left|\Delta P^{EHL}_{\kappa=1.0} - \Delta P^{EHL}_{\kappa=0.2}\right| / \Delta P^{EHL}_{\kappa=1.0}$ as a function of the operating conditions M, L, the indent diameter Φ and the indent slope D/Φ for $K = 4$

Additional pressure distributions in indented contacts are hardly affected by an ellipticity variation. Figure 3.15 gives an example of the pressure distribution around an indent in a circular and an equivalent elliptical contact. Table 3.5 presents some examples of the relative difference between elliptical and circular indented contacts as a function of the indent geometry and the operating conditions. It can be noticed that the difference remains small and is of the same order of magnitude as the discretisation error. For example, for $M = 400$ and $L = 10$, $\Phi = 0.5$ and $D/\Phi = 1.0$, the difference between $\kappa = 1.0$ and $\kappa = 0.2$ is 3%. The ellipticity influence is thus neglected. Hooke and Venner [56] have presented results in accordance with this conclusion. The authors explain that when varying the ellipticity, the modification of the inlet flow leads to a negligible modification of the harmonic waviness deformation.

3.3.3 Pure-rolling EHL pressure prediction

The important parameters of the indented lubricated contact study are presented. The dry contact study and existing lubricated contact deformation theory will be used and extended.

The amplitude reduction theory predicts the deformation of harmonic waviness in EHL contacts. Some differences between the amplitude reduction theory and the indented contact pressure study exist. The amplitude reduction theory studies harmonic waviness of small amplitudes. Typically, the initial waviness amplitude does not exceed 10% of the smooth central film thickness, whereas, indent depth can exceed by a factor of ten or more the film thickness. Under these conditions, the linear relation between deformed and initial amplitude is no longer true. A second difference is the complexity of the 2-D indent geometry. Moreover, the harmonic waviness deformation is studied for a periodic signal. For indents, no "established" regime can be defined because indents are not periodic.

Depending on the operating conditions and the indent geometry, the pressure perturbation amplitude can vary substantially. This work presents an analysis of the parameter influence and shows an approach to predict these pressure perturbation amplitudes. Existing theory for roughness deformation is extended to pure-rolling EHL indented contact pressure perturbations. First, a study of shallow indents is proposed, then sharper indents are studied. Key parameters are presented permitting theoretical predictions.

Figure 3.16 is an example of the additional pressure amplitude over the rear shoulder in an EHL contact as a function of the dry contact value. Different speeds have been represented (all the other parameters remain unchanged). When the speed decreases, M increases and L decreases. Two points are interesting: first, it shows the importance of the operating conditions because the additional pressure amplitude varies substantially with the speed variation; second, for pure-rolling contacts the dry contact is an upper boundary. When decreasing the speed, the EHL additional pressure amplitude approaches the dry contact value.

Shallow indent

For small amplitudes, the harmonic waviness deformation is linear. It justifies the use of the ratio between the deformed and the initial amplitudes. Hooke proposed a dimensionless parameter ∇, representing the ratio between the waviness wavelength and the inlet contact length. This parameter is proportional to $\lambda/b \cdot \sqrt{M/L}$, which corresponds to the parameter resulting from numerical studies conducted by Venner and Lubrecht.

The amplitude reduction curve presents two asymptotes: for small ∇, the roughness is associated with a small deformation (small pressure perturba-

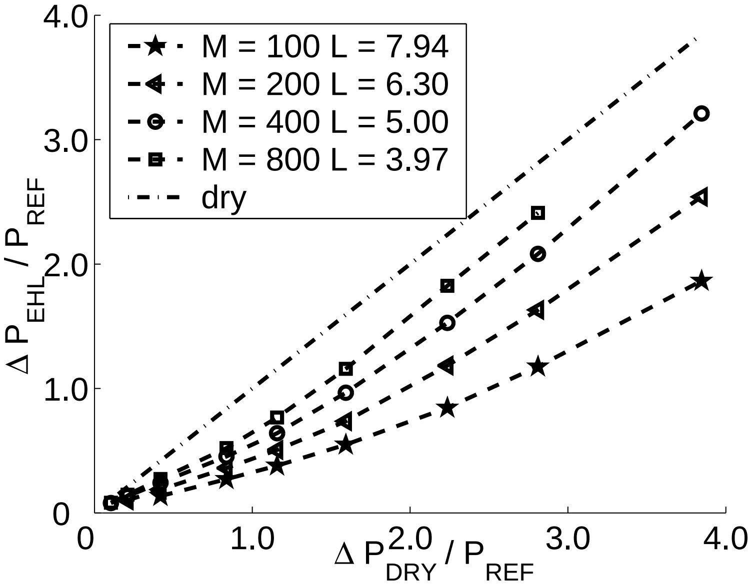

Figure 3.16: Additional pressure amplitude over the rear shoulder in ehl contacts compared to a dry contact when varying the mean speed, $\Phi = 0.5$

tion), and large ∇ corresponds to a completely flattened geometry (pressure perturbation close to the dry contact). So, to account for these asymptotes, the curve fit presented is based on the following functions:

$$\frac{\mathcal{S}\Delta P^{EHL}}{\mathcal{S}\Delta P^{DRY}} \propto 1 - \frac{1}{1 + f(\nabla_\Phi)} \tag{3.7}$$

$$f(0) = 0$$

$$\frac{\mathrm{d}f(\nabla_\Phi)}{\mathrm{d}\nabla_\Phi} > 0 \text{ for } \nabla > 0$$

$$\nabla_\Phi \propto \Phi \sqrt{\frac{M}{L}} \tag{3.8}$$

In the case of indents, the deformed amplitude is difficult to define. The deformed geometry is not harmonic, so the ratio between initial and deformed amplitude is not clearly defined. That is an other reason why the pressure perturbation amplitudes (positive and negative) are used, instead of the deformed amplitudes. For pure-rolling EHL contacts, the dry contact pressure is an upper limit.

The main idea is to assume that, similarly to small waviness deformation, the small indent additional pressure can be described as a function of the operating conditions and the indent diameter (which corresponds to a pseudo wavelength used to define ∇_Φ). As mentioned before, indents can be very deep. In order to use the linearity of small indent pressure variations, the initial slopes $\mathcal{S}\Delta P^{EHL}$ of the curves ΔP^{EHL} as a function of indent slope D/Φ are used. For given operating conditions, if the indent slope tends to zero, it means that the indent depth will become much smaller than the film thickness, given Φ constant.

$$\mathcal{S}\Delta P = \left.\frac{\mathrm{d}\Delta P(D/\Phi)}{\mathrm{d}(D/\Phi)}\right|_{D/\Phi\to 0} \tag{3.9}$$

The indent geometry and the associated transient phenomena are complex. The pressure perturbation amplitudes are not constant around the indent. That is why several sets of curves will be proposed to model the additional pressure amplitudes.

Figures 3.17 and 3.18 recap results (initial slope) of numerous calculations representing a relatively wide range of indent sizes and operating conditions. Every point represents several hours of computing time. A single curve can be clearly observed. The pressure excursion slope ratio $\mathcal{S}\Delta P^{EHL}/\mathcal{S}\Delta P^{DRY}$ increases with the dimensionless indent diameter parameter ∇_Φ[4]. As mentioned above, the two asymptotes of the pressure perturbations also exist: on the one hand, contact conditions yielding small deformations and small pressure perturbations; on the other, the indent is completely flattened and the dry contact pressure amplitude is reached.

---

[4] The numerical value of $\mathcal{S}\Delta P^{DRY}$ is known as a function of K from the dry contact study

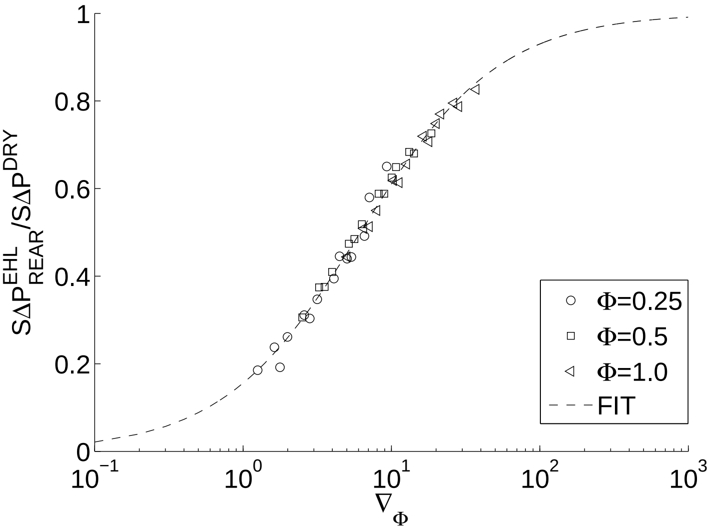

Figure 3.17: Relative initial slope $\mathcal{S}\Delta P^{EHL}_{REAR}/\mathcal{S}\Delta P^{DRY}$ as a function of the dimensionless indent diameter parameter ∇_{Φ}, for $M = 100 \ - \ 1200$, $L = 3 \ - \ 19$, $\Phi = 0.25 \ - \ 1.0$, $K = 3$

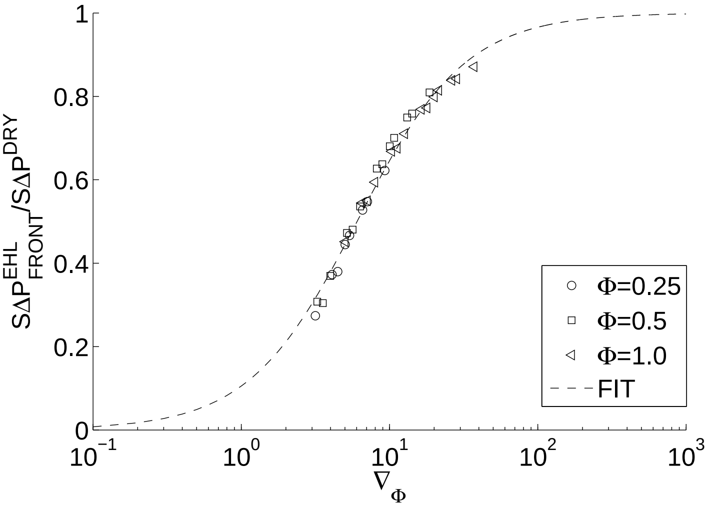

Figure 3.18: Relative initial slope $\mathcal{S}\Delta P^{EHL}_{FRONT}/\mathcal{S}\Delta P^{DRY}$ as a function of the dimensionless indent diameter parameter ∇_{Φ}, for $M = 100 \ - \ 1200$, $L = 3 \ - \ 19$, $\Phi = 0.25 \ - \ 1.0$, $K = 3$

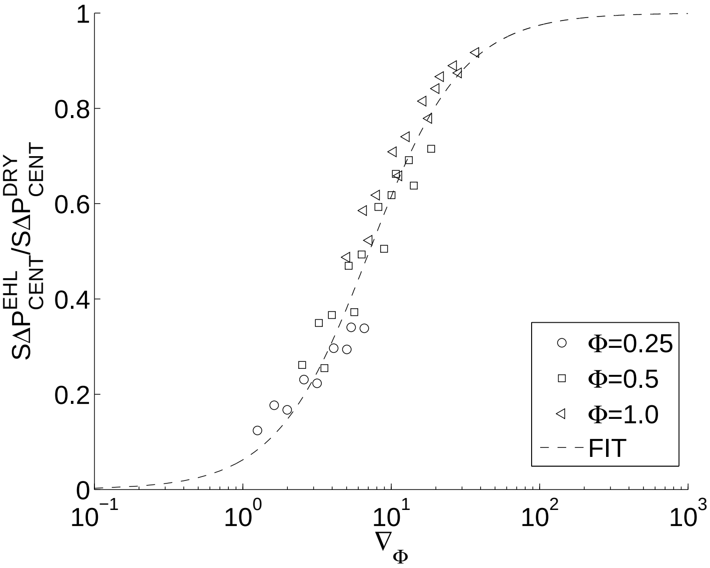

Figure 3.19: Relative initial slope $\mathcal{S}\Delta P^{EHL}_{CENT}/\mathcal{S}\Delta P^{DRY}$ as a function of the dimensionless indent diameter parameter ∇_Φ, for $M = 100 - 1200$, $L = 3 - 19$, $\Phi = 0.25 - 1.0$, $K = 3$

A similar analysis is possible for the negative pressure perturbation. However, as the behavior of the pressure in the indent hole is very nonlinear, results are less satisfying. Nevertheless, several results are interesting. The initial slopes of numerous calculations have been extracted and are represented in figure 3.19.

Figure 3.20 enables one to predict the initial slope of the curves ΔP^{EHL} as a function of D/Φ. It represents in a single plot the three previous equations. This initial slope is a function of the indent diameter and the operating conditions through the parameter ∇_Φ. When ∇_Φ increases, the ratio $\mathcal{S}\Delta P^{EHL}/\mathcal{S}\Delta P^{DRY}$ increases. When this ratio is close to 1, the additional pressure amplitude initial slope is close to the dry contact. The three curves are very similar and no clear difference can be extracted when accounting for the numerical accuracy.

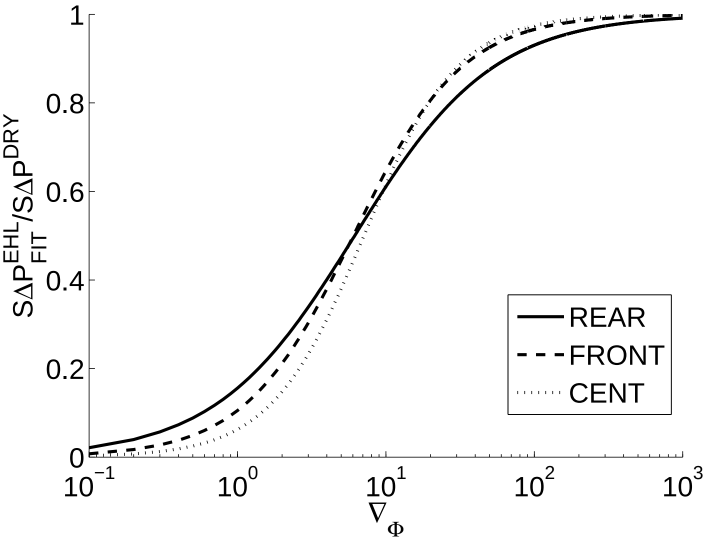

Figure 3.20: Relative initial slope $\mathcal{S}\Delta P^{EHL}/\mathcal{S}\Delta P^{DRY}$ as a function of the dimensionless indent diameter parameter ∇_Φ, for $M = 100 - 1200$, $L = 3 - 19$, $\Phi = 0.25 - 1.0$, $K = 3$

Moreover, the shoulder influence appears in figure 3.21, which compares results obtained previously ($K = 3$) with an indent with very flat shoulders ($K = 8$)[5]. The additional pressure amplitude initial slope is lower when the shoulders are flatter. However the two curves show similar trends and this difference can also be partially associated with the slight hole geometry variation when varying K.

The similarity of the curves in figure 3.21 does not mean that the pressure perturbations will be the same between $K = 3$ and $K = 8$. The curves represent the ratio between $\mathcal{S}\Delta P^{EHL}$ and $\mathcal{S}\Delta P^{DRY}$. Note that $\mathcal{S}\Delta P^{DRY}$ for $K = 3$ and $K = 8$ are very different. Hence, $\mathcal{S}\Delta P^{EHL}$ between $K = 3$ and $K = 8$ is also very different.

---

[5] The intermediate fit curves for $K = 4$ and $K = 5$ are also plotted

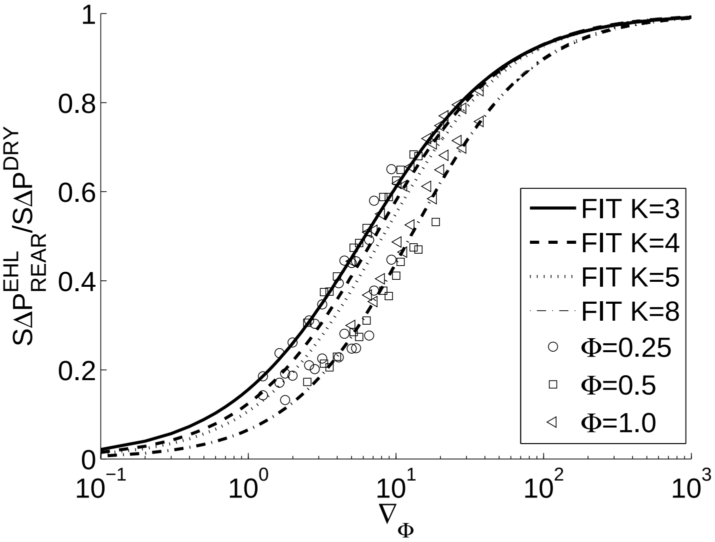

Figure 3.21: Relative slope $\mathcal{S}\Delta P^{EHL}_{REAR}/\mathcal{S}\Delta P^{DRY}$ as a function of the dimensionless indent diameter parameter ∇_Φ and of the shoulder parameter K, for $M = 100 - 1200$, $L = 3 - 19$, $\Phi = 0.25 - 1.0$

Sharp indent

The next step is to account for the non-linearity associated with deeper indents. The behavior of the additional pressure amplitude when increasing the indent depth is complex and depends on the contact conditions. Actually, the non-linear behavior is linked to the interaction between several factors. Complex piezoviscous effects are involved in the transition from the high pressure region over the indent shoulders to the medium pressure in the indent hole. The analysis is difficult because of important transient effects. Moreover, the fluid compressibility introduces an additional non-linearity. For the range of operating conditions and indent geometries used, figure 3.22 represents the dispersion of the pressure perturbations over the front shoulder ΔP^{EHL}_{FRONT}. For readability, only a few operating conditions and indent geometries are reported. A similar dispersion can be observed for the pressure over the rear shoulder ΔP^{EHL}_{REAR} in figure 3.23. Figure 3.24 represents this dispersion concerning the negative additional pressure amplitude in the indent hole ΔP^{EHL}_{CENT}. Only relatively sharp indents are represented. Concerning the negative additional pressure amplitude, a horizontal asymptote is relatively rapidly reached. It coincides with the pressure forming a plateau in the indent hole.

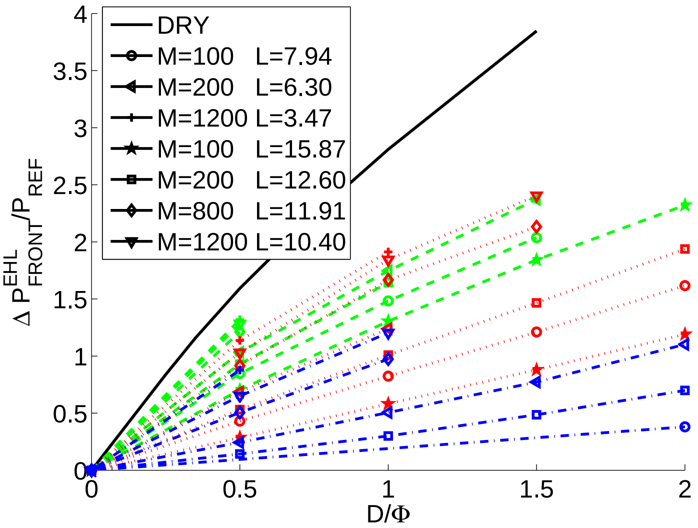

Figure 3.22: Additional pressure amplitude over the front shoulder $\Delta P^{EHL}_{FRONT}/P_{REF}$ for sharper indents $K = 4$. Blue curves for $\Phi = 0.25$, red curves for $\Phi = 0.5$ and green curves for $\Phi = 1$

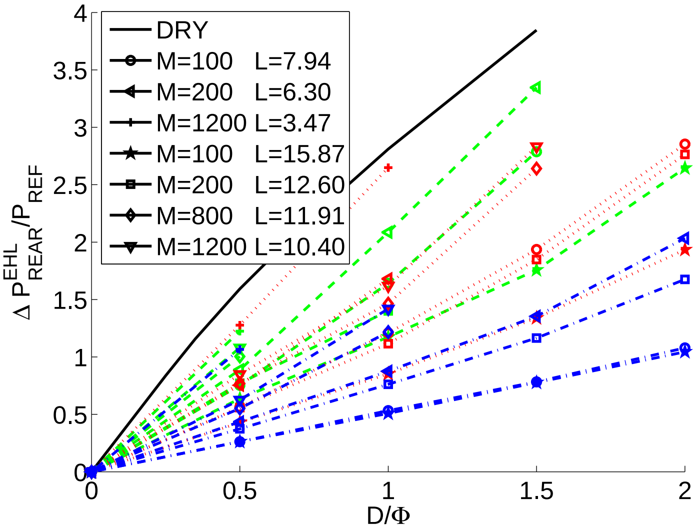

Figure 3.23: Additional pressure amplitude over the rear shoulder $\Delta P^{EHL}_{REAR}/P_{REF}$ for sharper indents $K = 4$. Blue curves for $\Phi = 0.25$, red curves for $\Phi = 0.5$ and green curves for $\Phi = 1$

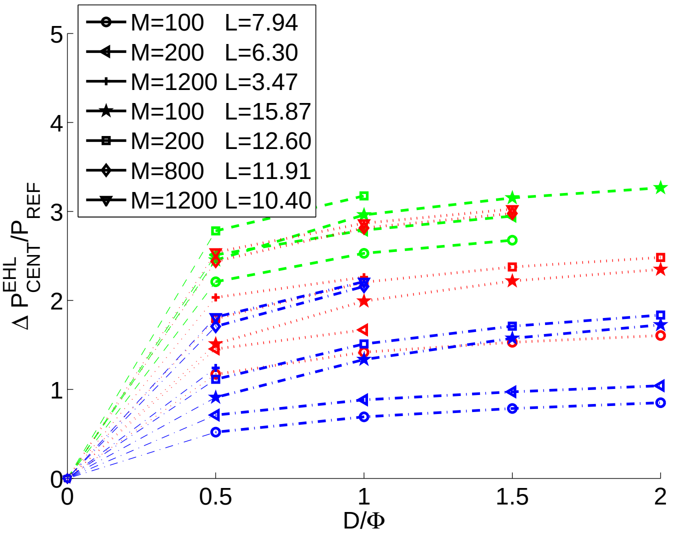

Figure 3.24: Additional pressure amplitude in the indent hole $\Delta P^{EHL}_{CENT}/P_{REF}$ for sharper indents $K = 4$. Blue curves for $\Phi = 0.25$, red curves for $\Phi = 0.5$ and green curves for $\Phi = 1$

The additional pressure is divided by the predicted initial slope from curve fits presented previously in the shallow indent study $\mathcal{S}\Delta P^{EHL}_{FIT}$. An asymptote appears logically for shallow indents. Figure 3.25 enables one to predict the pressure perturbations around sharp indents as a function of the indent geometry and the operating conditions.

Some efforts have been made to quantify the non linear effects when increasing the indent slope as a function of the operating conditions. However, the accuracy of the initial slope prediction and of the calculations themselves have not permitted a noticeable improvement in the final dispersion in figure 3.26 and 3.27. Moreover, these limited improvements lead to complex parameters without any physical interpretation. Figures 3.26 and 3.27 represent the correlation between full numerical results and fitted model predictions. The obtained correlation is considered satisfactory regarding the problem complexity.

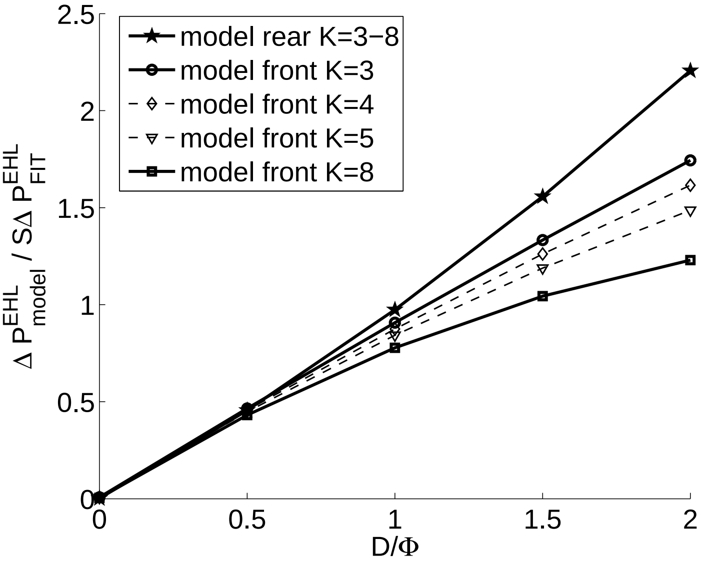

Figure 3.25: $\Delta P^{EHL}_{FRONT}/\mathcal{S}\Delta P^{EHL}_{FRONT\,FIT}$ and $\Delta P^{EHL}_{REAR}/\mathcal{S}\Delta P^{EHL}_{REAR\,FIT}$ for deeper indents. $M = 100 - 1200$, $L = 3 - 19$, $\Phi = 0.25 - 1$ and $K = 3 - 8$

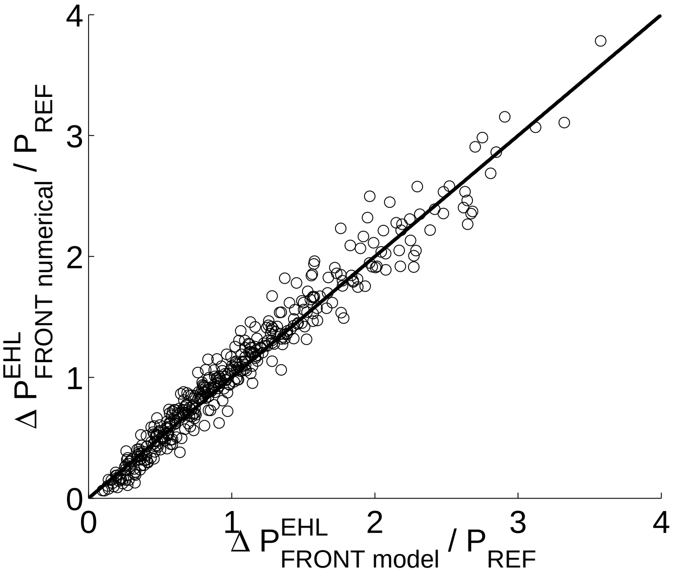

Figure 3.26: Full numerical prediction versus model predictions of the additional pressure amplitude over the front shoulder $\Delta P^{EHL}_{FRONT}/P_{REF}$ for $M = 100 - 1200$, $L = 3 - 19$, $\Phi = 0.25 - 1$, $D/\Phi = 0 - 2$ and $K = 3 - 8$

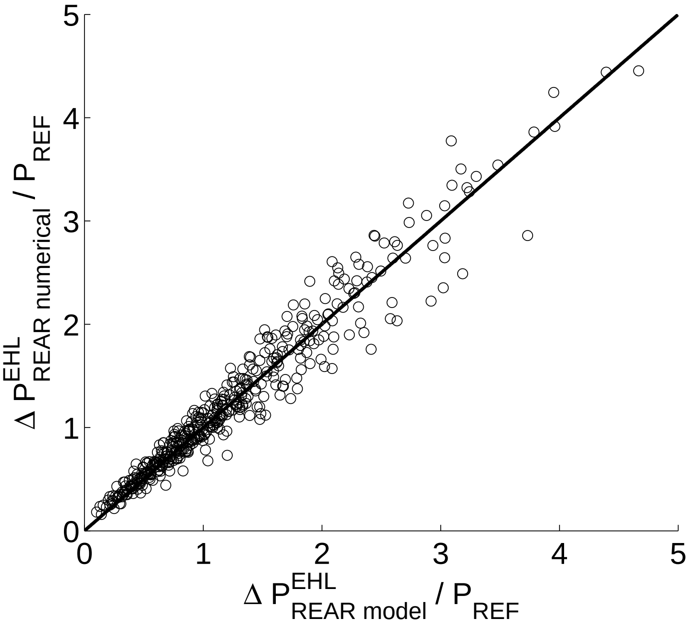

Figure 3.27: Full numerical prediction versus model predictions of the additional pressure amplitude over the rear shoulder $\Delta P_{REAR}^{EHL}/P_{REF}$ for $M = 100 - 1200$, $L = 3 - 19$, $\Phi = 0.25 - 1$, $D/\Phi = 0 - 2$ and $K = 3 - 8$

3.3.4 Sliding influence

Even if tapered roller bearings operate very close to pure-rolling, sliding exists (almost negligible). Moreover, other bearing technologies lead to sliding which can reach about 5%. The Newtonian fluid assumption can be not realistic in these cases. However, Newtonian calculations are a asymptotic case for high shear limit fluids. This section propose a limited study of the sliding influence. Only some major trends will be presented. Several authors present sliding as an important parameter Kaneta et al. [70], Ai and Cheng [1], Ai and Lee [2], Ai and Nixon [3, 4], Ville and Nelias [121], Nelias and Ville [91], Diab et al. [31]. The examples below show how a small amount of sliding of 4% can double the additional pressure amplitude.

Figure 3.28 represents an example of the pressure distribution for a centered indent for different slide to roll ratios. The slide to roll ratio is defined as the speed difference between the dented and the smooth surface divided by the velocity sum:

$$\frac{u_D - u_S}{u_D + u_S} \tag{3.10}$$

One can see that the pressure distribution is noticeably affected by sliding. Sliding has an obvious detrimental effect because of larger pressure perturbations. In this example, the pressure amplitude is almost doubled between pure-rolling and 4% sliding conditions.

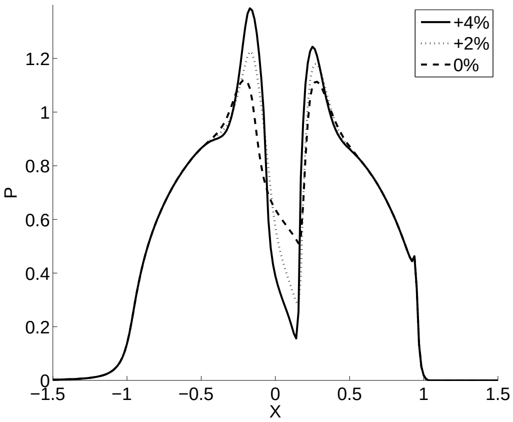

Figure 3.28: Pressure distribution for a centered indent for different slide to roll ratios $0\%, +2\%, +4\%$. Indent on the fast surface $\Phi = 0.4$, $M = 500$, $L = 8$

When comparing different slide to roll ratios, the mean speed remains the same and the indent is on the slow or the fast surface. The induced dent phenomenon can not be observed clearly with such small slide to roll ratios. However, the same physical phenomenon occurs: the lubricant becomes extremely viscous when pressure increases and the lubricant travels at the mean speed. When the lubricant geometry is shifted from the surface geometry, the edge of the surface indent is deformed by the lubricant geometry. It leads to a larger pressure perturbation.

However, even if this numerical observation was confirmed by experimental film thickness measurements, the impact of sliding on life seems to be more complex. Several authors present experimental results where the failure initiation spots are not in accordance with the largest calculated pressure and stress locations. Sliding seems to be an important parameter; however, the numerical model used in this work fails to correctly explain all details of the experimental observations. The role of the residual stresses, the friction forces and the crack propagation seem to be required to explain the life results in sliding conditions (whereas these aspects are neglected in this work). Kaneta et al. [70] studied the crack propagation directions. The orientation of the friction forces appears to be determinant. Moreover, the hydraulic pressure influence (when oil is trapped in the crack) can increase the crack propagation speed.

Sliding studies are more complex than pure-rolling conditions. For example, the pressure maximum above indent shoulders can no longer be approximated by the centered indent value. Indeed, this maximum appears at a different indent location. Figure 3.29 represents the pressure distribution at different indent locations. The additional pressure amplitudes are no longer constant during the indent crossing, the dash-dotted and the dotted curves represent the additional pressure over the front and the rear shoulder during the crossing. Jacq [65] presents an experimental work using several artificial indent sizes and operating conditions under pure-rolling or small slide to roll ratios. The author showed that the relative severity ranks of the different indents remain unchanged when introducing a small slide to roll ratio. As the model developed here will be adjusted to experimental data, one can expect that the pure-rolling calculations will be able to describe the relative severity of indents observed on bearing surfaces. Finally, in this work, the indent geometry is axysymmetric. It is already a simplification of the real indent geometry. Sliding conditions lead to much more complex natural indent geometries and pressure distributions.

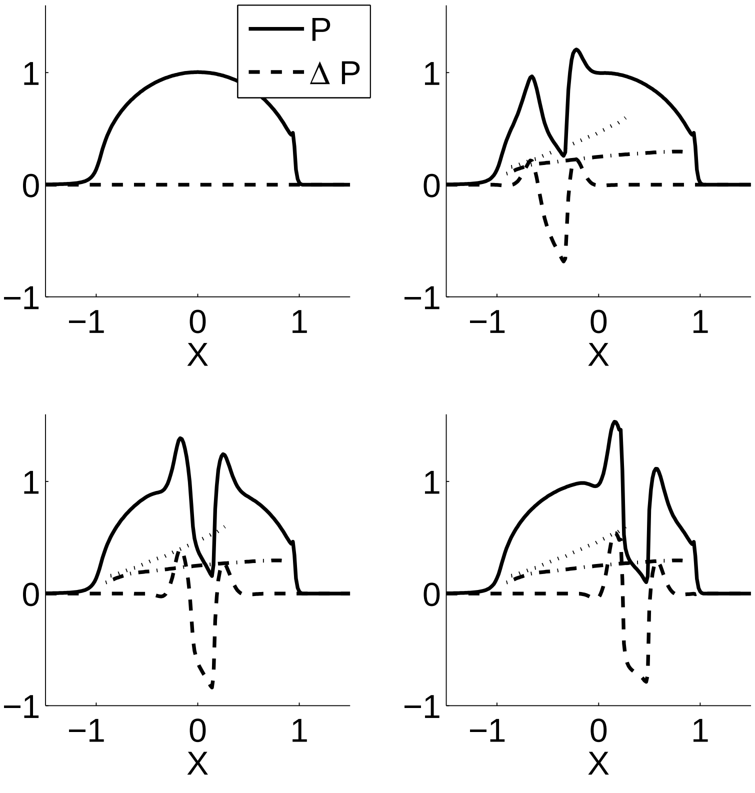

Figure 3.29: Indent traversing a +4% rolling sliding EHL contact. Indent on the fast surface $\Phi = 0.4$, $M = 500$, $L = 8$

3.4 Conclusion

Several results have been described concerning the pressure distribution in indented contacts. First, the additional pressure distribution is almost constant when an indent traverses a contact. This is both true for dry and pure-rolling EHL contacts. Therefore, most of the pressure results are presented for a centered indent. This observation will be used in the next chapter for the stress calculation. Second, some dimensionless elliptical parameters have been presented. These parameters enable one to generalize the pressure results obtained in circular contacts to wide elliptical contacts for sufficiently small indents. One dimension (especially time consuming) of the parametric study is therefore avoided. Moreover, an analytical model of the dry contact pressure perturbation was presented. Finally, curves predicting pure-rolling EHL additional pressure amplitude as a function of the indent geometry and the operating conditions were proposed. The detrimental effect of the (small) slide to roll ratio has been briefly presented.

Chapter 4

Indented contact stress and life

4.1 Introduction

The goal of this chapter is to propose a life model of indented bearings. The study of the indented contact pressure distribution in the previous chapter allowed to outline and to model some important phenomena. The step between pressure distribution and component fatigue life is not trivial. The rolling contact fatigue behavior is complex. Test campaigns are expensive (and time consuming) and lead to relatively large experimental dispersions. The numerous existing models are rarely universal and usually require experimental adjustments. It is not that easy to prove statistically that a model is better suited than another. A very brief presentation of life models is given; a discussion about the stress criteria is proposed. Some convenient applications of the conclusions of chapter 3 are proposed to facilitate the stress and life calculation. A compromise between computing time, memory requirement and numerical accuracy is presented. Moreover, stress and life prediction results are presented and a life model is proposed.

The life prediction model developed has to be correlated and adjusted to experimental data. An experimental adjustment procedure is briefly mentioned. Some experimental results concerning “natural” indentation statistics are proposed. An example is detailed.

4.2 Contact stress and life

4.2.1 Stress and life criteria

The material (steel) is far from simple. At a sufficiently small scale, it is very heterogeneous. Many defects are present. The defects vary substantially in terms of nature, size, depth and finally severity. Fatigue failure is associated with crack initiation and finally spalling. Defects play the role of stress raisers and cracks are initiated in their vicinity. These weak points are randomly distributed throughout the material. Depending on the loading cycle, these defects are activated or not. Dudragne and Girodin [34], Piot et al. [97] present a model which is based on material defect statistics and crack propagation calculations. However, the defect "severity" is not easy to evaluate. The microscopical behavior modeling often requires the identification of material parameters.

Some macroscopic fatigue criteria assume that the time between crack initiation and its propagation is sufficiently small to be neglected. The random distribution of material defects can be modeled using a statistical Weibull approach. The Weibull approach was developed for rolling contact fatigue (RCF) by Lundberg and Palmgren [87]. The authors experimentally linked the failure probability $\mathcal{F}$ to the τ_{xz} stress amplitude under Hertzian loading, to the stressed volume v and to the maximum stress depth z, see equation 4.1. Four parameters are adjusted to fit the experimental data: the stress exponent c, the Weibull slope e, the depth exponent h and the constant cst.

$$\mathcal{F} = 1 - cst\, L^e \, \frac{\tau_{xz}^c \, v}{z^h} \tag{4.1}$$

Ioannides and Harris [64] propose a criterion which is the extension of Lundberg and Palmgren's work. The stress distribution is integrated over the volume instead of considering only its maximum, see equation 4.2. The dimensionless risk integral is defined in equation 4.4. Since then, the study of various surface patterns or defects was possible. The notion of infinite life was also introduced. Lubrecht et al. [82] demonstrated that the depth term z^h had no physical meaning and lead to a singular behavior close to the surface.

$$\mathcal{F} = 1 - cst\, L^e \iiint_\Omega \frac{max\,(\tau - \tau_\infty\,;\,0)^c}{z^h}\, \mathrm{d}x\, \mathrm{d}y\, \mathrm{d}z \tag{4.2}$$

$$I = \iiint_\Omega max\,(\tau - \tau_\infty\,;\,0)^c \;\, \mathrm{d}x\, \mathrm{d}y\, \mathrm{d}z = p_H^c b^3 \bar{I}^c \tag{4.3}$$

$$\bar{I}^c = \iiint_\Omega max\,(T - T_\infty\,;\,0)^c \;\, \mathrm{d}X\, \mathrm{d}Y\, \mathrm{d}Z \tag{4.4}$$

Several choices are possible concerning the stress criterion. Tresca and Von Mises are commonly used in RCF studies. Actually, these criteria are more plasticity than fatigue criteria. Most recent studies are based on more sophisticated multiaxial fatigue criteria. Multiaxial criteria, for example Dang Van [29] or Papadopoulos [95], are based on the stress variation amplitude in every material point. These multiaxial criteria consider that every material point is submitted to a stress cycle. At a microstructural scale, the material accommodates this stress cycle by changing its microstructure. The variation around this stabilized stress state is studied for fatigue predictions. A coupling with the hydrostatic stress is then made [1].

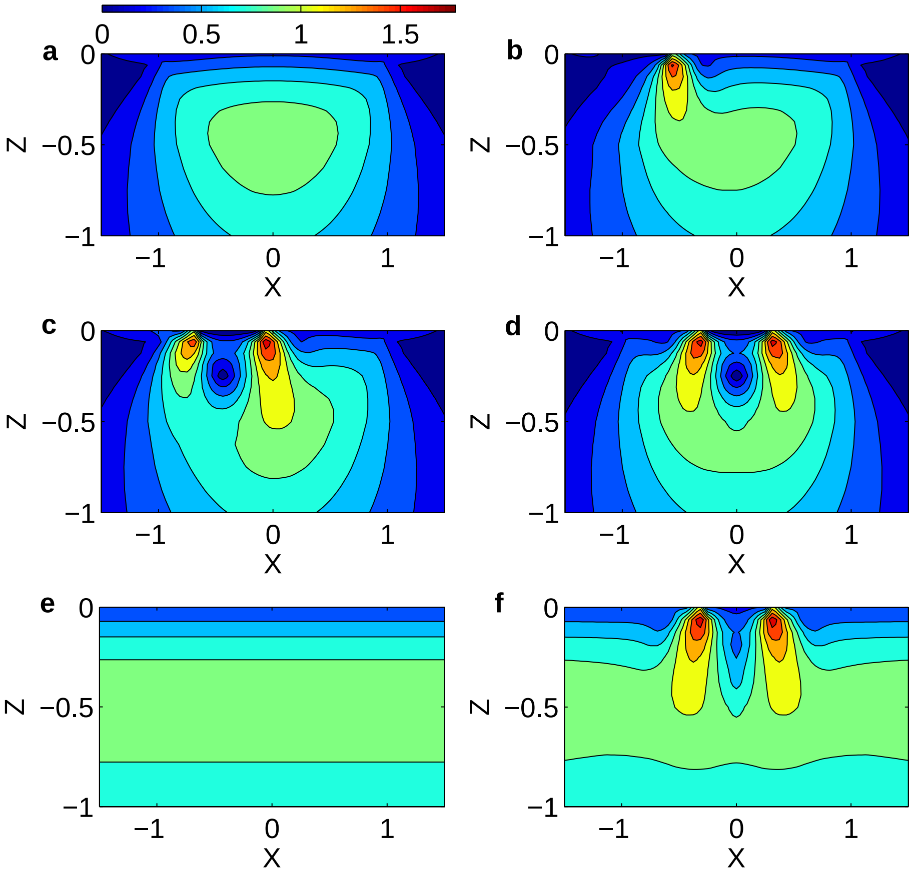

Figure 4.1: Stress distribution $\sigma^{VM}/\sigma^{VM}_{S\,max}$ at different indent locations a-d, and stress amplitude history e-f in the vertical plane along the rolling direction for a circular dry contact (e smooth, f dented), $\Phi = 0.5$, $K = 3$

---

[1] Without entering in too many details, the residual stresses (manufacturing, running in. . .) or constant stress like hoop stress play no role in the variation around the stabilized stress state. Actually, they appear only in the hydrostatic pressure coupling.

Figure 4.1 shows the stress amplitude history around an indent. This figure represents the stress distribution at different indent locations (plots 4.1 a-d) in a vertical plane along the rolling direction X. For every contact location, the stress distribution in the volume is calculated. One can see that the pressure perturbation on the surface due to an indent induces a high stress zone close to the surface. For a simple criterion like Von Mises, the stress amplitude history is defined as the maximum stress endured by each point during the contact crossing. For a multiaxial criterion, a more sophisticated treatment is used. However, it is shown further on that relatively similar results are obtained. If a smooth contact is used, horizontal isovalues are obtained, see plot 4.1 e. For an indented contact, one obtains a more complex distribution, see plot 4.1 f. To be able to compare the stress distribution between different criteria, every stress value has been normalized by the smooth contact maximum stress amplitude.

Several remarks concerning RCF predictions can be made. First, the Dang Van or Papadopoulos multiaxial criterion evaluation is much more complex and requires to calculate and to store the stress of every material point at every time step. Second, RCF tests are submitted to such large confidence intervals that it is very difficult to prove the benefits in life prediction accuracy from one criterion to an other, unless their predictions differ significantly. However, if the beneficial coupling effect of high compressive hydrostatic stress is generally accepted, Desimone et al. [30] show that under certain condition high compressive hydrostatic stresses have an adverse effect on fatigue life. Finally, the RCF life predictions are not made as “absolute” life, but with respect to a material constant which is experimentally adjusted. If different criteria give “homothetical” stress histories, the material constant will more or less integrate the different proportionality coefficients. It is especially true for the Tresca, Von Mises, Dang Van and Papadopoulos criteria used in Hertzian smooth rolling contacts.

Figure 4.2 represents the stress amplitude history for Papadopoulos’ multiaxial criterion around an indent in a dry contact in a vertical plane along the rolling direction axis X. The indent is centered in $X = Y = 0$. One can see that far from the indent, the maximum value returns logically to 1. Indeed, the stress perturbations due to the indent are sufficiently far to vanish and the stress distribution becomes that of a smooth contact. The stress amplitude history for the Papadopoulos multiaxial criterion looks similar to the stress distribution obtained with a simple Von Mises criterion in figure 4.1 f. A more detailed comparison is made in the next section.

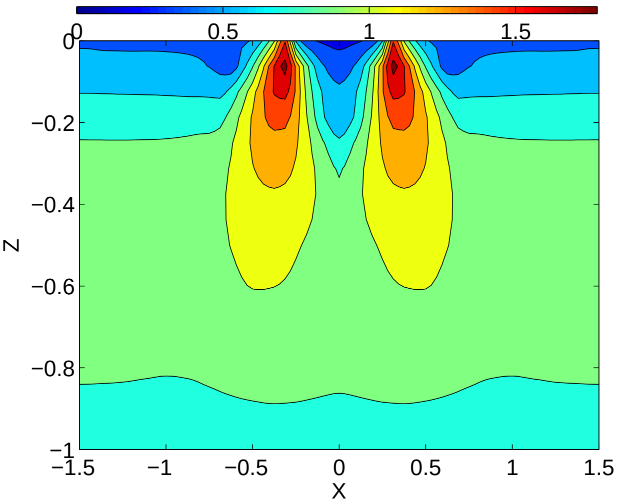

Figure 4.2: Indented contact stress amplitude history $\sigma^{PA}/\sigma^{PA}_{S\,max}$ for Papadopoulos' multiaxial criterion for a circular dry contact, $\Phi = 0.5$, $K = 3$

4.2.2 Pseudo-transient calculation

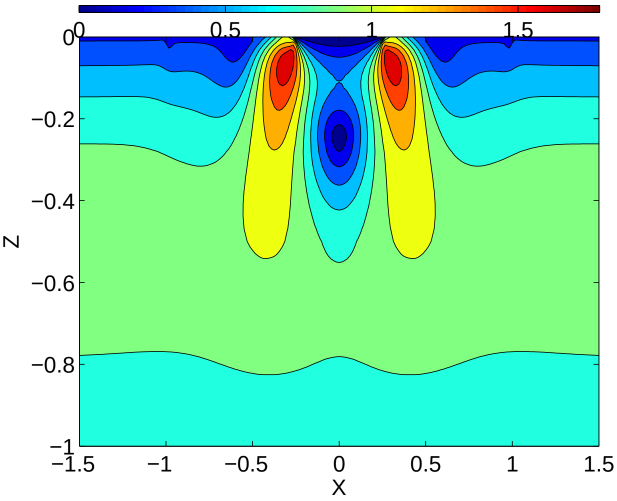

Figure 4.3: Indented contact stress amplitude history $\sigma^{VM}_{PT}/\sigma^{VM}_{S\,max}$ in the vertical plane along the axis X for a pseudo-transient calculation for a circular dry contact, $\Phi = 0.5$, $K = 3$

Pure elastic deformation is assumed. The associated stress distribution is an elastic stress field. This means that the stress tensor can be linearly divided into two tensors using the superposition principle. A considerable shortcut can be made if this decomposition is chosen carefully.

$$\sigma_{tot} = \sigma_S + \sigma_D \tag{4.5}$$

Chapter 3 presented two important results for the stress calculation. First, the additional pressure distribution is constant during the indent crossing. Second, the ellipticity hardly modifies this additional pressure distribution for sufficiently small indents. This leads to two interesting results:

First, the complete stress history around an indent can be emulated using only the centered indent stress distribution and the smooth stress distribution. This will be referred to as a "pseudo-transient" calculation. Instead of calculating and storing the pressure values at every time step and also the stress distribution, only two time steps are needed: the one of smooth contact and the centered indent. It represents an important gain in computing time and memory[2].

Second, the smooth stress distribution can be replaced by the smooth stress distribution of any ellipticity[3]. It leads to the same conclusions as for the pressure. The elliptical analysis, an especially time consuming parameter because of the number of unknowns, is thus avoided.

Of course, the pseudo-transient calculation has a drawback in terms of result accuracy. Moreover, some special care is needed when the two stress distributions are assembled emulating every time step. For example, the additional stress distribution σ_D has absolutely no meaning when the indent is out of the contact.

Figure 4.3 represents the stress history around an indent in a vertical plane along the rolling direction X for a simple Von Mises pseudo-transient approximation. The corresponding complete Von Mises calculation is represented in figure 4.1 f and the Papadopoulos multiaxial calculation in figure 4.2. The stress distributions are relatively similar. The complete Von Mises calculation and pseudo-transient approximation are almost identical. A slight difference is found in the stress distribution under the indent hole. It can undoubtedly be neglected because the stress is especially small in this very region. Concerning the comparison between the multiaxial criterion and the pseudo-transient approximation, the difference is more significant. The stressed volume seems more important for the Papadopoulos criterion. However, the maximum stress value is similar. The maximum stress has an important weight in the stress risk because of the power c in the equation 4.2.

---

[2] Typical calculations use a 256×256 grid on the surface, an equivalent of about 24 grids in depth for each stress tensor component and about 256 time steps. These two stress distributions are artificially shifted to simulate the indent movement. It represents about 2.5 billion numbers ($20\,Go$ of data if all the values are needed as in the Dang Van or Papadopoulos criteria).

[3] The infinitely elongated contact stress distribution is detailed in appendix C.

		$D/\Phi = 1$	$D/\Phi = 2$
$\Phi = 0.25$	$K = 3$	**5%**	**6%**
	$K = 8$	**3%**	**4%**
$\Phi = 0.5$	$K = 3$	**8%**	**7%**
	$K = 8$	**7%**	**7%**

Table 4.1: Difference between different stress criteria $\left(\sigma^{PA}_{D\,max}/\sigma^{PA}_{S\,max} - \sigma^{VM}_{D\,max}/\sigma^{VM}_{S\,max}\right) / \left(\sigma^{VM}_{D\,max}/\sigma^{VM}_{S\,max}\right)$ as a function of the indent diameter Φ, the indent slope D/Φ and the decay coefficient K for dry contacts

Table 4.1 represents the comparison between two stress criteria (Papadopoulos' multiaxial and Von Mises) of the maximum indented contact stress amplitude normalized by the maximum smooth contact stress amplitude as a function of the indent geometry. The Von Mises complete calculation is used as a reference. The difference between a Von Mises complete calculation and a Von Mises pseudo-transient approximation is less than 1%, thus it is not reported. The Papadopoulos and the Von Mises cases give similar variations. For this study and the range of parameters used, the multiaxial Papadopoulos criterion is systematically more severe. For example, the difference between the Papadopoulos multiaxial criterion and the Von Mises criterion for an indent diameter $\Phi = 0.25$, an indent slope $D/\Phi = 1$ and a shoulder parameter $K = 3$ is 5%.

The difference is limited and only much better experimental campaigns can reduce experimental confidence intervals and justify a more sophisticated stress criterion. The goal is only to show that the different criteria lead to similar results[4]. The computational effort of a multiaxial criterion was not justified regarding the assumptions and above remarks. Thus a simple Von Mises criterion with a pseudo-transient approximation is used.

4.2.3 Stress and life prediction

The additional pressure amplitude study was justified for several reasons. First, the maximum elastic stress is linearly proportional with the additional pressure amplitude. Figure 4.4 represents the maximum stress $\sigma_{D\,max}/\sigma_{S\,max}$ as a function of the additional pressure amplitude $\Delta P/P_{REF}$ for dry contacts. This figure confirms that the maximum stress varies linearly as a function of the additional pressure amplitude. The results from chapter 3 concerning the additional pressures are thus relevant to the contact sever-

---

[4] Note that the residual stress influence is not investigated here. Lubrecht et al. [85] show some results using the indentation residual stress. They conclude that for pure-rolling conditions and the obtained indent geometries, the indentation residual stress is beneficial because of high compressive stress under the indent shoulders.

ity. Second, the additional pressure study enables one to have a more direct understanding of the different phenomena. An important part of chapter 3 is based on the shallow indent pressure perturbation study. The equivalent study in terms of stress would be difficult.

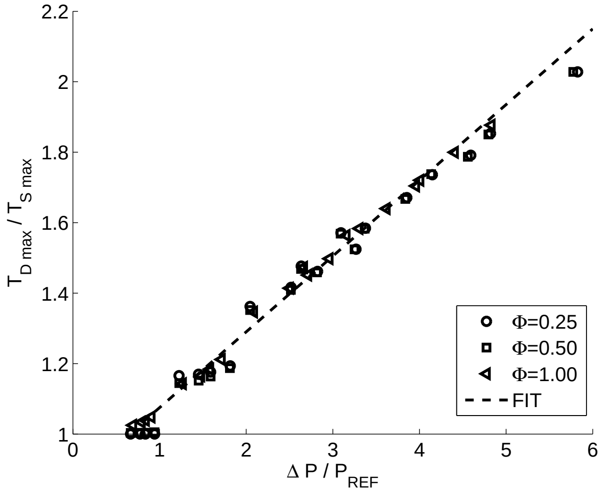

Figure 4.4: Maximum stress $T_{D\,max}/T_{S\,max}$ as a function of the additional pressure amplitude $\Delta P/P_{REF}$ for dry contacts, $\Phi = 0.25 - 1.0$, $D/\Phi = 0.25 - 2$ and $K = 3 - 8$

The reader has probably noticed that most results are presented using dimensionless parameters. When the dimensional maximum stress is calculated from its dimensionless value, a question can arise: How can the calculated dimensional stress exceed the material plasticity limit? Figure 4.4 shows that some of the calculated dimensionless stresses reach twice the maximum Hertzian stress for the range of parameters used in this study. If this particular indent was measured from a contact run under a $2.5\,GPa$ Hertzian pressure, it would mean that it could induce a shear stress close to $1.8\,GPa$. A common plasticity limit for bearing steel is $1.5\,GPa$. This particular indent geometry can not exist in this contact. It would have been deformed during the running in process until the induced stress is lower than the local plasticity limit (including isotropic and kinematic hardening). However, if this indent geometry is effectively measured after running in, it means that it does not induce any plastic deformation. The material has been locally hardened and the residual stresses are opposed to the stress distribution associated with the indent deformation. The global stress distribution does not lead to plastic deformation. Moreover, the stress amplitude endured by each material point during the loading cycle can be approximated by the elastic stress amplitude.

Figure 4.5 represents the dimensionless risk integral $\bar{I}_D/\bar{I}_S$ as function

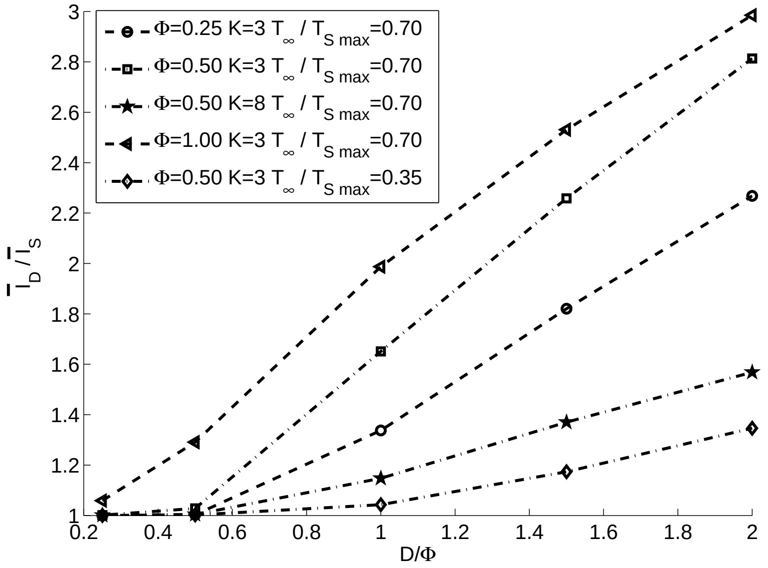

Figure 4.5: Dimensionless risk integral $\bar{I}_D/\bar{I}_S$ as a function of the indent geometry Φ, D/Φ and K and of the dimensionless infinite life limit $T_\infty/T_{S\,max}$ for dry contacts

of the indent geometry K, D/Φ, Φ and the dimensionless infinite life limit T_∞. The curves presented in figure 4.5 show that all these parameters have a significant impact on the dimensionless risk integral. The indent geometry influences both the stress amplitude and the stressed volume. For example, the first, second and fourth curves show how the stressed volume (increasing with Φ) influences the risk integral. The second and third curves compare two different shoulder shapes. Finally, the second and fifth curves compare two $T_\infty/T_{S\,max}$ ratios. The dimensionless infinite life limit influences the relative weight between the high stressed zone under the indent shoulders and the Hertzian smooth contact stressed zone. The highly stressed zone influence increases with this dimensionless infinite life limit (for example decreasing the Hertzian pressure).

The detrimental impact of an indent increases (relatively) for low Hertzian pressures. First, the indent slope and diameter are inversely proportional to the contact half width. Second, the dimensionless infinite life limit increases when decreasing the Hertzian pressure. These two points increase the dimensionless risk integral ratio.

The stress distribution can be schematically divided into two contributions: an annular highly stressed zone close to the surface due to the indent pressure perturbations and a Hertzian smooth contact stress distribution zone. The following equation is proposed to approximate the corresponding risk integral:

$$\left(\frac{\bar{I}_D}{\bar{I}_S}\right)^c = q_K(K) \cdot q_{T_\infty}\left(\frac{T_\infty}{T_{S\,max}}\right) \cdot \Phi^3 \cdot \left(\frac{\dfrac{T_{D\,max}}{T_{S\,max}} - \dfrac{T_\infty}{T_{S\,max}}}{1 - \dfrac{T_\infty}{T_{S\,max}}}\right)^c + 1 \qquad (4.6)$$

The functions $q_K(K)$ and $q_{T_\infty}(T_\infty/T_{S\,max})$ in equation 4.6 are adjusted to fit the numerical results. They account respectively for two points: first, the highly stressed volume depends on K (because the additional pressure half width is a function of K); second, the stress integration domain is a function of $T_\infty/T_{S\,max}$ and an adjustment is required. Figures 4.6 a, b and c represent respectively the function $q_K(K)$, the function $q_{T_\infty}(T_\infty/T_{S\,max})$ and $\bar{I}_S/\bar{I}_{S\,T_\infty=0}$ as a function of $T_\infty/T_{S\,max}$. The figures and the equation 4.6 allow to predict the dimensionless risk integral for dry contacts. The maximum stress $T_{D\,max}$ is known from the figure 4.4 and finally from the additional pressure amplitude predictions of chapter 3. The correlation between full numerical calculations and the simplified model is good, see figure 4.7.

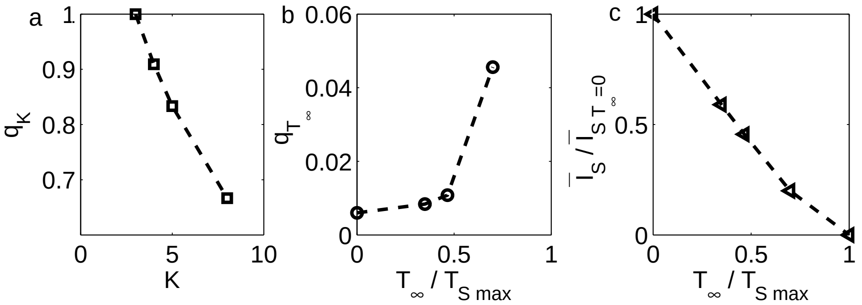

Figure 4.6: Adjustment functions $q_K(K)$ (plot a) and $q_{T_\infty}(T_\infty/T_{S\,max})$ (plot b), dimensionless risk integral $\bar{I}_S/\bar{I}_{S\,T_\infty=0}$ as a function of the dimensionless infinite life limit $T_\infty/T_{S\,max}$ for dry contacts (plot c)

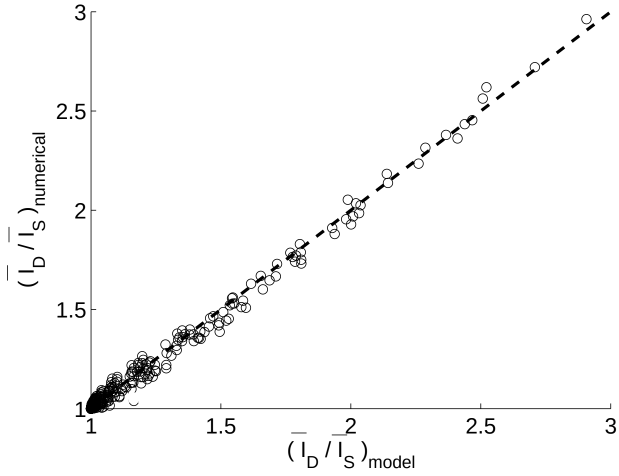

Figure 4.7: Full numerical dimensionless risk integral as a function of the model prediction for dry contacts, $c = 6.3 - 11.3$, $T_\infty/T_{S\,max} = 0.3 - 0.7$, $\Phi = 0.25 - 1.0$, $K = 3 - 8$

4.3 Experimental indentation and life calculation

4.3.1 Natural indentation and model adjustment

Surface indentation from lubricant pollution is a very complex process. Chapters 1 and 2 presented some of the difficulties encountered for the indentation prediction. For example, particle nature and geometry vary substantially; operating conditions (speed, slide to roll ratio...) and lubricant supply (particle mixing...) are decisive but very difficult to evaluate. The aim of this work is not to try to predict bearing life from oil cleanliness. Our analysis starts with the indented surface geometry measured using interferometric microscopy.

Two possibilities exists: first, the indentations are formed in a real device (gear box...); second, reference pollution test conditions are used to indent the surfaces. Both methods enable one to sidestep the indentation prediction issue. The first method yields representative results of pollution in a real application. The second is well suited to compare different bearings on a common basis. For example, the influence of the heat treatment in a polluted environment can be studied this way.

The standard pollution test consists of running several bearings in a controlled polluted environment. The size class, the particle material and the particle concentration are chosen in order to reproduce indentations observed for example in an automotive gear box. The damage should be appropriate to correctly evaluate the indented bearing lives. After the indentation procedure, the bearings are cleaned and mapped. Many spots on the surface are measured. Pit statistics (geometry, density, location) are obtained from the numerical treatment of the surface mapping. Then, the bearings are life tested and compared to clean bearing lives using a standard life test procedure. A correlation between measured surface indentation and component lives is made. The numerical constants are adjusted to these experimental results.

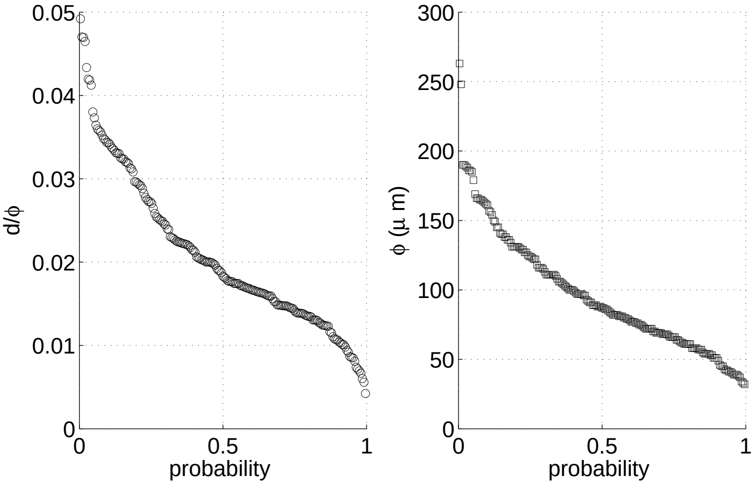

Figure 4.8: Indent slope d/ϕ (left) and indent diameter ϕ (right) cumulative distribution from a standard pollution test

A common ratio between clean and standard pollution life tests[5] with $90 - 125\,\mu m$ ductile particles is a factor 10. Figure 4.8 shows indent parameters of indented bearing topography results. It represents on the left, the slope and on the right, the diameter sorted in descending order. For example, one can see that 50% of the measured pits have a slope exceeding[6] 0.018 and that 50% of the measured pits have a diameter exceeding $85\,\mu m$. These median values should be taken with precaution. They depend sensibly on the surface mapping interpretation. Distinguishing roughness from flat indents is not always trivial[7].

Figure 4.9 (left) represents the correlation between the indent diameter and the indent slope. For each class of indent slopes, the maximum, the median and the minimum indent diameters are plotted. One can clearly see that the sharpest indents have the smallest diameter. For the 0.02 indent slope class, indent diameters are distributed between 50 and $180\,\mu m$, the median value is around $80\,\mu m$. This example agrees with Ville [119] table

---

[5] Depends obviously on many parameters as particle concentration, operating conditions…

[6] corresponding to 2°

[7] Several criteria are used: depth, circularity…

2.1 where the sharpest indents have the smallest diameters and correspond to the smallest particles.

However, these results are obtained in an experimental device where particles pass the contact only once. Under Ville's conditions, the indent slope dispersion was small. In a rolling element bearing, a particle is trapped in the bearing and it is laminated several times. Therefore, even for the unique particle size class used here, the indent slopes vary between zero and the maximum slope. The smallest sharp indents correspond certainly to the first particle squashing and large shallow indents to the next overrollings. Figure 4.9 (right) represents the probability of every indent slope class used for the left plot. The cumulative distribution and density probability functions are plotted. For example, the 0.02 indent slope class represents 35% of the entire indent population and 70% of the entire indent population belongs to this class or a shallower indent slope class.

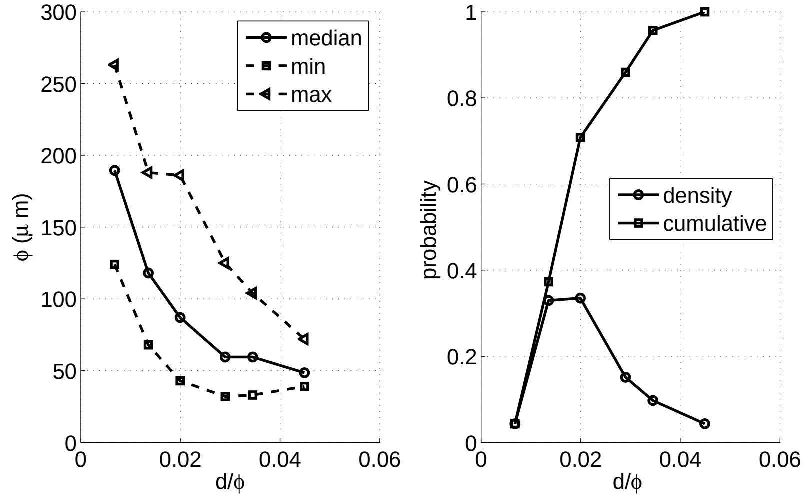

Figure 4.9: Indent diameter as a function of the indent slope (left) and probability of every indent slope class (right) from a topography measurement of a standard pollution test

The indent distribution of inner and outer ring are very close. The inner ring indents seem slightly larger and deeper, perhaps due to a slightly higher Hertzian pressure. Rolling bearings have specific kinematics: rotating or fixed inner and outer rings, and cage and roller relative motion. The number of indents (or the indent density) can be estimated using these kinematics: overrolling contact frequency and loaded surface. This study is not detailed here, as the results are not completely satisfying. The inner ring density prediction is too small compared to measurements.

An example of common contact conditions is detailed below. It is a simplification of contact conditions in a bearing. For clarity, a unique Hertzian pressure amplitude and approximated operating conditions are used. However, these values are representative of common contact conditions in tapered roller bearings. The mean bearing cone diameter is set to 5 cm and the mean roller diameter to 7.8 mm. The bearing rotates at 2000 revs/mn.

$$
\begin{aligned}
R_{x\,\kappa=\infty} &\approx 3.9\textsc{e}\text{-}3\,\mathrm{m}\\
E' &= 226\textsc{e}9\,\mathrm{Pa}\\
b &\approx 152\textsc{e}\text{-}6\,\mathrm{m}\\
p_H &\approx 2.2\textsc{e}9\,\mathrm{Pa}\\
R_{x\,\kappa=1} &\approx 5\textsc{e}\text{-}3\,\mathrm{m}\\
\frac{T_\infty}{T_{S\,max}} &\approx 0.7\\
\alpha &= 20\textsc{e}\text{-}9\,\mathrm{Pa}^{-1}\\
\eta_0 &= 40\textsc{e}\text{-}3\,\mathrm{Pa.s}\\
u_s &\approx 5.9\,\mathrm{m/s}\\
M &\approx 350\\
L &\approx 17\\
\overline{\alpha} &\approx 44\\
\overline{\lambda} &\approx 4.5\textsc{e}\text{-}3
\end{aligned}
$$

The dimensionless median indent slope is 0.6. The dimensionless median indent diameter is 0.56. One can now associate a dimensionless risk integral to the indent geometry and the contact conditions. For a dry contact assumption, figure 4.10 represents the dimensionless risk integral distribution as a function of the dimensionless indent slope and the dimensionless indent diameter. The color of each point represents the risk integral value[8]. Red points indicate the most severe indents.

The second step is to recalculate the risk integrals using EHL conditions. The operating conditions and the indent geometry lead to intermediate ∇_Φ. It means that the lubricant plays an important role and modifies significantly the pressure and stress distributions. Figure 4.11 is similar to figure 4.10 using dimensionless risk integrals for EHL contacts. The most dangerous indents are shifted towards larger diameters. The explanation is straightforward using the results from chapter 3. A larger indent diameter increases the ∇_Φ value and the pressure perturbations tend to the dry contact values. However, the color scale is deceptive. As explained, for the range of parameters used in this work, the pure-rolling EHL contacts are less severe than dry contacts. If the same color scale were used for figures 4.10 and 4.11, figure 4.11 would show only blue points. The lubricated contact risk integrals certainly underestimate the contact risk in comparison with dry contact results[9].

---

[8] Several points which are very close in terms of slope and diameter can have different colors because of different shoulder shapes K.

[9] The indentation data is based on measured surface topographies and yields a significant experimental life reduction under well lubricated conditions. So, both the operating

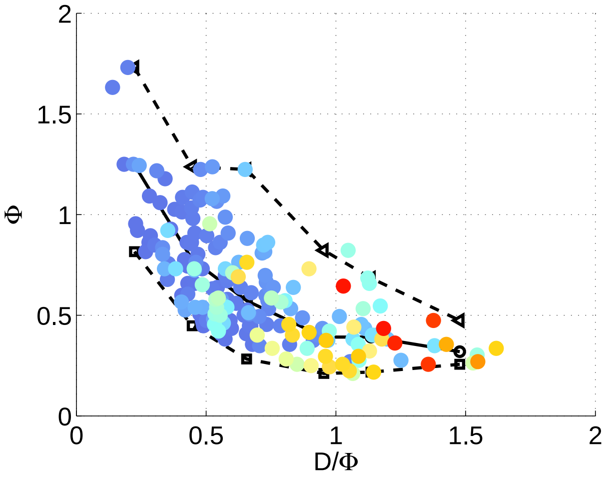

Figure 4.10: Dimensionless risk integral $\bar{I}_D/\bar{I}_S$ as a function of the indent geometry for a dry contact applied to a topography measurement of a standard pollution indentation test ($90 - 125$ μm ductile particles)

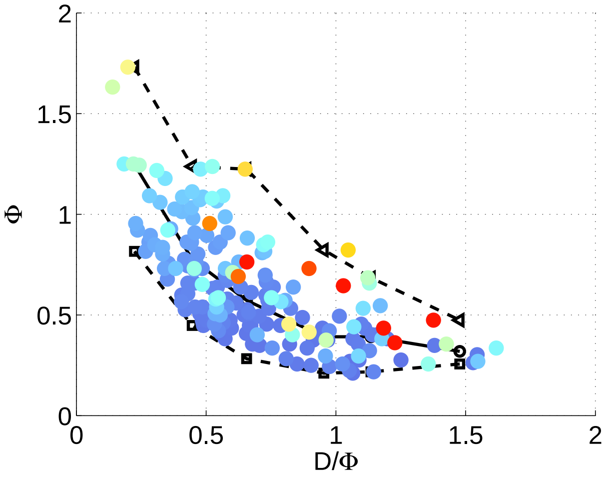

Figure 4.11: Dimensionless risk integral $\bar{I}_D/\bar{I}_S$ as a function of the indent geometry for an EHL contact applied to a topography measurement of a standard pollution indentation test ($90 - 125$ μm ductile particles)

---

conditions and the indent statistics are realistic. Tapered roller bearings run very close to pure-rolling; measured indents are relatively axisymmetrical (an other indirect confirmation of pure-rolling). A non Newtonian rheology would smooth pressure excursions and underestimate EHL predictions even more. Experimental tests are conducted ensuring an important lubricant supply; thus contacts are not starved. . .

The adjustment to experimental data uses the same type of analysis. The more complex bearing operating conditions and bearing kinematics (rotating ring or not, loading zone. . .) is accounted for. A Weibull probabilistic approach is used to calculate the life reduction due to the surface indentation.

4.3.2 Life calculation

The life calculation with a Weibull approach is relatively simple since the risk integrals are known as a function of the indent geometry and the operating conditions. Considering a non rotating ring and a constant loading, each point of the ring is submitted to a constant stress cycle. The ring can be meshed using elementary surfaces S_i. Every surface S_i is associated with a risk integral I_i. The I_i distribution is made accordingly to the indentation statistics and the operating conditions over surfaces S_i. The life $L_{\vartheta i}$ is defined as the life which corresponds to a failure probability ϑ before $L_{\vartheta i}$.

The failure probability $\mathcal{F}_i$ and the $L_{\vartheta i}$ life for surfaces S_i assuming a constant Weibull slope e reads :

$$\mathcal{F}_i = 1 - e^{ln(1-\vartheta)\left(\frac{L}{L_{\vartheta i}}\right)^e} \tag{4.7}$$

$$L_{\vartheta i}^e \propto \frac{1}{I_i} \propto \frac{1}{p_{Hi}^c\, b_i^3\, \bar{I}_i^c} \tag{4.8}$$

The surface S fails when the first elementary surface S_i fails, it corresponds to a product of survival probabilities. The entire surface L_ϑ life reads :

$$L_\vartheta^e = \frac{1}{\sum \frac{1}{L_{\vartheta i}^e}} \tag{4.9}$$

Finally, it is possible to write the ratio between the dented surface life and the smooth surface life :

$$\left(\frac{L_\vartheta}{L_{\vartheta S}}\right)^e = \frac{\sum p_{Hi}^c\, b_i^3\, \bar{I}_{Si}^c}{\sum p_{Hi}^c\, b_i^3\, \bar{I}_i^c} \tag{4.10}$$

An adjustment to experimental life tests can be made using the parameter c. This parameter appears explicitly in the terms p_{Hi}^c and implicitly in the dimensionless risk integrals $\bar{I}_i$.

4.4 Conclusion

Several fatigue life prediction models exist. A classic Weibull approach is used in this work because of its high efficiency to simplicity ratio. Different stress criteria are briefly presented. They lead to similar results, thus the simplest one is preferred. An approximate calculation is proposed referred to as pseudo-transient. It is based on the conclusions from chapter 3 concerning the pressure in elliptical contacts and during the contact crossing. The accuracy of this approximation is satisfactory and it allows a substantial time and memory saving.

The maximum stress due to the indent is directly linked to the additional pressure amplitude. Moreover, the risk integral is studied. A predictive model is proposed and a good correlation is obtained. The risk integral is written as a function of the stressed volume, the maximum stress value and the infinite life limit. This model allows the prediction of the risk integral as a function of the indent geometry and the operating conditions.

Finally, a glimpse of the experimental work concerning indentation measurement and life prediction model adjustment is shown. Some results concerning natural indentation in a tapered roller bearing are presented, especially statistical results on indent geometry. An adjustment procedure used for indented bearing life tests is briefly mentioned.

Chapter 5

General conclusion

In industrial applications, lubricant pollution can not be avoided. Controlled manufacturing processes or lubricant filters can limit this pollution. Material resistance to pollution is also constantly improved. However, the necessity to predict the life reduction due to lubricant pollution persists. The lubricant film thickness is usually much less than the particle size. When the particles enter the contact, they are squashed between the two surfaces. The surfaces are deformed plastically creating an indent.

The indent geometry is complex to predict because it is a function of many parameters: particle nature and size, material properties, operating conditions, particle mixing and lubricant supply... The aim of this work is to predict the indent severity as a function of the indent geometry and the operating conditions. The surface indentation is supposed to be known from a surface measurement.

Chapter 2 presents the main equations and the simplifications used for the contact pressure calculation (dry and EHL contacts) and for stress distribution calculation. The indent analytical description is presented. A compromise between description precision and calculation capability (time, stability, accuracy...) is necessary. Multigrid techniques[1] are used to solve contact equations and to calculate deformation and risk integrals.

Chapter 3 studies the indented contact pressure. Dry and pure-rolling lubricated contacts are both studied. Three questions are asked: What happens when the indent traverses the contact? What is the influence of the contact ellipticity? What are the important parameters to model the indented contact pressure?

- For the range of parameters used in this work (indent geometry and operating conditions), the centered indent calculation allows to pre-

---

[1] Appendix A presents an implementation of a transient EHL line relaxation solver.

dict the entire indent crossing. The additional pressure distribution remains almost constant during the crossing[2].

- Ellipticity hardly modifies the additional pressure for sufficiently small indents (small force balance perturbation). Some elliptical results are presented.
- An analytical model is presented for dry contacts and outlines the important phenomena and parameters[3]. The indent slope and the shoulder geometry are the important parameters. The lubricated contact study is based on the amplitude reduction theory which has been extended to shallow indents. The lubrication substantially modifies the pressure perturbations, from a complete damping to almost no changes. Some curves are presented to predict the EHL indented contact pressure perturbations.

  Sliding, even limited, has an important detrimental effect. Some results are briefly presented. No detailed study is proposed as indents that are created under rolling sliding conditions have complex geometries (not correctly described by the axisymmetrical model).

Chapter 4 presents some indented contact stress results and life prediction calculations. A brief study concerning the choice of the stress criterion and convenient application of some results of chapter 3 are presented. A simple Von Mises stress criterion is used; however, more sophisticated multiaxial criteria give similar results.

The maximum stress varies linearly with the additional pressure amplitude. A Weibull life prediction approach is presented; some curves for the risk integral prediction are presented as a function of the operating conditions, the indent geometry and the material infinite life limit.

Some results on natural indentation consecutive to a standard indentation test with $90-125\,\mu m$ ductile particles are shown. The sharpest indents are found to be the smallest. The indentation geometry statistics for rolling element bearings is specific because of the numerous overrollings. A simplified example for a gear box tapered roller bearing is also presented.

A life prediction tool for (indented) rolling element bearings has been developed and implemented. First, the surface topography analysis has been improved and is still being studied; second, the specific kinematic and loading cycle has been accounted for.

---

[2] neglecting the outlet Newtonian pressure spike for EHL contacts

[3] some details in appendix B

First and foremost, the next step is an experimental validation and correlation. Such validations are time consuming and expensive. The tests should at the same time show statistically significant differences and respect realistic conditions. Typically, one should obtain simultaneously the same damage type as observed in real applications, show statistically significant (quite large) differences between tested groups and be feasible on a practical time scale (especially for "clean" condition reference tests).

A very ambitious project is a more physical RCF model, where material RCF properties are extracted from the microstructural behavior. It is certainly *the*[4] Achilles heel of current RCF prediction in rolling element bearings.

---

[4] The reader can substitute "*the*" by "*the principal*"; however, historically speaking Achilles had only one.

Bibliography

[1] Ai X. and Cheng H. S. The influence of moving dent on point EHL contacts. *STLE Tribology Transactions*, 1994, vol 37, p 323 – 335.

[2] Ai X. and Lee S. C. Effect of slide-to-roll ratio on interior stresses around a dent in EHL contacts. *STLE Lubrication Engineering*, 1996, vol 39, p 881 – 889.

[3] Ai X. and Nixon H. P. Fatigue life reduction of roller bearings due to debris denting: Part I – Theoretical modeling. *STLE Tribology Transactions*, 2000, vol 43, p 197 – 204.

[4] Ai X. and Nixon H. P. Fatigue life reduction of roller bearings due to debris denting: Part II – Experimental validation. *STLE Tribology Transactions*, 2000, vol 43, p 311 – 317.

[5] Ai X. Effect of debris contamination on the fatigue life of roller bearings. *Proc. IMechE, part J, Journal of Engineering Tribology*, 2001, vol 215, p 563 – 575.

[6] Antaluca E. and Nelias D. Contact fatigue analysis of a dented surface in a dry elastic-plastic circular point contact. *Tribology Letters*, 2008, vol 29, p 139 – 153.

[7] Åström H. and Venner C. H. Soap-thickener induced local pressure fluctuations in a grease-lubricated elastohydrodynamic point contact. *Proc. IMechE, part J, Journal of Engineering Tribology*, 1994, vol 208, p 191 – 198.

[8] Barus C. Isothermals, isopiestics and isometrics relative to viscosity. *American Journal of Science*, 1893, vol 45, p 87 – 96.

[9] Bhargava V., Hahn G. T. and Rubin C. A. An elastic-plastic finite element model of rolling contact, Part 1: Analysis of single contacts. *ASME Journal of Applied Mechanics*, 1985, vol 52, p 67 – 74.

[10] Bhargava V., Hahn G. T. and Rubin C. A. An elastic-plastic finite element model of rolling contact, Part 2: Analysis of repeated contacts. *ASME Journal of Applied Mechanics*, 1985, vol 52, p 75 – 82.

[11] BIBOULET N., LUBRECHT A. A. and HOUPERT L. Contact pressure in indented EHL contacts. *Proc. IMechE, part J, Journal of Engineering Tribology*, 2008, vol 222, p 415 – 421.

[12] BIBOULET N., LUBRECHT A. A. and HOUPERT L. Contact pressure of indented wide elliptical contacts: dry and lubricated cases. *ASME Journal of Tribology*, 2008 to be published.

[13] BOUSSINESQ J. *Applications des potentiels à l'étude de l'équilibre et du mouvement des solides élastiques.* Gauthier-Villard, Paris, 1885.

[14] BRANDT A. Multi-Level adaptative solutions to boundary value problems. *Mathematics of Computation*, 1977, vol 31, p 333 – 390.

[15] BRANDT A. Rigorous local mode analysis of multigrid. *Prelim. Proc. 4th Copper Mountain Conference of MultiGrid Methods, Copper Mountain Colorado*, 1990.

[16] BRANDT A. and LUBRECHT A. A. Multilevel matrix multiplication and fast solution of integral equations. *Journal of Computational Physics*, 1990, vol 90, p 348 – 370.

[17] CANN P. M. E., HAMER J. C., SAYLES R. S., SPIKES H. A. and IOANNIDES E. Direct observation of particle entry and deformation in a rolling EHD contact. *Proceedings of the 22nd Leeds-Lyon Symposium on Tribology*, 1996, p 127 – 134.

[18] CHAPKOV A. *Etude des contacts elastohydrodynamiques lubrifiés avec un fluide non Newtonien.* PhDthesis: INSA-LYON, Lyon, France, 2006.

[19] CHAPKOV A., COLIN F. and LUBRECHT A. A. Influence of harmonic surface roughness on the fatigue life of elastohydrodynamic lubricated contacts. *Proc. IMechE, part J, Journal of Engineering Tribology*, 2006, vol 220, p 287 – 294.

[20] CHENG W., CHENG H. S. and KEER L. M. Longitudinal crack initiation under rolling contact fatigue. *STLE Tribology Transactions*, 1994, vol 37, p 51 – 58.

[21] CHENG W., CHENG H. S., MURA T. and KEER L. M. Micromechanics modeling of crack initiation under contact fatigue. *ASME Journal of Tribology*, 1994, vol 116, p 2 – 8.

[22] CHEVALIER F. *Modélisation des conditions d'alimentation dans les contacts EHD ponctuels.* PhDthesis: INSA-LYON, Lyon, France, 1996.

[23] COGDELL J. D. *Timken internal report.* Technical report, Timken company metrology laboratory, Canton, Ohio, USA, 2007.

[24] Coulon S. *Prédiction de la durée de vie des contacts ponctuels lubrifiés en présence d'indentations.* PhDthesis: INSA-LYON, Lyon, France, 2001.

[25] Coulon S., Ville F. and Lubrecht A. A. An abacus for predicting the rolling contact fatigue life reduction due to debris dents. *Proceedings of the 28th Leeds-Lyon Symposium on Tribology*, 2002, p 283 – 294.

[26] Coulon S., Ville F. and Lubrecht A. A. Effect of a dent on the pressure distribution in dry point contact model. *ASME Journal of Tribology*, 2002, vol 124, p 220 – 222.

[27] Coulon S., Jubault I., Lubrecht A. A., Ville F. and Vergne P. Pressure profiles measured within lubricated contact in presence of dented surfaces. Comprison with numerical models. *Tribology International*, 2004, vol 37, p 111 – 117.

[28] Damiens B. *Modélisation de la lubrification sous-alimentée dans les contacts elastohydrodynamiques elliptiques.* PhDthesis: INSA-LYON, Lyon, France, 2003.

[29] Dang Van K., Le Douaron A. and Lieurade H. P. Multiaxial fatigue limit: a new approach. *Pergamon Press, Oxford*, 1984, p 1879 – 1885.

[30] Desimone H., Bernasconi A. and Beretta S. On the application of Dang Van criterion to rolling contact fatigue. *Wear*, 2005, p 567 – 572.

[31] Diab Y., Coulon S., Ville F. and Flamand L. Experimental investigations on rolling contact fatigue of dented surfaces using artificial defects: subsurface analyses. *Proceedings of the 29th Leeds-Lyon Symposium on Tribology*, 2003, p 359 – 366.

[32] Dowson D. and Higginson G. R. A numerical solution to the elastohydrodynamic problem. *Proc. IMechE, part C, Journal of Mechanical Engineering Science*, 1959, p 6 – 15.

[33] Dowson D. and Higginson G. R. *Elastohydrodynamic lubrication, the fundamentals of roller and gear lubrication.* Pergamon Press, Oxford, Great Britain, 1966.

[34] Dudragne G. and Girodin D. Application au dimensionnement des roulements d'un nouveau modèle de calcul de la durée de vie. *Actes JIFT 1999 – Roulements et tribologie – AFM/GST Tribologie*, 1999, p 149 – 160.

[35] Dwyer-Joyce R. S., Hamer J. C., Sayles R. S. and Ioannides E. Surface damage effects caused by debris in rolling bearing lubricants, with emphasis on friable materials. *Rolling element bearings – towards the 21st century*, 1990, p 1 – 8.

[36] Dwyer-Joyce R. S. *The effect of lubricant contamination on rolling bearing performance*. PhDthesis: University of London, London, England, 1992.

[37] Dwyer-Joyce R. S. and Heymer J. The entrainment of solid particles into rolling elastohydrodynamic contacts. *Proceedings of the 22nd Leeds-Lyon Symposium on Tribology*, 1996, p 135 – 140.

[38] Ertel A. M. Hydrodynamic lubrication based on new principles. *Akad. Nauk SSSR Prikadnaya Mathematica i Mekhanika*, 1939, vol 3, p 41 – 52.

[39] Fenner R. T. *Engineering elasticity application of numerical and analytical techniques.* Ellis Horwood Ltd, Chichester, West Sussex, ISBN 10322757516, 1986.

[40] Foord C. A., Hamman W. C. and Cameron A. Evaluation of lubricants using optical elastohydrodynamics. *ASLE Lubrication Engineering*, 1968, vol 11, p 31 – 43.

[41] Girodin D., Ville F., Guers R. and Dudragne G. Experimental investigations of surface initiated rolling contact fatigue using dented surfaces. *Proceedings of the 27th Leeds-Lyon Symposium on Tribology*, 2001, p 449 – 458.

[42] Girodin D., Ville F., Guers R. and Dudragne G. Rolling contact fatigue tests to investigate surface initiated damage and tolerance to surface dents. *ASTM*, 2002, p 263 – 282.

[43] Gohar R. and Cameron A. The mapping of elastohydrodynamic contacts. *ASLE Lubrication Engineering*, 1967, vol 10, p 215 – 225.

[44] Greenwood J. A. and Morales-Espejel G. E. The behaviour of transverse roughness in EHL contacts. *Proc. IMechE, part J, Journal of Engineering Tribology*, 1994, vol 208, p 121 – 132.

[45] Greenwood J. A. and Morales-Espejel G. E. The behaviour of transverse roughness in EHL contacts. *Proceedings of the 23rd Leeds-Lyon Symposium on Tribology*, 1997, p 307 – 312.

[46] Gupta V., Bastias P., Hahn G. T. and Rubin C. A. Influence of indent geometry on repeated two-dimensional rolling contact. *ASME Journal of Tribology*, 1995, vol 117, p 655 – 659.

[47] Hahn G. T., Bhargava V., Rubin C. A. and Chen Q. Analysis of the rolling contact residual stresses and cyclic plastic deformation of SAE 52100 steel ball bearings. *ASME Journal of Tribology*, 1987, vol 109, p 618 – 626.

[48] Hamer J. C., Lubrecht A. A., Ioannides E. and Sayles R. S. Surface damage on rolling elements and its subsequent effects on performance and life. *Proceedings of the 15th Leeds-Lyon Symposium on Tribology*, 1989, p 189 – 197.

[49] Hamrock B. J. and Dowson D. Isothermal elastohydrodynamic lubrication of points contacts, part I – Theoretical formulation. *ASME Journal of Lubrication Technology*, 1976, vol 98, p 223 – 229.

[50] Hamrock B. J. and Dowson D. Isothermal elastohydrodynamic lubrication of points contacts, part II – Ellipticity parameter results. *ASME Journal of Lubrication Technology*, 1976, vol 98, p 375 – 383.

[51] Hamrock B. J. and Dowson D. Isothermal elastohydrodynamic lubrication of points contacts, part III – Fully flooded results. *ASME Journal of Lubrication Technology*, 1977, vol 99, p 264 – 276.

[52] Hamrock B. J. and Brewe D. Simplified solution for stresses and deformations. *ASME Journal of Lubrication Technology*, 1983, vol 105, p 171 – 177.

[53] Hertz H. On the contact of elastic solids. *J. Reine und Angew. Math.*, 1881, vol 92, p 292 – 302.

[54] Hooke C. J. Surface roughness modification in elasto-hydrodynamic line contacts operating in the elastic piezoviscous regime. *Proc. IMechE, part J, Journal of Engineering Tribology*, 1998, vol 202, p 145 – 162.

[55] Hooke C. J. Surface roughness modification in elasto-hydrodynamic line contacts - the effects of roughness wavelength, orientation and operating conditions. *Proceedings of the 25th Leeds-Lyon Symposium on Tribology*, 1999, p 193 – 202.

[56] Hooke C. J. and Venner C. H. Surface roughness attenuation in line and point contacts. *Proc. IMechE, part J, Journal of Engineering Tribology*, 2000, vol 214, p 439 – 444.

[57] Hooke C. J. and Li K. Y. An inverse approach to the validation of pressure predictions in rough elastohydrodynamic contacts. *ASME Journal of Tribology*, 2002, vol 124, p 103 – 108.

[58] Hooke C. J. and Li K. Y. Rapid calculation of the pressures and clearances in rough, elastohydrodynamically lubricated contacts under pure

rolling. Part 1: low amplitude, sinusoidal roughness. *Proc. IMechE, part C, Journal of Mechanical Engineering Science*, 2006, vol 220, p 901 – 913.

[59] Hooke C. J. and Li K. Y. Rapid calculation of the pressures and clearances in rough, elastohydrodynamically lubricated contacts under pure rolling. Part 2: general roughness. *Proc. IMechE, part C, Journal of Mechanical Engineering Science*, 2006, vol 220, p 915 – 925.

[60] Hooke C. J. and Li K. Y. Validation of the stress predictions in rolling EHL contact having in-line roughness using the inverse method. *ASME Journal of Tribology*, 2006, vol 128, p 745 – 752.

[61] Hooke C. J., Li K. Y. and Morales-Espejel G. E. Rapid calculation of the pressures and clearances in rough, rolling-sliding elastohydrodynamically lubricated contacts. Part 1: low-amplitude, sinusoidal roughness. *Proc. IMechE, part C, Journal of Mechanical Engineering Science*, 2007, vol 221, p 535 – 550.

[62] Hooke C. J., Li K. Y. and Morales-Espejel G. E. Rapid calculation of the pressures and clearances in rough, rolling-sliding elastohydrodynamically lubricated contacts. Part 2: general, non-sinusoidal roughness. *Proc. IMechE, part C, Journal of Mechanical Engineering Science*, 2007, vol 221, p 551 – 564.

[63] Howell M. B., Rubin C. A. and Hahn G. T. The effect of dent size on the pressure distribution and failure location in dry point frictionless rolling contacts. *ASME Journal of Tribology*, 2004, vol 126, p 413 – 421.

[64] Ioannides E. and Harris T. A. A new fatigue life mode for rolling bearings. *ASME Journal of Tribology*, 1985, vol 107, p 367 – 378.

[65] Jacq C. *Limite d'endurance et durée de vie en fatigue de roulement du 32CrMoV13 nitruré en présence d'indentations.* PhDthesis: INSA-LYON, Lyon, France, 2001.

[66] Jacq C., Nelias D., Lormand G. and Girodin D. Development of a three-dimensional semi-analytical elastic-plastic contact code. *ASME Journal of Tribology*, 2002, vol 124, p 653 – 667.

[67] Johnson K. L. *Contact Mechanics.* Cambridge University Press, Cambridge, ISBN 0521347963, 1989.

[68] Johnston G. J., Wayte R. and Spikes H. A. The measurement and study of very thin lubricant films in concentrated contacts. *STLE Tribology Transactions*, 1991, vol 34, p 187 – 194.

[69] Kalker J. J. Numerical calculation of the elastic field in a half-space. *Communications in Applied Numerical Methods*, 1986, vol 2, p 401 – 410.

[70] Kaneta M., Yatsuzuka H. and Murakami Y. Mechanism of crack growth in lubricated rolling/sliding contact. *ASLE Lubrication Engineering*, 1985, vol 28, p 407 – 414.

[71] Kaneta M., Sakai T. and Nishakawa H. Optical interferometric observations of the effect of a bump on point contact EHL. *ASME Journal of Tribology*, 1992, vol 114, p 779 – 784.

[72] Kaneta M., Kanada T. and Nishakawa H. Optical interferometric observations of the effects of a moving dent on point contact EHL. *Proceedings of the 23rd Leeds-Lyon Symposium on Tribology*, 1997, p 69 – 79.

[73] Kang Y. S., Sadeghi F. and Hoeprich M. R. A finite element model for spherical debris denting in heavily loaded contacts. *ASME Journal of Tribology*, 2004, vol 126, p 71 – 79.

[74] Ko C N. and Ioannides E. Debris denting - The associated residual stresses and their effect on the fatigue life of rolling bearing: An FEM analysis. *Proceedings of the 15th Leeds-Lyon Symposium on Tribology*, 1989, p 199 – 207.

[75] Kotzalas M N. and Harris T. A. Fatigue failure progression in ball bearings. *ASME Journal of Tribology*, 2001, vol 123, p 238 – 242.

[76] Li K. Y. and Hooke C. J. Use of the inverse approach to the investigate the stresses in rough elastohydrodynamic contacts. *ASME Journal of Tribology*, 2002, vol 124, p 109 – 113.

[77] Loewenthal S. H., Moyer D. W. and Needelman W. M. Effects of ultra-clean and centrifugal filtration on rolling-element bearing life. *ASME Journal of Lubrication Technology*, 1982, vol 104, p 283 – 292.

[78] Lorösch H. K. Research on longer life for rolling-element bearings. *ASLE Lubrication Engineering*, 1985, vol 41, p 37 – 43.

[79] Lubrecht A. A., Ten Napel W. E. and Bosma R. Multigrid, an alternative method for calculating film thickness and pressure profiles in elastohydrodynamically lubricated line contacts. *ASME Journal of Tribology*, 1986, vol 108, p 551 – 556.

[80] Lubrecht A. A. *Numerical solution of the EHL line and point contact problem using multigrid techniques.* PhDthesis: University of Twente, Enschede, The Netherlands ISBN 90-9001583-3, 1987.

[81] Lubrecht A. A., Ten Napel W. E. and Bosma R. Multigrid, an alternative method of solution for two-dimensional elastohydrodynamically lubricated point contacts. *ASME Journal of Tribology*, 1987, vol 109, p 437 – 443.

[82] Lubrecht A. A., Jacobson B. O. and Ioannides E. Lundberg Palmgren revisited. *Rolling element bearings – towards the 21st century, London*, 16 November 1990, p 17 – 20.

[83] Lubrecht A. A., Venner C. H., Lane S., Jacobson B. O. and Ioannides E. Surface damage - Comparison of theoretical and experimental endurance lives of rolling bearings. *Proceedings of the Japan International Tribology Conference*, 1990, p 185 – 190.

[84] Lubrecht A. A. and Ioannides E. A fast solution of the dry contact problem and the associated sub-surface stress field, using multilevel techniques. *ASME Journal of Tribology*, 1991, vol 113, p 128 – 133.

[85] Lubrecht A. A., Dwyer-Joyce R. S. and Ioannides E. Analysis of the influence of indentations on contact life. *Proceedings of the 19th Leeds-Lyon Symposium on Tribology*, 1993, p 173 – 181.

[86] Lubrecht A. A. and Venner C. H. Elastohydrodynamic lubrication of rough surfaces. *Proc. IMechE, part J, Journal of Engineering Tribology*, 1999, vol 213, p 397 – 404.

[87] Lundberg G. and Palmgren A. Dynamic capacity of rolling bearings. *Acta Polytech. Mech. Eng.*, 1947, vol 7, p 207 – 213.

[88] Moes H. *Lubrication and beyond.* technical report, code 115531, University of Twente, Enschede, The Netherlands, 2000.

[89] Morales-Espejel G. E., Venner C. H. and Greenwood J. A. Kinematics of transverse real roughness in elastohydrodynamically lubricated line contacts using Fourier analysis. *Proc. IMechE, part J, Journal of Engineering Tribology*, 2000, vol 214, p 523 – 534.

[90] Mourier L., Mazuyer D., Lubrecht A. A. and Donnet C. Transient increase of film thickness in micro-textured EHL contacts. *Tribology International*, 2006, vol 39, p 1745 – 1756.

[91] Nelias D. and Ville F. Detrimental effects of debris dents on rolling contact fatigue. *ASME Journal of Tribology*, 2000, vol 122, p 55 – 64.

[92] Nelias D. New methodology to evaluate the rolling contact fatigue performance of bearing steels with surface dents: Application to 32CrMoV13 (nitrided) and M50 steels. *ASME Journal of Tribology*, 2005, vol 127, p 611 – 622.

[93] Nixon H. P. and Zantopoulos H. Fatigue life performance comparisons of tapered roller bearings with debris-damaged raceways. *STLE Lubrication Engineering*, 1995, vol 51, p 732 – 736.

[94] Östensen J.O., Larrson R. and Venner C. H. Determination of viscosity and pressure in an elastohydrodynamic rolling contact by using optical interferometry : a theorical study. *Proc. IMechE, part J, Journal of Engineering Tribology*, 1996, vol 210, p 259 – 268.

[95] Papadopoulos I. *Fatigue polycyclique des métaux : une nouvelle approche.* PhDthesis: ENPC, France, 1986.

[96] Petrusevich A. I. *Fundamental conclusion from hydrodynamic contact theory of lubrication.* Isz. Akad. Nauk SSSR (OTN), 1951.

[97] Piot D., Lormand G., Vincent A., Baudry G., Girodin D. and Dudragne G. Modélisation microstructurale et micromécanique de la distribution des durées de vie en fatigue de roulement. *Actes JIFT 1995 – Roulements et tribologie – AFM/GST Tribologie*, 1995, p 211 – 223.

[98] Reynolds O. On the theory of lubrication and its application to Mr. Beauchamp tower's experiments, including an experimental determination of the viscosity of olive oil. *Phil. Trans. Roy. Soc. of London*, 1886, vol 117, p 157 – 234.

[99] Roelands C. J. A. *Correlation aspects of the viscosity-temperature-pressure relationship of lubricating oils.* PhDthesis: Technical University of Delft, Delft, The Netherlands, 1966.

[100] Sackfields A. and Hills D. A. Some useful results in the classical Hertz contact problem. *IMechE Journal of Strain Analysis*, 1983, vol 18, p 101 – 106.

[101] Sackfields A. and Hills D. A. Some useful results in the tangential loaded Hertzian contact problem. *IMechE Journal of Strain Analysis*, 1983, vol 18, p 107 – 110.

[102] Sayles R. S. and Macpherson P. B. Influence of wear debris on rolling contact fatigue. *ASTM*, 1982, vol STP 771, p 255 – 274.

[103] Sayles R. S. and Ioannides E. Debris damage in rolling bearings and its effects on fatigue life. *ASME Journal of Tribology*, 1988, vol 110, p 26 – 31.

[104] Smith J. O. and Liu C. K. Stresses due to tangential and normal loads on an elastic solid with application to some contact stress problems. *ASME Journal of Applied Mechanics*, 1953, p 157 – 166.

[105] Tallian T. E. A datta-fitted rolling bearing life prediction model – Part 1: Mathematical model. *Tribology International*, 1996, vol 39, p 249 – 258.

[106] Tallian T. E. A datta-fitted rolling bearing life prediction model – Part 2: Model fit to the historical experimental database. *Tribology International*, 1996, vol 39, p 259 – 268.

[107] Tallian T. E. A datta-fitted rolling bearing life prediction model – Part 3: Parametric study, comparison to published models and engineering review. *Tribology International*, 1996, vol 39, p 269 – 275.

[108] Thoquenne G. *Prévision des durées de vie en fatigue des roulements.* PhDthesis: Ecole Polytechnique, Palaiseau, France, 2004.

[109] Venner C. H. *Multilevel solution of the EHL line and point contact problems.* PhDthesis: University of Twente, Enschede, The Netherlands. ISBN 90-9003974-0, 1991.

[110] Venner C. H. and Lubrecht A. A. Numerical simulation of transverse ridge in a circular EHL contact under rolling/sliding. *ASME Journal of Lubrication Technology*, 1994, vol 116, p 751 – 761.

[111] Venner C. H. and Lubrecht A. A. Numerical simulation of waviness in a circular EHL contact under rolling/sliding. *Proceedings of the 21st Leeds-Lyon Symposium on Tribology*, 1995, p 259 – 272.

[112] Venner C. H., Couhier F., Lubrecht A. A. and Greenwood J. A. Amplitude reduction of waviness in transient EHL line contacts. *Proceedings of the 23rd Leeds-Lyon Symposium on Tribology*, 1997, p 103 – 112.

[113] Venner C. H. and Lubrecht A. A. Amplitude reduction of non-isotropic harmonic patterns in circular EHL contacts under pure rolling. *Proceedings of the 25th Leeds-Lyon Symposium on Tribology*, 1999, p 151 – 162.

[114] Venner C. H. and Morales-Espejel G. E. Amplitude reduction of small-amplitude waviness in transient elastohydrodynamically lubricated line contacts. *Proc. IMechE, part J, Journal of Engineering Tribology*, 1999, vol 213, p 487 – 504.

[115] Venner C. H. and Lubrecht A. A. *Multilevel Methods in Lubrication.* Elsevier Tribology Series, vol. 37, Amsterdam, ISBN 0 444 50503 2, 2000.

[116] Venner C. H. EHL film thickness computations at low speeds: risk of artificial trends as a results of poor accuracy and implications for mixed

lubrication modelling. *Proc. IMechE, part J, Journal of Engineering Tribology*, 2005, vol 219, p 285 – 290.

[117] Venner C. H. and Lubrecht A. A. An engineering tool for the quantitative prediction of general roughness deformation in EHL contact based on harmonic waviness attenuation. *Proc. IMechE, part J, Journal of Engineering Tribology*, 2005, vol 219, p 303 – 312.

[118] Venner C. H. and Wijnant Y. H. Validation of EHL contact predictions under time varying load. *Proc. IMechE, part J, Journal of Engineering Tribology*, 2005, vol 219, p 249 – 261.

[119] Ville F. *Pollution solide des lubrifiants, indentations et fatigue des surfaces.* PhDthesis: INSA-LYON, Lyon, France, 1998.

[120] Ville F. and Nelias D. Influence of the nature and size of solid particles on the indentation features in EHL contacts. *Proceedings of the 24th Leeds-Lyon Symposium on Tribology*, 1998, p 399 – 409.

[121] Ville F. and Nelias D. Early fatigue failure due to dents in EHL contacts. *STLE Tribology Transactions*, 1999, vol 42, p 795 – 800.

[122] Ville F. and Nelias D. An experimental study on the concentration and shape of dents caused by spherical metallic particles in EHL contacts. *STLE Tribology Transactions*, 1999, vol 42, p 231 – 240.

[123] Wang Q. J. and Zhu D. Virtual texturing: Modeling the performance of lubricated contacts of engineered surfaces. *ASME Journal of Tribology*, 2005, vol 127, p 722 – 728.

[124] Webster M. N., Ioannides E. and Sayles R. S. The effect of topographical defects on the contact stress and fatigue life in rolling element bearings. *Proceedings of the 12th Leeds-Lyon Symposium on Tribology*, 1986, vol 108, p 207 – 221.

[125] Wedeven L. D. Influence of debris on EHD lubrication. *ASLE Lubrication Engineering*, 1977, vol 21, p 41 – 52.

[126] Wedeven L. D. and Cusano C. Elastohydrodynamic film thickness measurements of artificially produced surface dents and groove. *ASLE Lubrication Engineering*, 1979, vol 22, p 369 – 381.

[127] Wijnant Y. H. *Contact dynamics in the field of elastohydrodynamic lubrication.* PhDthesis: University of Twente, Enschede, The Netherlands, 1998.

[128] Xu G., Sadeghi F. and Cogdell J. D. Debris denting effects on elastohydrodynamic lubricated contacts. *ASME Journal of Tribology*, 1997, vol 119, p 579 – 587.

[129] Xu G., Sadeghi F. and Hoeprich M. R. Residual stresses due to debris effects in EHL contacts. *STLE Tribology Transactions*, 1997, vol 40, p 613 – 620.

[130] Xu G., Sadeghi F. and Hoeprich M. R. Dent initiated spall formation in EHL rolling/sliding contacts. *ASME Journal of Tribology*, 1998, vol 120, p 453 – 462.

Appendix A

Transient EHL solver implementation

Discrete equations

$$\xi = \frac{\overline{\rho} H^3}{\overline{\eta}\overline{\lambda}} \tag{A.1}$$

$$\begin{aligned}
\xi_{i+1/2,j} &= \frac{\xi_{i,j} + \xi_{i+1,j}}{2}\, rh_X^2 \\
\xi_{i-1/2,j} &= \frac{\xi_{i-1,j} + \xi_{i,j}}{2}\, rh_X^2 \\
\xi_{i,j+1/2} &= \frac{\xi_{i,j} + \xi_{i,j+1}}{2}\, rh_Y^2 \\
\xi_{i,j-1/2} &= \frac{\xi_{i,j-1} + \xi_{i,j}}{2}\, rh_Y^2 \\
\Sigma\, \xi &= \xi_{i-1/2,j} + \xi_{i+1/2,j} + \xi_{i,j-1/2} + \xi_{i,j+1/2} \qquad \text{(A.2)}
\end{aligned}$$

The $NU2$ scheme is composed of two schemes depending on the h_X/h_T ratio. The operator $\mathcal{L}^h$ is defined in the implementation [1] as:

- if $h_X \leqslant h_T$ one gets[2]:

$$\begin{aligned}
\mathcal{L}^h \left\langle u^h \right\rangle = & rh_X^2 \left(\xi_{i+1/2,j} P_{i+1,j} - \left(\xi_{i+1/2,j} + \xi_{i-1/2,j}\right) P_{i,j} - \xi_{i-1/2,j} P_{i-1,j}\right) \\
& + rh_Y^2 \left(\xi_{i,j+1/2} P_{i,j+1} - \left(\xi_{i,j+1/2} + \xi_{i,j-1/2}\right) P_{i,j} - \xi_{i,j-1/2} P_{i,j-1}\right) \\
& - \left(rh_X - rh_T\right)\left(1.5\,\overline{\rho} H_{i,j} - 2.0\,\overline{\rho} H_{i-1,j} + 0.5\,\overline{\rho} H_{i-2,j}\right) \\
& - rh_T\, 1.5\,\overline{\rho} H_{i,j}
\end{aligned} \tag{A.3}$$

---

[1] to clarify the notation a little, the third subscript k related to the time step is omitted for the terms corresponding to the current time step k

[2] for the finest level if $h_T = h_X$

- if $h_X > h_T$ one gets[3]:

$$\begin{aligned}\mathcal{L}^h \left\langle u^h \right\rangle =& rh_X^2 \left(\xi_{i+1/2,j} P_{i+1,j} - \left(\xi_{i+1/2,j} + \xi_{i-1/2,j}\right) P_{i,j} - \xi_{i-1/2,j} P_{i-1,j}\right) \\ &+ rh_Y^2 \left(\xi_{i,j+1/2} P_{i,j+1} - \left(\xi_{i,j+1/2} + \xi_{i,j-1/2}\right) P_{i,j} - \xi_{i,j-1/2} P_{i,j-1}\right) \\ &- rh_X \, 1.5 \, \overline{\rho} H_{i,j} - \left(rh_T - rh_X\right) 1.5 \, \overline{\rho} H_{i,j} \end{aligned} \tag{A.4}$$

All the terms which correspond to previous time step are put in the right hand side of the equation. The residual terms for FAS scheme are not changed and coarsening routine is not changed. The right hand member reads:

- if $h_X \leqslant h_T$ one gets:

$$f_{i,j}^h = rh_T \left(-2.0 \, \overline{\rho} H_{i-1,j,k-1} + 0.5 \, \overline{\rho} H_{i-2,j,k-2}\right) \tag{A.5}$$

- if $h_X > h_T$ one gets:

$$\begin{aligned} f_{i,j}^h = & rh_X \left(-2.0 \, \overline{\rho} H_{i-1,j,k-1} + 0.5 \, \overline{\rho} H_{i-2,j,k-2}\right) + \\ & \left(rh_T - rh_X\right) \left(-2.0 \, \overline{\rho} H_{i,j,k-1} + 0.5 \, \overline{\rho} H_{i,j,k-2}\right) \end{aligned} \tag{A.6}$$

Gauss Seidel line relaxation

One can define the terms $dH_X^{(k)}$ and $dH_T^{(k)}$. They will be used to build the line relaxation matrix.

---

[3] for all the coarser levels

- if $h_X \leqslant h_T$ one gets:

$$
\begin{aligned}
dH_X^{(-3)} &= (rh_X - rh_T)\,(1.5\,\bar{\rho}_{i,j}K_{3,0} - 2.0\,\bar{\rho}_{i-1,j}K_{2,0} + 0.5\,\bar{\rho}_{i-2,j}K_{1,0})\\
dH_T^{(-3)} &= rh_T\,1.5\,\bar{\rho}_{i,j}K_{3,0}\\
dH_X^{(-2)} &= (rh_X - rh_T)\,(1.5\,\bar{\rho}_{i,j}K_{2,0} - 2.0\,\bar{\rho}_{i-1,j}K_{1,0} + 0.5\,\bar{\rho}_{i-2,j}K_{0,0})\\
dH_T^{(-2)} &= rh_T\,1.5\,\bar{\rho}_{i,j}K_{2,0}\\
dH_X^{(-1)} &= (rh_X - rh_T)\,(1.5\,\bar{\rho}_{i,j}K_{1,0} - 2.0\,\bar{\rho}_{i-1,j}K_{0,0} + 0.5\,\bar{\rho}_{i-2,j}K_{1,0})\\
dH_T^{(-1)} &= rh_T\,1.5\,\bar{\rho}_{i,j}K_{1,0}\\
dH_X^{(0)} &= (rh_X - rh_T)\,(1.5\,\bar{\rho}_{i,j}K_{0,0} - 2.0\,\bar{\rho}_{i-1,j}K_{1,0} + 0.5\,\bar{\rho}_{i-2,j}K_{2,0})\\
dH_T^{(0)} &= rh_T\,1.5\,\bar{\rho}_{i,j}K_{0,0}\\
dH_X^{(+1)} &= (rh_X - rh_T)\,(1.5\,\bar{\rho}_{i,j}K_{1,0} - 2.0\,\bar{\rho}_{i-1,j}K_{2,0} + 0.5\,\bar{\rho}_{i-2,j}K_{3,0})\\
dH_T^{(+1)} &= rh_T\,1.5\,\bar{\rho}_{i,j}K_{1,0}\\
dH_X^{(+2)} &= (rh_X - rh_T)\,(1.5\,\bar{\rho}_{i,j}K_{2,0} - 2.0\,\bar{\rho}_{i-1,j}K_{3,0} + 0.5\,\bar{\rho}_{i-2,j}K_{4,0})\\
dH_T^{(+2)} &= rh_T\,1.5\,\bar{\rho}_{i,j}K_{2,0}
\end{aligned}
\tag{A.7}
$$

- if $h_X > h_T$ one gets:

$$
\begin{aligned}
dH_X^{(-3)} &= rh_X\,1.5\,\bar{\rho}_{i,j}K_{3,0}\\
dH_T^{(-3)} &= (rh_T - rh_X)1.5\,\bar{\rho}_{i,j}K_{3,0}\\
dH_X^{(-2)} &= rh_X\,1.5\,\bar{\rho}_{i,j}K_{2,0}\\
dH_T^{(-2)} &= (rh_T - rh_X)1.5\,\bar{\rho}_{i,j}K_{2,0}\\
dH_X^{(-1)} &= rh_X\,1.5\,\bar{\rho}_{i,j}K_{1,0}\\
dH_T^{(-1)} &= (rh_T - rh_X)1.5\,\bar{\rho}_{i,j}K_{1,0}\\
dH_X^{(0)} &= rh_X\,1.5\,\bar{\rho}_{i,j}K_{0,0}\\
dH_T^{(0)} &= (rh_T - rh_X)1.5\,\bar{\rho}_{i,j}K_{0,0}\\
dH_X^{(+1)} &= rh_X\,1.5\,\bar{\rho}_{i,j}K_{1,0}\\
dH_T^{(+1)} &= (rh_T - rh_X)1.5\,\bar{\rho}_{i,j}K_{1,0}\\
dH_X^{(+2)} &= rh_X\,1.5\,\bar{\rho}_{i,j}K_{2,0}\\
dH_T^{(+2)} &= (rh_T - rh_X)1.5\,\bar{\rho}_{i,j}K_{2,0}
\end{aligned}
\tag{A.8}
$$

The matrix A^j in equation 2.39 reads:

$$\begin{aligned}
A^j_{i,i-3} &= -dH^{(-3)}_X - dH^{(-3)}_T \\
A^j_{i,i-2} &= -dH^{(-2)}_X - dH^{(-2)}_T \\
A^j_{i,i-1} &= -dH^{(-1)}_X - dH^{(-1)}_T + \xi_{i-1/2,j} \\
A^j_{i,i} &= -dH^{(0)}_X - dH^{(0)}_T - \Sigma\,\xi \\
A^j_{i,i+1} &= -dH^{(+1)}_X - dH^{(+1)}_T + \xi_{i+1/2,j} \\
A^j_{i,i+2} &= -dH^{(+2)}_X - dH^{(+2)}_T
\end{aligned} \tag{A.9}$$

Jacobi distributive line relaxation

$$\begin{aligned}
dK_0 &= K_{0,0} - \frac{1}{4}\,(2\,K_{1,0} + 2\,K_{0,1}) \\
dK_1 &= K_{1,0} - \frac{1}{4}\,(K_{2,0} + K_{0,0} + 2\,K_{1,1}) \\
dK_2 &= K_{2,0} - \frac{1}{4}\,(K_{3,0} + K_{1,0} + 2\,K_{2,1}) \\
dK_3 &= K_{3,0} - \frac{1}{4}\,(K_{4,0} + K_{2,0} + 2\,K_{3,1}) \\
dK_4 &= K_{4,0} - \frac{1}{4}\,(K_{5,0} + K_{3,0} + 2\,K_{4,1})
\end{aligned} \tag{A.10}$$

- if $h_X \leqslant h_T$ one gets:

$$\begin{aligned}
dH^{(-3)}_X &= (rh_X - rh_T)\,(1.5\,\bar\rho_{i,j} dK_3 - 2.0\,\bar\rho_{i-1,j} dK_2 + 0.5\,\bar\rho_{i-2,j} dK_1) \\
dH^{(-3)}_T &= rh_T\,1.5\,\bar\rho_{i,j} dK_3 \\
dH^{(-2)}_X &= (rh_X - rh_T)\,(1.5\,\bar\rho_{i,j} dK_2 - 2.0\,\bar\rho_{i-1,j} dK_1 + 0.5\,\bar\rho_{i-2,j} dK_0) \\
dH^{(-2)}_T &= rh_T\,1.5\,\bar\rho_{i,j} dK_2 \\
dH^{(-1)}_X &= (rh_X - rh_T)\,(1.5\,\bar\rho_{i,j} dK_1 - 2.0\,\bar\rho_{i-1,j} dK_0 + 0.5\,\bar\rho_{i-2,j} dK_1) \\
dH^{(-1)}_T &= rh_T\,1.5\,\bar\rho_{i,j} K_{1,0} \\
dH^{(0)}_X &= (rh_X - rh_T)\,(1.5\,\bar\rho_{i,j} dK_0 - 2.0\,\bar\rho_{i-1,j} dK_1 + 0.5\,\bar\rho_{i-2,j} dK_2) \\
dH^{(0)}_T &= rh_T\,1.5\,\bar\rho_{i,j} dK_0 \\
dH^{(+1)}_X &= (rh_X - rh_T)\,(1.5\,\bar\rho_{i,j} dK_1 - 2.0\,\bar\rho_{i-1,j} dK_2 + 0.5\,\bar\rho_{i-2,j} dK_3) \\
dH^{(+1)}_T &= rh_T\,1.5\,\bar\rho_{i,j} dK_1 \\
dH^{(+2)}_X &= (rh_X - rh_T)\,(1.5\,\bar\rho_{i,j} dK_2 - 2.0\,\bar\rho_{i-1,j} dK_3 + 0.5\,\bar\rho_{i-2,j} dK_4) \\
dH^{(+2)}_T &= rh_T\,1.5\,\bar\rho_{i,j} dK_2
\end{aligned} \tag{A.11}$$

- if $h_X > h_T$ one gets:

$$\begin{aligned}
dH_X^{(-3)} &= rh_X\,1.5\,\bar{\rho}_{i,j}dK_3\\
dH_T^{(-3)} &= (rh_T - rh_X)1.5\,\bar{\rho}_{i,j}dK_3\\
dH_X^{(-2)} &= rh_X\,1.5\,\bar{\rho}_{i,j}dK_2\\
dH_T^{(-2)} &= (rh_T - rh_X)1.5\,\bar{\rho}_{i,j}dK_2\\
dH_X^{(-1)} &= rh_X\,1.5\,\bar{\rho}_{i,j}dK_1\\
dH_T^{(-1)} &= (rh_T - rh_X)1.5\,\bar{\rho}_{i,j}dK_1\\
dH_X^{(0)} &= rh_X\,1.5\,\bar{\rho}_{i,j}dK_0\\
dH_T^{(0)} &= (rh_T - rh_X)1.5\,\bar{\rho}_{i,j}dK_0\\
dH_X^{(+1)} &= rh_X\,1.5\,\bar{\rho}_{i,j}dK_1\\
dH_T^{(+1)} &= (rh_T - rh_X)1.5\,\bar{\rho}_{i,j}dK_1\\
dH_X^{(+2)} &= rh_X\,1.5\,\bar{\rho}_{i,j}dK_2\\
dH_T^{(+2)} &= (rh_T - rh_X)1.5\,\bar{\rho}_{i,j}dK_2
\end{aligned} \tag{A.12}$$

The matrix A^j in equation 2.42 reads:

$$\begin{aligned}
A^j_{i,i-3} &= -dH_X^{(-3)} - dH_T^{(-3)}\\
A^j_{i,i-2} &= -dH_X^{(-2)} - dH_T^{(-2)} - \frac{1}{4}\,\xi_{i-1/2,j}\\
A^j_{i,i-1} &= -dH_X^{(-1)} - dH_T^{(-1)} + \xi_{i-1/2,j} + \frac{1}{4}\,\Sigma\,\xi\\
A^j_{i,i} &= -dH_X^{(0)} - dH_T^{(0)} - \frac{5}{4}\,\Sigma\,\xi\\
A^j_{i,i+1} &= -dH_X^{(+1)} - dH_T^{(+1)} + \xi_{i+1/2,j} + \frac{1}{4}\,\Sigma\,\xi\\
A^j_{i,i+2} &= -dH_X^{(+2)} - dH_T^{(+2)} - \frac{1}{4}\,\xi_{i+1/2,j}
\end{aligned} \tag{A.13}$$

Appendix B

Dry contact analytical model

The approximation of the hole and shoulder geometry influences additional pressure results. No study concerning the best approximation has been made. The aim was not to get the most accurate prediction of the additional pressure, but to introduce a physical approach of the shoulder influence in zone A, and to account for the zero pressure in zone B. The functions of the geometrical approximation functions are briefly reported below. These functions have no simple analytical expressions, but are easy to evaluate numerically.

The indent geometry and its derivatives read:

$$\mathcal{R} = -de^{-K\frac{r^2}{\phi^2}} \cos\left(\frac{\pi r}{\phi}\right) \tag{B.1}$$

$$\mathcal{R}' = \frac{\partial \mathcal{R}}{\partial r} = de^{-K\frac{r^2}{\phi^2}} \left\{ \frac{2Kr}{\phi^2} \cos\left(\frac{\pi r}{\phi}\right) + \frac{\pi}{\phi} \sin\left(\frac{\pi r}{\phi}\right) \right\} \tag{B.2}$$

$$\mathcal{R}'' = \frac{\partial^2 \mathcal{R}}{\partial r^2} = \frac{2dK}{\phi^2} e^{-K\frac{r^2}{\phi^2}} \left\{ \cos\left(\frac{\pi r}{\phi}\right) \left(1 - \frac{2Kr^2}{\phi^2}\right) - \frac{2\pi r}{\phi} \sin\left(\frac{\pi r}{\phi}\right) \right\} \tag{B.3}$$

Shoulder approximation

To calculate the shoulder additional pressure amplitude , a parabolic approximation of the shoulders has been used see figure B.3 and equation B.4. The shoulder approximation reads :

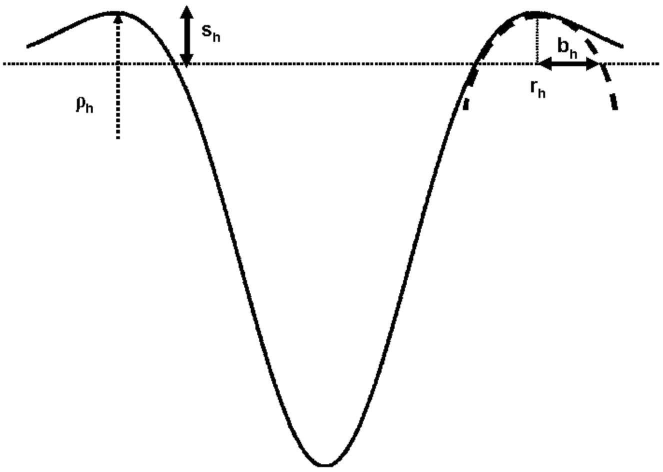

Figure B.1: Shoulder model diagram

$$\mathcal{R}_{approx} = -\frac{1}{\rho_h}\frac{r^2}{2} + s_h \tag{B.4}$$

The values r_h, s_h and ρ_h reads :

$$\left\{\begin{array}{l} \mathcal{R}'(r_h) = 0 \\ r_h \in \;]\frac{\phi}{2}\;\frac{3\phi}{2}[\end{array}\right. \Leftrightarrow \left\{\begin{array}{l} \tan(\hat{r}_h) = -\frac{2K}{\pi^2}\,\hat{r}_h \\ \hat{r}_h = \frac{\pi\, r_h}{\phi} \\ \hat{r}_h \in \;]\frac{1}{2}\;\frac{3}{2}[\end{array}\right.$$

The equation above is evaluated numerically, and the solution enables to deduce the numerical values below :

$$r_h = \beta(K)\,\phi \tag{B.5}$$

$$s_h = \mathcal{R}(r_h) = \gamma(K)\,d \tag{B.6}$$

$$\rho_h = \frac{1}{\mathcal{R}''(r_h)} = \mu(K)\frac{\phi^2}{d} \tag{B.7}$$

$$\nu(K) = \sqrt{\frac{\gamma(K)}{\mu(K)}} \tag{B.8}$$

Two parameters which are function of K are used to calculate $\nu(K)$. The radius of curvature of the shoulder ρ_h appears through the parameter $\mu(K)$ and $\gamma(K)$ corresponds to the shoulder height s_h. The factor $\nu(K)$ is given in figure B.2. It is used to calculate the shoulder influence.

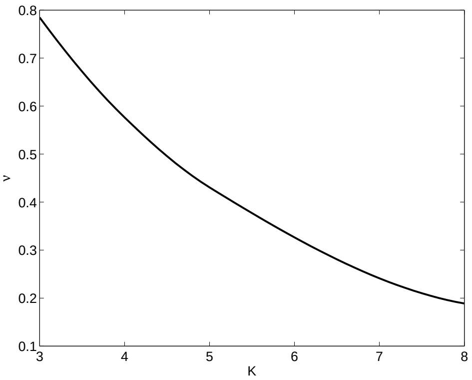

Figure B.2: ν as a function of K

Hole approximation

To calculate the hole additional pressure amplitude , the choice has been made to represent the hole with a parabolic approximation see figure B.3. The hole approximation reads :

$$\mathcal{R}_{approx} = -\frac{1}{\rho_b}\frac{r}{2}^2 + d \tag{B.9}$$

Two parameters which are function of K are used to compute $\zeta(K)$. The radius of curvature at the hole bottom ρ_b appears through the parameter $\lambda(K)$, and $\beta(K)$ is related to the radius r_h.

$$\rho_b = \lambda(K)\frac{\phi}{d}^2 \tag{B.10}$$

$$\zeta(K) = \frac{2\sqrt{\lambda(K)}}{\beta(K)} \tag{B.11}$$

$$\left\{\begin{array}{lll} \text{if} \quad \mathcal{R}(\phi/4) = \mathcal{R}_{approx}(\phi/4) & & \\ \quad\lambda(K) & = & \dfrac{1}{32\left(1 - \dfrac{e^{-K/16}}{\sqrt{2}}\right)} \end{array}\right.$$

When an approximation like the one represented figure B.3 is used, $\zeta(K)$ is almost constant and equal to 0.78.

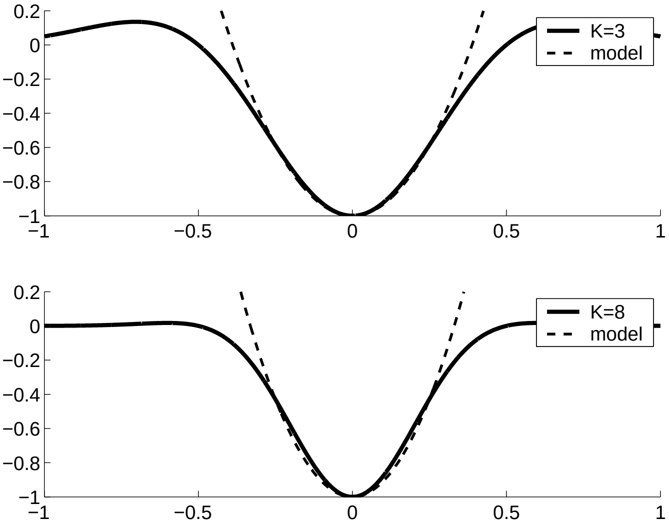

Figure B.3: Hole approximation with $\bar{\mathcal{R}}(\Phi/4) = \bar{\mathcal{R}}_{approx}(\Phi/4)$

Zone A coefficient adjustment

The coefficients of proportionality m and n of the shoulder and the hole influence in equation 3.5 are adjusted in zone A using the method of least squares see equations B.12, B.13.

$$x = \Delta P'_{hole}$$
$$y = \Delta P'_{shoulders}$$
$$f = \Delta P^{num}_{tot}$$
$$T = \sum x_i^2 \cdot \sum y_i^2 - \left(\sum x_i\, y_i\right)^2$$
$$n = \left(\sum y_i^2 \cdot \sum f_i\, x_i - \sum x_i\, y_i \cdot \sum f_i\, y_i\right) / \; T \tag{B.12}$$
$$m = \left(\sum x_i^2 \cdot \sum f_i\, y_i - \sum x_i\, y_i \cdot \sum f_i\, x_i\right) / \; T \tag{B.13}$$
$$\tag{B.14}$$

Zone B coefficient adjustment

As mentioned before, the ratio between deformed and initial indent depth F is directly linked to the indent slope D/Φ. The zero pressure in the indent hole appears for a slope of 0.25. Moreover, an horizontal asymptote appears when the slope is large because the hole will be less and less deformed. When the slope decreases to 0.25, a second asymptote correctly matches

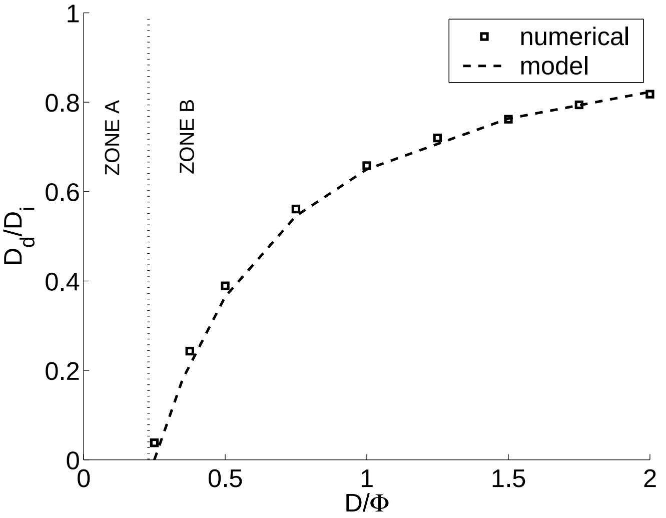

Figure B.4: Ratio between deformed and initial indent depth D_d/D_i as a function of the indent slope D/Φ

the numerical results. The parameters k and θ of equation B.15 have been adjusted accordingly. The final equations reads:

$$
\begin{aligned}
F &= \frac{D_d}{D_i} \\
\theta &= 1.1 \\
k &= 2.1 \\
F &= \frac{k\,(D/\Phi - 0.25)}{\sqrt[\theta]{1 + \{k\,(D/\Phi - 0.25)\}^{\theta}}} && \text{for } D/\Phi > 0.25 \qquad \text{(B.15)} \\
F &= 0 && \text{for } D/\Phi \leqslant 0.25 \\
\Delta P_{tot} &= n\frac{D}{\Phi}\zeta(K)\,(1 - s\,F^{\omega}) + m\frac{D}{\Phi}\,\nu(K) && \text{(B.16)}
\end{aligned}
$$

Appendix C

Line contact stress

For infinitely elongated Hertzian contact without friction, the stress distribution in the material has a simple analytical expression C.1, see Smith and Liu [104]. The authors detail also a more complicated set of equations to account for Hertzian contact with friction. Elliptical contacts were studied by Sackfields and Hills [100, 101].

$$
\begin{aligned}
C1 &= (1+X)^2 + Z^2 \\
C2 &= (1-X)^2 + Z^2 \\
\psi &= \frac{\pi}{C1}\,\frac{1-\sqrt{\dfrac{C2}{C1}}}{\sqrt{\dfrac{C2}{C1}}\sqrt{2\sqrt{\dfrac{C2}{C1}}+\dfrac{C1+C2-4}{C1}}} \\
\overline{\psi} &= \frac{\pi}{C1}\,\frac{1+\sqrt{\dfrac{C2}{C1}}}{\sqrt{\dfrac{C2}{C1}}\sqrt{2\sqrt{\dfrac{C2}{C1}}+\dfrac{C1+C2-4}{C1}}}
\end{aligned}
$$

$$
\begin{aligned}
\sigma_{xx} &= -\frac{Z}{\pi}\,\left(\overline{\psi}\,(1+2\,X^2+2\,Z^2) - 2\,\pi - 3\,X\psi\right) \\
\sigma_{yy} &= \nu\,(\sigma_{xx}+\sigma_{zz}) \\
\sigma_{zz} &= -\frac{Z}{\pi}\,\left(\overline{\psi} - X\psi\right) \\
\sigma_{xz} &= -\frac{Z^2\psi}{\pi}
\end{aligned}
\tag{C.1}
$$

List of Figures

List of Tables